

8-2018

Design and Analysis of a Body-Powered Underactuated Prosthetic Hand

Hun Chan Lee
Purdue University

Follow this and additional works at: https://docs.lib.purdue.edu/open_access_theses

Recommended Citation

Lee, Hun Chan, "Design and Analysis of a Body-Powered Underactuated Prosthetic Hand" (2018). *Open Access Theses*. 1557.
https://docs.lib.purdue.edu/open_access_theses/1557

This document has been made available through Purdue e-Pubs, a service of the Purdue University Libraries.
Please contact epubs@purdue.edu for additional information.

**DESIGN AND ANALYSIS OF A BODY-POWERED UNDERACTUATED
PROSTHETIC HAND**

by

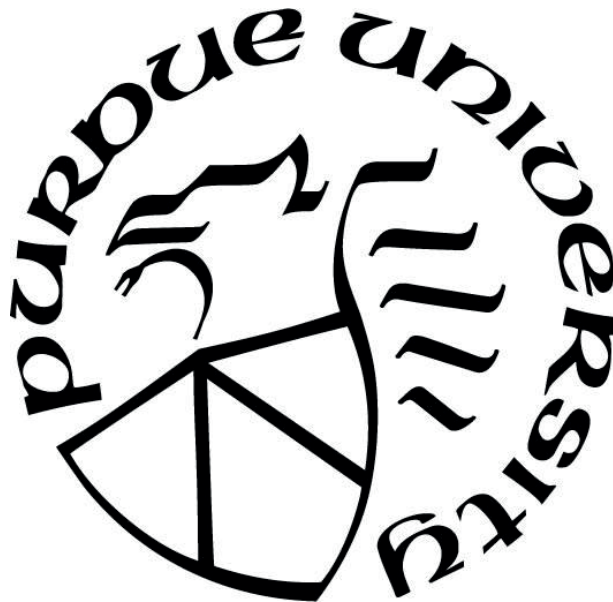
Hun Chan Lee

A Thesis

Submitted to the Faculty of Purdue University

In Partial Fulfillment of the Requirements for the degree of

Master of Science in Mechanical Engineering



School of Mechanical Engineering

West Lafayette, Indiana

August 2018

THE PURDUE UNIVERSITY GRADUATE SCHOOL
STATEMENT OF THESIS APPROVAL

Dr. Raymond J. Cipra, Chair

School of Mechanical Engineering

Dr. Peter H. Meckl

School of Mechanical Engineering

Dr. Eric A. Nauman

School of Mechanical Engineering

Dr. David J. Cappelleri

School of Mechanical Engineering

Approved by:

Dr. Jay P. Gore

Head of the School Graduate Program

Dedicated to the memories of my grandfather, Woo June Lee

ACKNOWLEDGMENTS

I would like to express my greatest appreciation to my advisor, Professor Raymond J. Cipra, for helping and supporting me. I truly appreciate his help on my project and enjoyed the brainstorming sessions. I would like to appreciate my committee members, Professor Peter H. Meckl, Professor Eric A. Nauman and Professor David J. Cappelleri for reviewing my work. In addition, I would like to thank Bong Joong Kim for helping my project and my friends for the encouragement. Lastly, I would like thank my parents for all their support and encouragement that helped me to motivate and successfully finish my degree.

TABLE OF CONTENTS

	Page
LIST OF TABLES	viii
LIST OF FIGURES	ix
SYMBOLS	xiv
ABBREVIATIONS	xvi
ABSTRACT	xvii
1 INTRODUCTION	1
1.1 Electrically Powered Prosthetic Hands	2
1.2 Body Powered Prosthetic Hand	4
1.3 Underactuated Hand	6
1.4 Design Requirements	9
1.5 Scope of Research	11
1.6 Thesis Overview	11
2 DESIGN CONCEPTS	13
2.1 Actuation	13
2.2 Locking Mechanism Design	14
2.2.1 Linear Ratchet	16
2.2.2 Rotary Ratchet	18
2.2.3 Cantilever Bar Design	20
2.3 Mechanical Fuse	22
2.4 Finger Design and Fabrication	24
2.4.1 Compliant Finger	24
2.4.2 Supporting Finger	25
2.4.3 Fabrication	27
2.5 Final Prototype	31

	Page
3 ANALYSIS	32
3.1 Preshaping Analysis	32
3.1.1 Assumptions	34
3.1.2 Finger Nomenclatures	35
3.1.3 Flexure Joints	37
3.1.4 Preshaping - Force Control	38
3.1.5 Preshaping - Rack Actuated Distance Control	47
3.1.6 Mechanical Fuse Effect	49
3.2 Preshaping Analysis Results and Discussion	51
3.2.1 Force Control Results	51
3.2.2 Rack Actuated Distance Control Results	55
3.2.3 Mechanical Fuse Results	56
3.3 Force Analysis	58
3.3.1 Analysis	58
3.3.2 Results	61
4 EXPERIMENT	67
4.1 Preshaping Experiment	67
4.1.1 Experimental Method	67
4.1.2 Results	68
4.1.3 Discussion	71
4.2 Grasping Experiment	73
4.2.1 Verification of the Maximum Load	73
4.2.2 Grasping Demonstration	73
5 CONCLUSIONS	78
6 RECOMMENDATIONS	80
REFERENCES	82
A JOINT ANGLE CALCULATION DERIVATION	88
A.1 Force Controlled	88

	Page
A.2 Rack Distance Controlled	91
B POINT CONTACT METHOD DERIVATION	93
C CAPSTAN EQUATION DERIVATION	98
D CONTACT FORCE ANALYSIS DERIVATION	101
E PRESHAPING DATA ANALYZING ALGORITHM	105
F GRASPING DEMONSTRATION	108
F.1 Successful	108
F.2 Partially Successful	109
F.3 Unsuccessful	115
G MECHANISM DRAWINGS	116
H CODE	130
H.1 Preshaping - Input Force Control Using Point Contact Method	130
H.2 Preshaping - Input Force Control Using Capstan Equation Method	133
H.3 Preshaping - Rack Actuated Distance Control	136
H.4 Preshaping Data Analyzing Code	141
H.5 Contact Force Analysis Code - Varying Angle	146
H.6 Contact Force Analysis Code - Varying Contact Distance	150
I BILL OF MATERIALS	154

LIST OF TABLES

Table	Page
2.1 Average range of motion of the wrist.	15
3.1 Finger Parameters.	35

LIST OF FIGURES

Figure	Page
1.1 Level of amputation of upper limb.	1
1.2 Commercially available electrically powered prosthetic hands. (a) Bebionic hand [2]. (b) Vincent Evolution 3 [3]. (c) i-limb ultra [4].	3
1.3 Body powered prosthetic hand [7].	4
1.4 Wrist operated 3-D printed prosthetic hand [9].	5
1.5 Examples of underactuated hands. (a) SDM Hand [11]. (b) Ocean One Hand [12]. (c) HERMES Hand [13]. (d) Model O [14]. (e) Deployable Surgical Grasper [15]. (f) SARAH Hand [16].	7
2.1 Proposed prosthetic hand design.	13
2.2 Linear ratchet mechanism design attached to the hand.	16
2.3 Operating process of the linear ratchet mechanism (a) Pawl is at the initial position, resting on a tooth of the rack (b) Pawl is lifted up and moved to the second bi-stable position (c) The second position of the pawl is maintained and the rack returns to the initial position (d) Pawl is pushed down and moved to the initial position.	17
2.4 Rotary ratchet mechanism with labels.	18
2.5 Rotary ratchet mechanism design (a) Initial position (b) First rotary ratchet - Actuating (c) First rotary ratchet tooth - Actuated (d) Second rotary ratchet - Actuating (e) Second rotary ratchet tooth - Actuated.	19
2.6 Different situations after actuating the ratcheting mechanism (a) original position (b) Actuated position (c) Actuated position with generated torque from the wrist (d) Actuated position with an applied force from the support structure.	21
2.7 Cantilever support.	22
2.8 Comparison of the position of compliant finger (with and without a fuse).	23
2.9 Compliant finger design.	24
2.10 Supporting finger mounting level.	26
2.11 Supporting finger design (a) Initial design (b) Second Design.	26

Figure	Page
2.12 Labeled drawing of the finger frame. The red line indicates the tendon cable route, the blue lines indicate the thin sacrificial walls, and the mechanical anchors are indicated with yellow circles.	27
2.13 Fabricated fingers (a) Compliant finger (b) Supporting finger.	29
2.14 Dremel 3D45 FDM 3D Printer.	30
2.15 Final Prototype.	31
3.1 The configuration of the compliant finger when it adapts to a circular shape of the object.	33
3.2 The design of finger with parameters.	33
3.3 Pseudo rigid body model representation.	37
3.4 The design of a flexure joint with parameters.	38
3.5 Simplified diagram of a flexure joint.	39
3.6 Bent configuration of the compliant finger.	40
3.7 FBD of the compliant finger during preshaping. (a) DP (b) DP and IP. . .	41
3.8 Location of the friction effects where the highlighted regions experience the frictional effects.	42
3.9 FBD of the cable at different location of the cable route (a) Partial FBD of the cable at the curvature of the route (b) FBD of the cable at the end of the route inside of the DP (c) FBD of the cable at the IP (d) FBD of the cable at the PP.	43
3.10 Location of the capstan effect.	47
3.11 Joint angle computation process including a mechanical fuse.	49
3.12 The change in the joint angle of the phalanges without friction.	52
3.13 The change in the joint angle of the phalanges with friction.	52
3.14 Comparison of the point contact method and the capstan equation method.	53
3.15 The trajectory of the tip of finger.	54
3.16 The change in joint angles as actuator angle changes. The blue line represents θ_2 . The red line represents θ_3	55
3.17 Required force to actuate based on the actuation angle. The blue line represents the tension of the cable without friction. The red line represents the tension of the cable with friction.	56

Figure	Page
3.18 The change in the joint angles as the actuation angle changes with spring.	57
3.19 Diagram of the finger with contacting distance labels.	58
3.20 FBD of the phalanges with contact forces (a)IP and DP (b)DP.	60
3.21 Stability where DP contact location is 7.91 mm away relatively and IP contact location is 6.02 mm away relatively. The yellow regions represent a stable region and the dark blue region represents an unstable region.	61
3.22 Effects of the joint angles on the contact force produced by the DP. Contact location is at 21.88 mm (6.02 mm for the relative distance) for the IP and 23.28 mm (7.91 mm for the relative distance) for the DP.	62
3.23 Effects of the joint angles on the contact force produced by the IP. Contact location is at 21.88 mm (6.02 mm for the relative distance) for the IP and 23.28 mm (7.91 mm for the relative distance) for the DP.	63
3.24 Effects of the contact locations on the contact force produced by the DP when the DP is at 48 deg and the IP is at 50 deg.	64
3.25 Effects of the contact locations on the contact force produced by the IP when DP is at 48 deg and IP is at 50 deg.	65
4.1 Preshaping experiment setup.	68
4.2 Processed image.	69
4.3 One cycle of results. The weight was added from 0 g to 2000 g and subtracted from 2000 g to 0 g.	70
4.4 θ_2 w.r.t. Input force.	71
4.5 θ_3 w.r.t. Input force.	71
4.6 Illustration of the hysteresis when the total input force is 16.7 N.	72
4.7 Maximum load verification experiment. (a) 0g. (b) 100g. (c) 200g. (d) 300g. (e) 400g. (f) 500g. (g) 500g top view. (h) 600g.	74
4.8 Pinch grasp contact location.	75
4.9 Grasping a locknut using the tip of the finger.(a) Finger contacting at contact region 1.(b) Finger contacting at contact region 2.	76
4.10 Grasping Experiment. (a) Air refresher spray. (b) Scissors. (c) Pencil case. (d) Computer mouse. (e) Umbrella. (f) Lighter. (g) Knife. (h) Water bottle.	77
6.1 The recommended design allows the support finger to move when force is applied.	80

Figure	Page
A.1 FBD of distal and intermediate phalanx during preshaping.	89
A.2 FBD of distal phalanx during preshaping.	90
B.1 Location of the friction effects.	93
B.2 FBD of the cable at different location of the cable route (a) FBD of the cable at the curvature of the route (b) FBD of the cable at the end of the route inside of the DP (c) FBD of the cable at the IP (d) FBD of the cable at the PP.	94
C.1 Free body diagram used to derive the capstan equation.	98
D.1 FBD of the phalanges with contact forces (a)IP and DP (b)DP.	102
D.2 DP Finger Pad with Labels.	103
D.3 Rotation about Z axis.	103
E.1 The extracted color data.	105
E.2 Example of Conversion Process (a)Original image (b)Binary image of the red color space.	106
E.3 Processed image.	107
F.1 Cup.	108
F.2 Air refresher spray bottle. (a) Side view. (b) Top View	109
F.3 Pencil Case.	110
F.4 Computer mouse.	110
F.5 Umbrella.	111
F.6 Lighter.	111
F.7 Knife.	112
F.8 Pen.	112
F.9 Scissor.	113
F.10 Screw.	114
F.11 Nut.	115
F.12 Coin.	115
G.1 Rotary ratchet drawing.	117
G.2 Compliant finger mold drawing.	118

Figure	Page
G.3 Rack drawing.	119
G.4 Hand socket drawing.	120
G.5 Pawl drawing.	121
G.6 Stopper drawing.	122
G.7 Rotary ratchet link drawing.	123
G.8 Rack base drawing.	124
G.9 Cantilever bar structure.	125
G.10 Supporting Finger.	126
G.11 Gauntlet.	127
G.12 Finger mount.	128
G.13 Forearm.	129

SYMBOLS

θ_i	The i^{th} joint angle
$\theta_{i_{int}}$	The initial value of i^{th} joint angle
L_i	The length of i^{th} flexure joint
k_i	The rotational stiffness of the j^{th} joint
F_a	The magnitude of the applied cable force
B	The base length of the flexure joints
h	The height of the flexure joints
E	The modulus of elasticity of the flexure joints
I	The area moment of inertia of the flexure joints
a_i	The x distance between the center of i^{th} joint and the end of cable route of i^{th} link
b_i	The y distance between the center of i^{th} joint and the end of cable route of i^{th} link
C	The distance traveled by the rack and cable
R_i	The length of i^{th} link
ϕ	The total contact angle
d_f	Deflected distance of a spring
k_f	The stiffness of a spring
r_{cix}	The x direction distance between the center of i^{th} joint and the contact location of the corresponding link
r_{ciy}	The y direction distance between the center of i^{th} joint and the contact location of the corresponding link
F_{ix}	The x component of i^{th} link reaction force
F_{iy}	The y component of i^{th} link reaction force

F_{cix}	The x component of i^{th} link contact force
F_{ciy}	The y component of i^{th} link contact force
T	The tension of the cable
γ_i	The angle between i^{th} and $i+1^{th}$ surface of the distal pad
N	The normal force
μ	Coefficient of friction

ABBREVIATIONS

PDMS	Polydimethylsiloxanen
DOF	Degrees of Freedom
FBD	Free Body Diagram
DP	Distal Phalanx
IP	Intermediate Phalanx
PP	Proximal Phalanx
PRBM	Pseudo Rigid Body Model

ABSTRACT

Lee, Hun Chan M.S.M.E., Purdue University, August 2018. Design and Analysis of a Body-Powered Underactuated Prosthetic Hand. Major Professor: Raymond J. Cipra.

As affordable and efficient 3-D printers became widely available, researchers are focusing on developing prosthetic hands that are reasonably priced and effective at the same time. By allowing anyone with a 3-D printer to build their body powered prosthetic hands, many people could build their own prosthetic hand. However, one of the major problems with the current designs is the user must bend and hold their wrist in an awkward position to grasp an object.

The primary goal of this thesis is to present the design process and analysis of a mechanical operated, underactuated prosthetic hand with a novel ratcheting mechanism that locks the finger automatically at a desired position. The prosthetic hand is composed of the following components: a frame for the hand and forearm, ratcheting mechanism, finger mount, rack, pawl and stopper for ratchet, cable, springs, rigidly supporting finger and a compliant finger. The compliant finger was manufactured using shape deposition manufacturing. The joints of the finger were made using PMC 780, polyurethane material, and the finger pads were made of Polydimethylsiloxane(PDMS). To estimate how a compliant finger behaves on the actual system with the ratcheting mechanism and how much force is required to operate this finger, the preshaping analysis was conducted. The preshaping analysis data was verified by loading and unloading weights to the tendon cable and taking pictures of the finger each time the cable force was varied. Then, the pictures were processed using MATLAB image processing tools to calculate joint angles. Additionally, the contact force analysis was performed to determine the effects of the contact location and finger

joint angles on the magnitude of contact force given the tension of the cable. Using the contact force analysis, it would be possible to estimate how much load the hand can hold. Finally, the hand was tested to hold various shapes of objects to prove how well it can grasp. Based on the experiment, the hand had a higher success rate of grasping objects that are lightweight (less than 500g) and cylindrical or circular shaped.

1. INTRODUCTION

In 2005, around 541,000 Americans had some sort of upper limb amputation and this number is expected to be doubled at least by 2050. In Italy and U.K., about 3500 and 5200 upper limb amputation cases are reported respectively and of those cases, 61 percent is transcarpal amputation [1]. Figure 1.1 shows the level of upper limb absence.

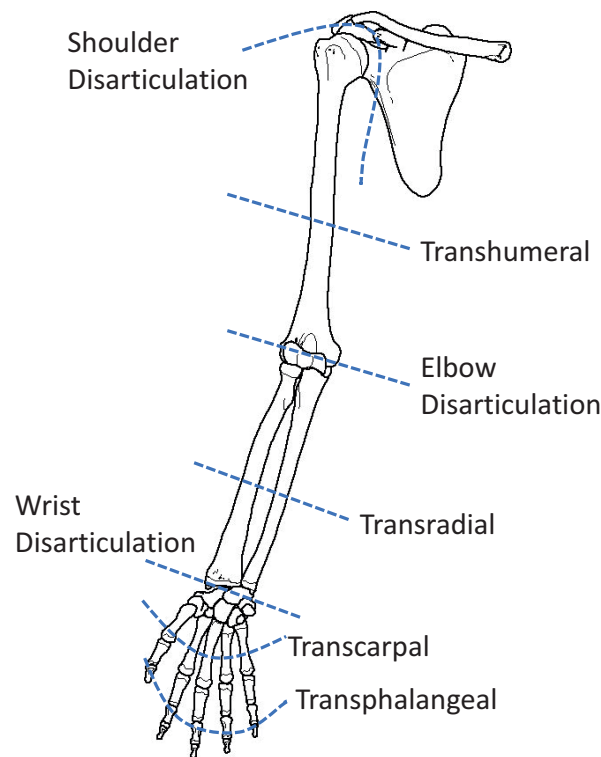


Fig. 1.1. Level of amputation of upper limb.

Depending on the level of upper limb absence, the design of the prosthetic hands and the actuating method of the hands change. To substitute the amputated portion of the upper limb, the amputees choose among cosmetic hand, body powered hand, and electrically powered hand. When they select the type of prosthesis, their economic status and the types of job they perform heavily influence their decision. For example, for people who have a laborious job, they tend to consider a cosmetic or body powered prosthetic hand over a electrically powered hand because they need more durable and less expensive hand that can be replaced easily if needed. On the other hand, if a user's job requires more dexterity, then they consider a electrically powered prosthetic hand. Hereafter, Chapter One presents different types of prosthetic hands and their advantages and disadvantages.

1.1 Electrically Powered Prosthetic Hands

In the market, electrically powered prosthetic hands are available. Many of which use electromyography (EMG), which captures the electrical signals from the muscle activities to control the prosthetic hand. In the research field, other control methods such as ultrasound imaging, neural interface, surface electrodes, and pattern recognition are currently developing without a clinical application [1]. As of now, most of the commercially available hands use EMG signals to control the hand. Figure 1.2 shows some of the prosthetic hands in the market. As described in [5], the commercially available hands, shown in Figure 1.2, use multiple motors to achieve multiple degrees of freedom (DOF). Due to higher DOF, these hands can accomplish different types of grasp such as power, precision, lateral, finger point grasp and more, and they are more dexterous. In addition, because they use multiple motors to operate the fingers, these hands can easily exert a larger range of grasping force on an object with precision compare to the body powered prosthetic hands.

Even though the commercially available myoelectric hands, prosthetic hands controlled using the electrical signal produced by the muscles, have many advantages



(a)



(b)



(c)

Fig. 1.2. Commercially available electrically powered prosthetic hands. (a) BeBionic hand [2]. (b) Vincent Evolution 3 [3]. (c) i-limb ultra [4].

in terms of dexterity and grasping force, there are still many disadvantages leading to the rejection of the electrically powered hands as well. Some of the drawbacks of electrically powered hands are heavyweight, lack of sensory feedback, noise produced by motor, high cost, and high learning curve. The prosthetic users express that the electrically powered hands are usually too heavy to use, where most of the weight accumulates from motors and batteries attached to the hand [1]. In addition, currently available electrically operated hands still lack sensory feedback that helps the users to control and sense an object. For example, a user needs to operate their

hand more carefully in a dark environment because they do not know how much they opened or closed their fingers [6]. Lastly, many people reject commercially available prosthetic hands because the cost of electrically powered hands is too high for an average person to accommodate. Even though many research groups are developing cost-effective prosthetic hands, they are not commercially available yet.

1.2 Body Powered Prosthetic Hand



Fig. 1.3. Body powered prosthetic hand [7].

Although electrically powered prosthetic hands are more advanced and dexterous, body powered prosthetic hands such as split-hook prosthetic terminal devices are more commonly used due to their robustness, low-cost, low learning curve, efficient performance, and feedback from body [6,8]. Unlike the electrically powered prosthetic hands, for the body powered prosthetic hands the users can sense how much the hook is opened using the awareness of the position of their body. Therefore, even when a user is in a dark room, they can sense how much the hook is opened and operate their hand accordingly. An example of conventional body powered prosthetic hands is shown in Figure 1.3.

The design of split hook prosthetic hand has not changed much since 1912 [8]. The body powered prosthetic operates by either moving an elbow or shoulder. Depending on the size of the residual upper limb, the user may choose to use their wrist, elbow, or shoulder to operate the hand. A split hook hand works by pulling an attached cable between the amputee's body and the terminal device. When the user pulls the tendon cable using their amputated limb in a certain direction, the split hook opens by working against the rubber band around the hook. Once the actuating portion of the upper limb moves back to the original position, the hook closes due to the force generated by the rubber band.



Fig. 1.4. Wrist operated 3-D printed prosthetic hand [9].

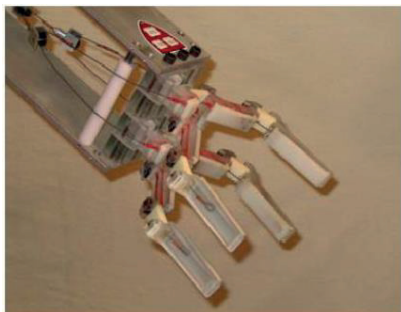
Another type of body powered prosthetic hands is the 3-D printed prosthetic hand. Figure 1.4 shows an example of 3-D printed prosthetic hands. The 3-D printed prosthetic hands have been making a great stride because of the widely available low-cost and efficient 3-D printers. They are commonly operated by using a wrist or an elbow. Thus, for the users to operate these types of hand, they require the users to have a functional wrist with a partial or full palm or a functional elbow with a partial or full forearm. The definition of functional wrist and elbow is the person needs to be able to bend those parts of the body at least 30 degrees.

The advantages of the 3-D printed prosthetic hands are low-cost, ease of manufacturing, and light weight. However, the currently available 3-D printed prosthetic hands are mainly used for children. The current design of those hands cannot exert enough force for average adults to use. In addition, the users must bend their wrist to close the fingers and maintain that position until they want to reopen their fingers. However, maintaining such position is cumbersome and tiring. Therefore, throughout this thesis, the author intends to explain some of the existing problems of the 3-D printed prosthetic hands and discuss potential solutions to those problems in Chapter Two.

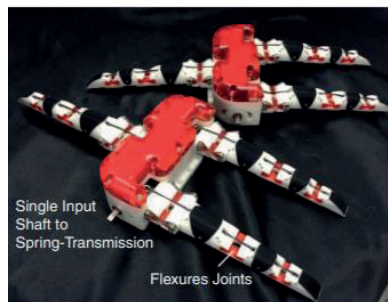
1.3 Underactuated Hand

To reduce the number of actuators, many research groups use an underactuated control system. An underactuated system refers to a system in which the number of its inputs is smaller than the DOF. This system is beneficial for many different applications, many of which can be found from manipulators and graspers. Some of the key advantages of using an underactuated system are to reduce the overall weight of the system by reducing the number of actuators and to use the power of input actuators more efficiently. However, because its DOF is larger than the number of actuators, this system itself cannot be directly controlled. The kinematics of the system needs to be considered to understand how it works [10].

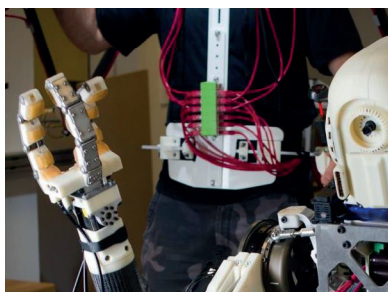
One of the popular applications of an underactuated system is an underactuated grasper. Many of the underactuated hands are inspired by the SDM hand developed from Harvard University [17], [18] where they use the shape deposition manufacturing method, a layered manufacturing technique that fabricates both the compliant and rigid links simultaneously. Figure 1.5(a) shows the SDM hand. Grab Lab at Yale University has further improved such design of the hand to produce different kinds of underactuated hands. These models that they developed use one actuator to control



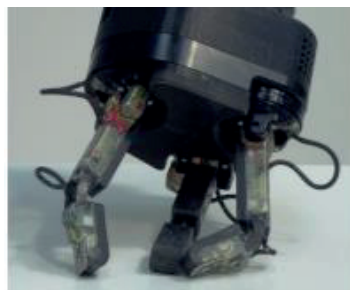
(a)



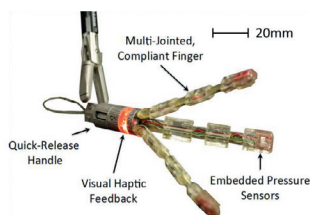
(b)



(c)



(d)



(e)



(f)

Fig. 1.5. Examples of underactuated hands. (a) SDM Hand [11]. (b) Ocean One Hand [12]. (c) HERMES Hand [13]. (d) Model O [14]. (e) Deployable Surgical Grasper [15]. (f) SARAH Hand [16].

a finger with multiple joints [14]. Figure 1.5(d) shows one of the hands developed from Grab Lab. Even though these manipulators are underactuated systems, they can grasp an object using different types of grasp such as pinch and power grasp defined by Cutkosky [19]. Similarly, the HERMES Hand, shown in Figure 1.5(c) from M.I.T. [13] and the Ocean One Hand, shown in Figure 1.5(b), from Stanford University [12] used

a similar strategy to achieve grasping for robots with different applications, search and rescue robot and underwater manipulation respectively. Those groups further enhanced their stiffness of the finger joints using springs. As seen from those projects, one of the key features of underactuated hands is the shape adaptability. For example, if a finger has only one actuator to control multiple joints on that finger, then once a joint touches an object, the stiffness of the corresponding joint becomes infinity. This forces that joint to stay at the same position and move other joints with lower stiffness. This concept will be further discussed later in this thesis. Another group from Harvard University developed a grasper, shown in Figure 1.5(e), that could be used for surgical purposes which mainly uses a pinch grasp to operate [15]. On the other hand, unlike the compliant underactuated manipulators, Gosselin and his group investigated developing an underactuated system with a series of mechanical links. Figure 1.5(f) shows SARAH Hand developed by Gosselin's group. Essentially, by connecting a series of four bar mechanisms, the hand has 10 DOF with only 2 actuators [16]. To close the fingers, SARAH Hand only uses one motor input to control all three fingers simultaneously.

For the prosthetic hand purpose, it is critical that the hand is light weight. According to [20], [21], the consumers of prosthetic hands prefer a light weight prosthetic hand because they have a power and weight constraint on their amputated arm. This limit gets tighter as the level of amputation gets higher. To solve such issue, many groups used the underactuated hand concept to reduce the number of actuators to lower the weight of the hand. The prototype that was developed for this project uses the same concept. However, the main purpose was not necessarily to reduce the weight. To avoid restricting the range of motion of a body part, only one input, wrist, is allocated for this prototype. Even though the number of inputs can be increased by using a fully functional arm or other joints, this would essentially restrict the range of motion of the arm. If other joints of body are used to control the hand, they would restrict the movement of the amputated arm because the user needs to move their arm within a limited range of motion unless they want to actuate. However, it is possible

to increase the number of inputs by adding control inputs that can be operated by the other hand that is functional. For this prosthetic hand, only the wrist portion of the arm was used as the input. Therefore, to use this hand, a functional wrist needs to be present.

1.4 Design Requirements

As described in [1], some of the important design priorities are listed below:

- Comfort
- Durability
- Appearance
- Function
- Weight
- Cost
- Grip strength
- Sensory feedback
- Ability to maneuver in awkward positions
- Physical effort needed to use

Of those requirements, comfort, durability, appearance, functionality, and cost were the most prioritized requirements. For the functionality of the body powered hand, gripping, steadying, manipulating, appearance, and body languages are the prioritized functions [1].

The present research focuses on improving the design of previously developed prosthetic hands while keeping the price of the hand affordable. To allow the hand to be accessed widely around the world, the hand needs to be cost-efficient. To keep an

affordable price range, electronic components such as motors and sensors had to be removed. Though there are many advantages of using the electronic components, it was an appropriate choice to lower the price and the weight of the hand. Additionally, as stated in [1], the replacement of battery and the hand are critical issues of the electrically powered prosthetic hands that need to be solved.

One of the biggest problems with the current 3-D printed prosthetic hands is the users need to rotate their wrist by at least 30 degrees to fully close the hand and maintain such position until they desire to open their fingers. However, such position is uncomfortable to maintain for a long period of time and an awkward hand position to be at. Most of the body powered, 3-D printed prosthetic hands do not have a locking mechanism to avoid the position described. By installing a locking mechanism to hold the fingers at a certain position, the hand should be more comfortable to use.

Another ability of prosthetic hands that the user desires is the capability to easily adapt to the shape of an object. Previously developed body powered prosthetic hands, especially a hand with a hook, are not capable of adapting to the shape of an object because two rigid bars open and close to grasp it.

Regarding the weight of the hand, an average weight of a human hand is around 400 g. However, according to [5], prosthetic devices that weigh around the same as an average weight of a human hand felt too heavy. Therefore, the specific weight requirement was included as a part of design requirements.

Referring to those design requirements and previously developed 3-D printed prosthetic hand specifications, the following requirements were selected:

1. Ability to produce 1.5 kg grip load which is enough for most of the daily living activities [22]
2. Ability to produce 20 N pinch force [23]
3. Capability to hold a 1~15 cm wide object
4. Easily adapt to the shape of an object

5. Finger Locking Mechanism
6. Rotate wrist less than 30 degrees to actuate the finger
7. Low cost (less than 100 dollars to build)
8. Light weight (less than 400 g)

1.5 Scope of Research

The purpose of this research is to improve the design of previously developed body powered, 3-D printed prosthetic hands. This research mostly focuses on developing a novel locking and actuating mechanism and fabricating compliant fingers that are adapted from the previously published papers. Additionally, this work focuses on developing a prototype of prosthetic hand with the locking mechanism that could potentially satisfy the design requirements described in section 1.4. Lastly, the preshaping and contact force analysis of the hand are performed to determine the workspace of the compliant finger and the force required to trigger the rotary ratchet actuator. The information obtained from those analyses and the results from the preshaping and grasping experiments will become a basis of the system that customizes a hand for each user based on the size, shape, and strength of their wrist.

1.6 Thesis Overview

Chapter Two of this thesis reviews the design concepts of the prosthetic hand. This chapter reviews how each component of the hand operates and the purpose of each component. This chapter will explain further how each part of the hand helps to satisfy the design requirements described in Chapter One and the uniqueness of those parts. Additionally, it reviews how each component, specifically the fingers, has been manufactured. Hybrid deposition method was applied to fabricate compliant fingers. This chapter will further clarify the materials of the hand and the manufacturing process. Chapter Three reviews the preshaping and force analysis. The results of

those analyses help to predict the trajectory of the fingertip and required torque from the user's wrist to actuate the hand. These analyses will help to optimize the parameters of each component by observing the required torque to operate before manufacturing the hand. The results of this chapter will be further verified by the preshaping and grasping experiment. Chapter Four describes the purpose and the set-up of the preshaping and grasping experiment. It also reviews the results and discusses the results of the experiment. Chapter Five presents the conclusion which summarizes this thesis and in Chapter Six, it discusses about the recommendations for the future research and potential designs that could improve the hand.

2. DESIGN CONCEPTS

This chapter presents the design concepts of critical components of the proposed prosthetic hand shown in Figure 2.1. The hand is composed of a ratcheting mechanism, mechanical fuse, compliant finger, and a supporting finger. This chapter reviews the actuation method, introduce each component, and discusses the purpose of each component. Refer to Appendix G for the detailed drawings with parameters.

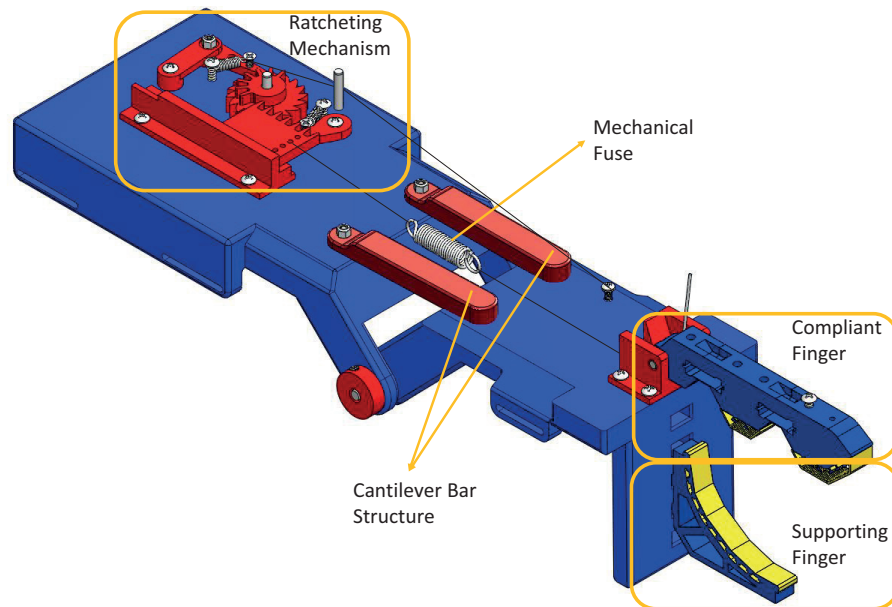


Fig. 2.1. Proposed prosthetic hand design.

2.1 Actuation

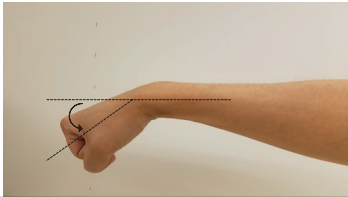
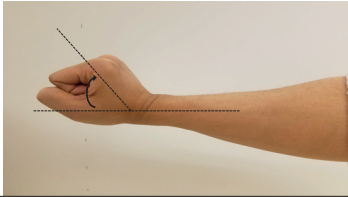
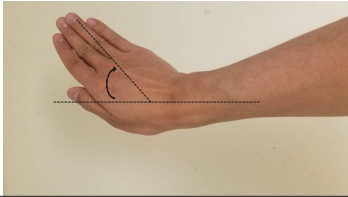
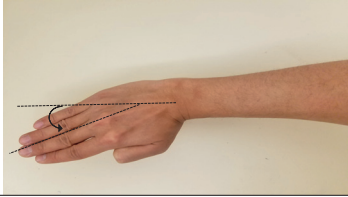
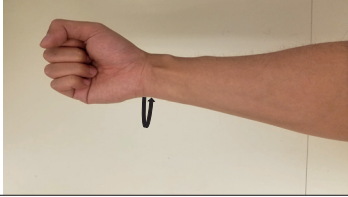

Previously developed 3-D printed, body-powered prosthetic hands require the flexion of the user's wrist to operate them. Once the hand is actuated using their wrist, the cables along the fingers of the 3-D printed hand are pulled to close the fingers.

Other actuation methods were looked at but not used for the proposed prosthetic hand design. The flexion of the wrist was the best option because using other joints such as elbow or shoulder would lower the precision of the actuation and it would limit the range of motion of the entire arm. Additionally, compared to other wrist motions as shown in Table 2.1 [24], which shows the average range of motion, the flexion of the wrist has a wider range of motion which makes it easier to rotate in comparison to other wrist motions. However, it needs to be further studied if the range of motion and the torque generated from the wrist of the amputees are similar to that of average person.

2.2 Locking Mechanism Design

One of the problems with the existing 3-D printed prosthetic hands and other voluntary closing prosthetic hands is that the fingers of those hands cannot be locked at a certain position. To maintain the position of those fingers, the user must keep flexing their wrist or hold their actuating portion of the body position the same until they want to reopen the fingers. That position is an awkward position to be at and it is difficult to maintain the same position for a long period of time. To avoid this problem, a locking mechanism is needed. Considering that the hand has a limited DOF, a mechanism was designed to perform two tasks at once: pulling the tendon cable for the finger and locking the cable at the new position. Taking those functional requirements into consideration, a mechanism like a ratchet was a suitable mechanism. During the process of conceptualization, both linear ratchet and rotary ratchet were considered to adjust the position of the finger. To effectively lock the finger, a rotatable cantilever bar design was proposed.

Table 2.1. Average range of motion of the wrist.

Type of Rotation	Range of Motion (Degrees)
Flexion 	≈ 78
Extension 	≈ 60
Ulnar Flexion 	≈ 21
Radial Flexion 	≈ 38
Full Supination 	90
Full Pronation 	90

2.2.1 Linear Ratchet

Initially, a linear ratchet type mechanism was designed to fulfill the functional requirements described in the previous section. A similar type of mechanism was found in [25], where the linear ratchet with a motor is used to control the thumb of a prosthetic hand. Figure 2.2 illustrates the mechanism design with labels and shows how the mechanism operates.

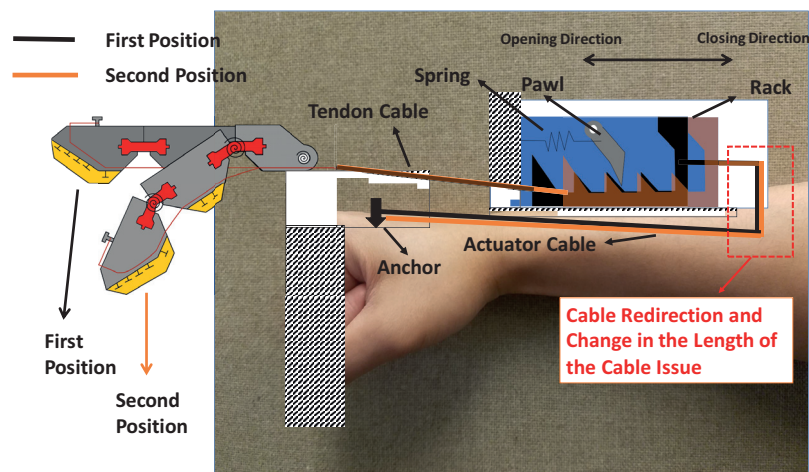


Fig. 2.2. Linear ratchet mechanism design attached to the hand.

The mechanism contains a bi-stable pawl, rack, and base for the rack. For this mechanism, the rack cannot move toward the hand unless it reaches the last tooth of the rack. The last tooth is taller than the other teeth on the rack. This forces the bi-stable pawl to rotate to the second position. Figure ?? illustrates how the linear ratchet moves. Because the rack is spring loaded, once the pawl moves to the second position, the rack is pulled back to the initial configuration by the spring attached in front of the rack. Consecutively, due to the design of the rack, the rack forces the pawl to move to its first position.

The design of this mechanism effectively satisfies the previously described requirements; however, it is difficult to use the flexion motion of the wrist to move the rack

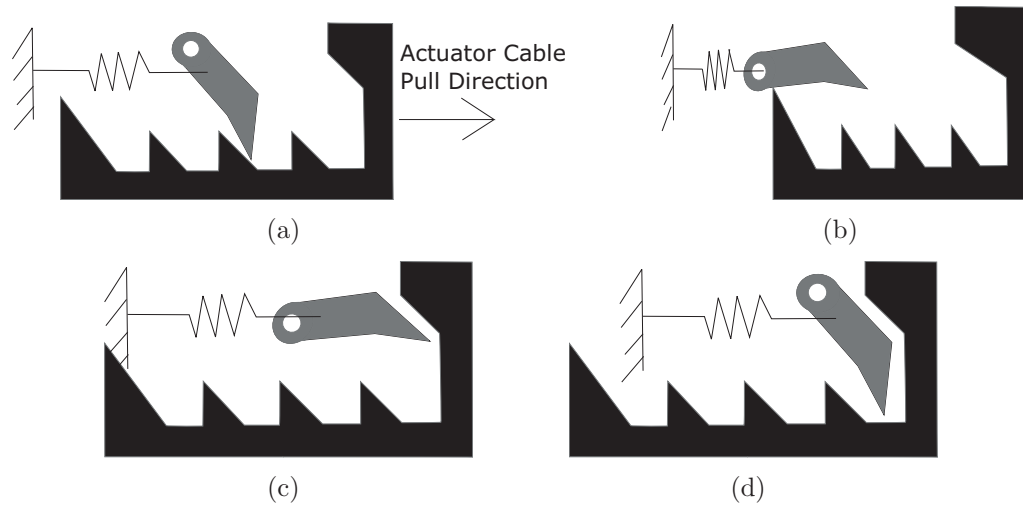


Fig. 2.3. Operating process of the linear ratchet mechanism (a) Pawl is at the initial position, resting on a tooth of the rack (b) Pawl is lifted up and moved to the second bi-stable position (c) The second position of the pawl is maintained and the rack returns to the initial position (d) Pawl is pushed down and moved to the initial position.

to the direction that closes the fingers effectively. To move this rack successfully, the cable attached to the rack needs to be redirected and the length of the cable needs to change to pull the rack. However, considering the contact force between the cable and its route and the frictional force along the route, the mechanical advantage would be low and the length of the cable cannot be changed to pull the rack using only an input. Therefore, this mechanism did not completely satisfy the given design requirements. Additionally, while testing the prototype of this mechanism, it was difficult to maintain the bi-stability of the pawl. For example, when there is an external impulsive force acting on the ratcheting system, the pawl may move from the second position to the first position since the pawl is only marginally stable at the second configuration and it only requires a small amount of force to change its position. Lastly, preventing the rack from lifting up from the base without an extra support on top of the rack which would make the rack harder to pull due to friction.

2.2.2 Rotary Ratchet

To solve the problems seen from the linear ratcheting mechanism, a rotary ratchet type mechanism was designed as an alternative. This mechanism is composed of a rotary ratchet with a partial gear, rack for the partial gears, pawl, and stopper. Figure 2.4 shows the structure of the mechanism.

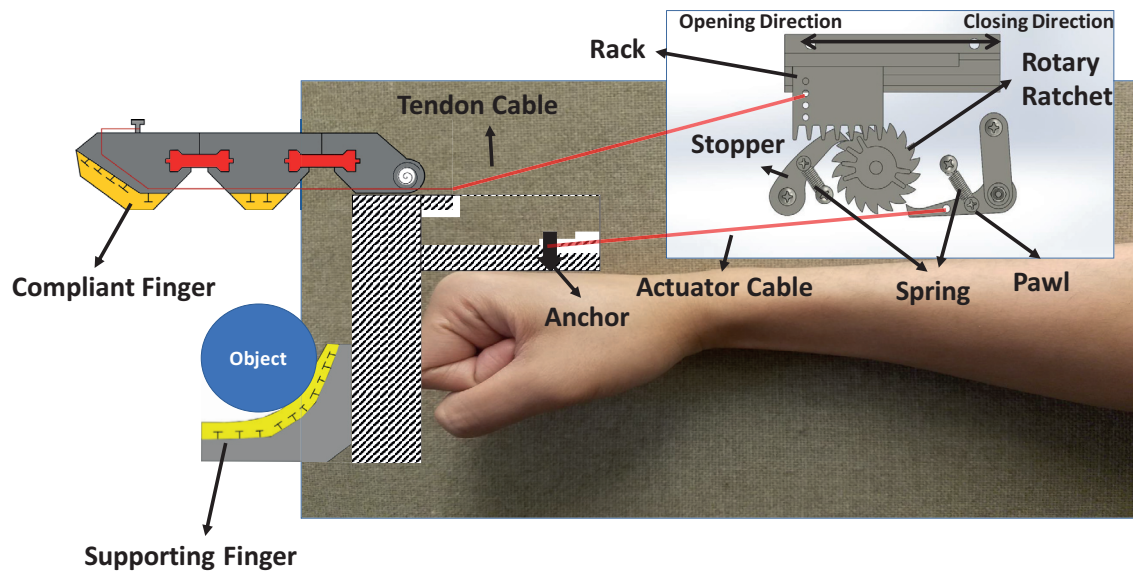


Fig. 2.4. Rotary ratchet mechanism with labels.

As described previously, the mechanism needs to do two functions: pulling the tendon cable and effectively locking the finger at a desired location. The mechanism shown in Figure 2.5 is capable of pulling the tendon cable and adjusting the position of the finger. Unlike a conventional ratcheting system, the pawl of this mechanism is not stopping the ratchet from rotating instead it is actuated by pulling the cable attached between the pawl and the gauntlet of the hand. The pawl moves whenever the user flexes the wrist. As can be seen from Figure 2.5, the string is not rerouted unlike the linear ratchet mechanism described in the previous section and the length of the actuator cable does not change. After actuating the pawl, the pawl automatically

returns to the initial configuration if the user extends their wrist back to the original position due to a spring attached to it. For this mechanism, the stopper acts like a pawl of the conventional mechanism, which prevents the ratchet from rotating in undesired direction.

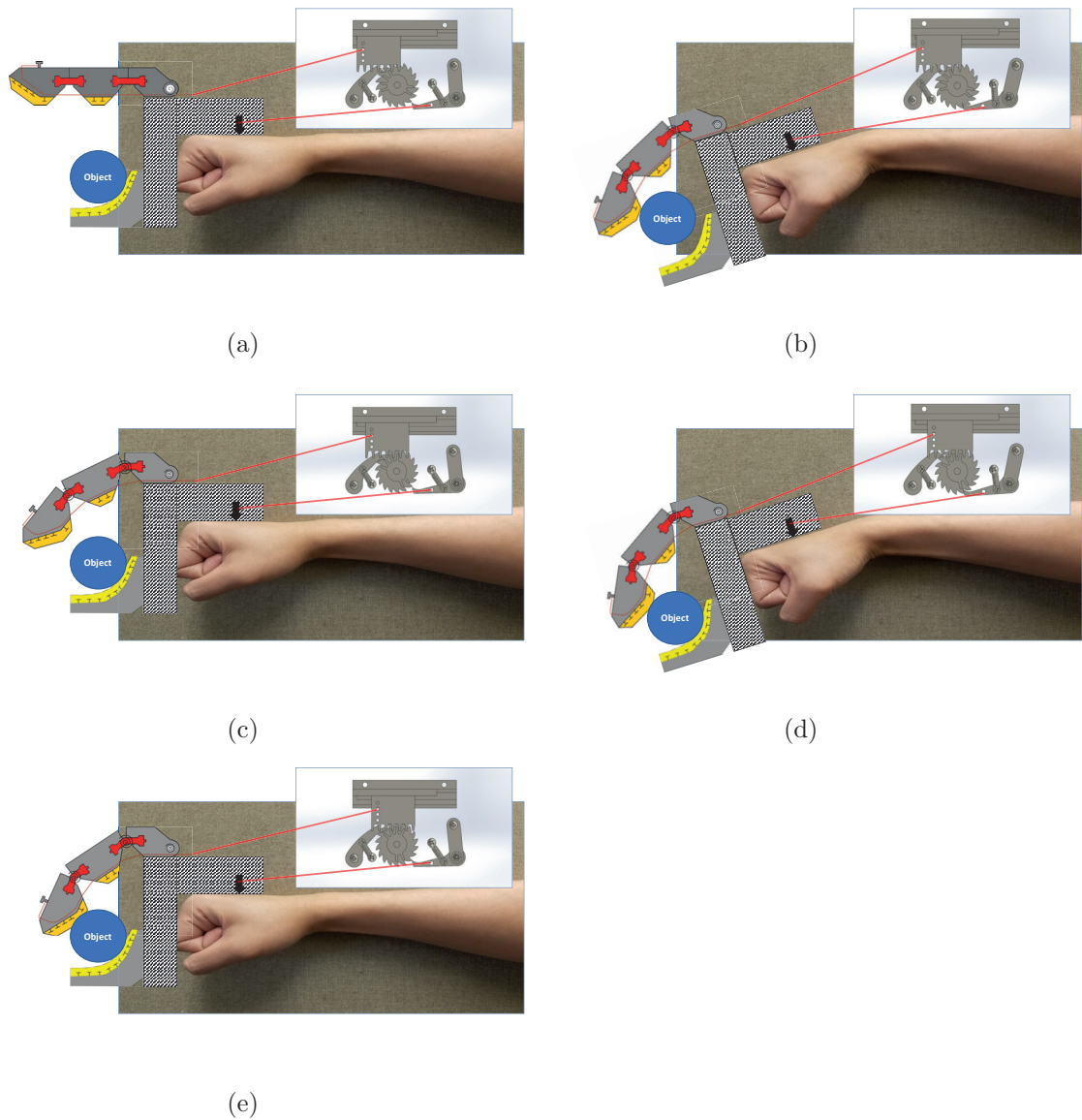


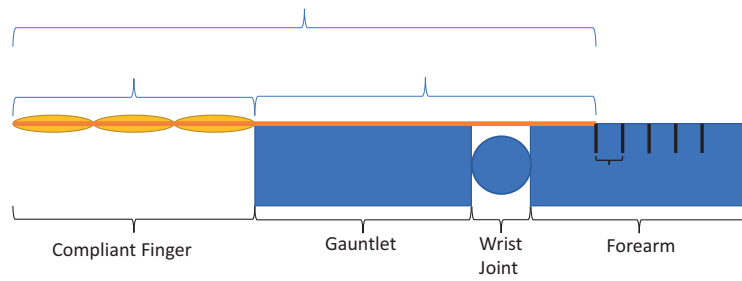
Fig. 2.5. Rotary ratchet mechanism design (a) Initial position (b) First rotary ratchet - Actuating (c) First rotary ratchet tooth - Actuated (d) Second rotary ratchet - Actuating (e) Second rotary ratchet tooth - Actuated.

Figure 2.5 illustrates an example of grasping an object using the compliant finger and the ratcheting mechanism. The joint angles of the finger need to be adjusted by actuating the ratcheting mechanism. To grasp an object, the ratcheting mechanism may need to be actuated several times depending on the size of the object. Due to a limited range of motion of the pawl, the rotary ratchet is only able to move only one or two teeth at a time. Once the first tooth of the partial gear engages with the rack, then it pulls the rack toward the direction that closes the fingers. When the ratcheting mechanism is actuating as shown in Figures 2.5(b) and 2.5(d), the compliant finger is further actuated than the actuated position as shown in Figures 2.5(c) and 2.5(e). When the ratcheting mechanism actuates as the wrist rotates, the tendon cable has to be further pulled as well. Therefore, when the ratcheting mechanism is actuating, the compliant finger has to curl more than when the ratcheting mechanism has finished actuating and the wrist has returned to the rest position. The rack continues to pull the tendon cable to close the hand until the gear and the rack are disengaged. Once they disengage, the rack moves back to the initial position due to the compliant joints. As the compliant joints return to the initial configuration, the finger pulls the cable toward the opened hand configuration direction as well. A unique feature of this mechanism is that the rack and the rotary ratchet can be easily replaced. The number of teeth on the ratchet and the rack can be changed based on the user's preference.

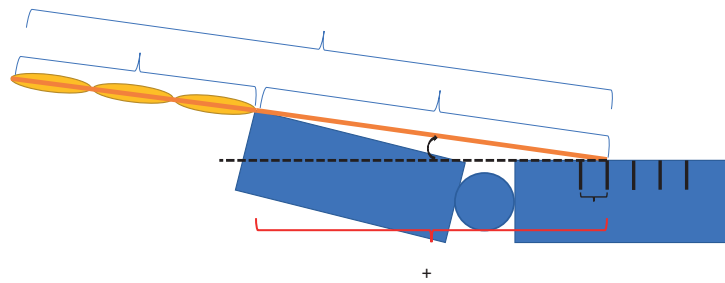
2.2.3 Cantilever Bar Design

One problem that was shown from both linear and rotary ratcheting mechanisms was that the finger cannot be locked at a position unless the top surfaces of the gauntlet and forearm are on the same plane. When the rack is pulled back, the distance traveled by the rack needs to be compensated from somewhere in the system.

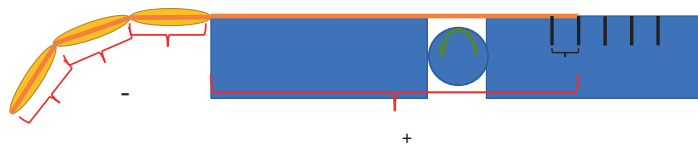
The easiest way to compensate the distance is extending the wrist because when the wrist is extended, the shortest path between the finger and the rack is formed.



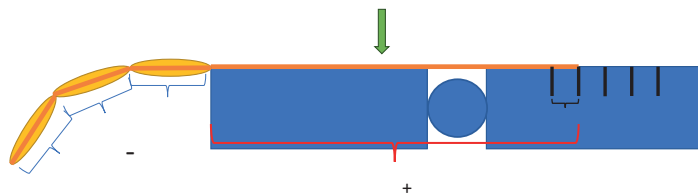
(a)



(b)



(c)



(d)

Fig. 2.6. Different situations after actuating the ratcheting mechanism (a) original position (b) Actuated position (c) Actuated position with generated torque from the wrist (d) Actuated position with an applied force from the support structure.

Figure 2.6(b) illustrates the natural position of the system after actuating the ratcheting mechanism. As mentioned, extending the wrist does not keep the finger at a desired position since the top surfaces of the gauntlet and forearm are forming an angle. Therefore, to keep the finger at a desired position, either the user needs to generate torque from their wrist to keep two parts straight or there must be a structure that prevents the wrist joint from extending. Figures 2.6(c) and 2.6(d) show the position of the system in those two situations. However, it is exhausting for the user to constantly generate torque to lock the finger at a certain position.

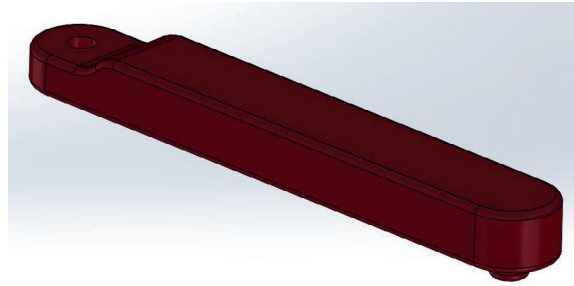


Fig. 2.7. Cantilever support.

To avoid cases shown in Figures 2.6(b) and 2.6(c), a cantilever structure was designed to effectively lock the finger at a position. As shown in Figure 2.7, it is a cantilever bar structure that prevents the gauntlet from rotating. The cantilever bar structures help to effectively keep the top surface of the gauntlet and that of the forearm leveled flat to lock the finger in place. Refer to Figure 2.1 to see how the cantilever supports are attached. If the user needs to open their finger for any reason, they can rotate the cantilever supports and extend their wrist.

2.3 Mechanical Fuse

When both the distal phalanx (DP) and immediate phalanx (IP) contact an object or if they reach their maximum range of motion, the stiffness of the joints increases drastically. Using the rotary ratchet mechanism described earlier, the mechanical

advantage of the mechanism drastically is lowered if the finger is at either one of those two situations. In those scenarios, the user needs to flex their wrist with significantly greater amount of force than usual because the joints are essentially locked and the cable along the finger cannot be further reduced to compensate the distance traveled by the rack. At this point, to open the hand, the user needs to disassemble the mechanism or slack the tendon cable by extending their wrist.

However, those motions are cumbersome; they are not the best solutions to those problems. To resolve them, a spring was attached between the rack and the finger. Figure 2.8 shows where the spring is attached. In this work, this spring is defined

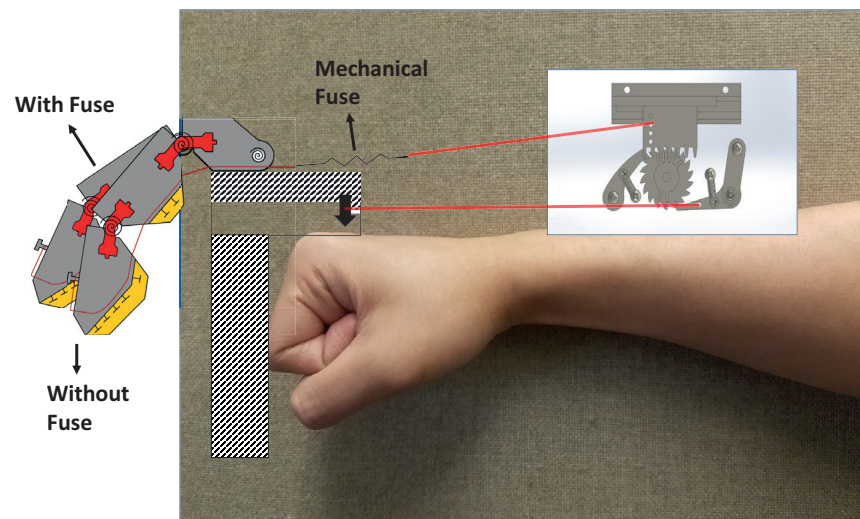


Fig. 2.8. Comparison of the position of compliant finger (with and without a fuse).

as a mechanical fuse. Unlike a conventional fuse where a fuse stops a system, this mechanical fuse overrides the inextensible cable condition. When the phalanges reach their maximum range of motion or contact an object, the spring starts to extend to compensate the distance traveled by the rack. Even though the user needs to flex their wrist with a higher force each time, the force required to pull will be much less than without a fuse and the required amount of force can be controlled by changing the stiffness of the spring.

2.4 Finger Design and Fabrication

For the proposed hand, it has two different types of finger: compliant finger and supporting finger. The compliant finger is actuated using the flexion of the hand. On the other hand, the supporting finger is not actuated; it is a stationary finger that is attached to the gauntlet of the hand.

2.4.1 Compliant Finger

To satisfy the shape adaptability requirement and to avoid using electronic actuators, an underactuated hand was designed. This hand design requires only one input to actuate the finger. Similar variations of this hand were referenced, as described in Section 1.3, when this hand was designed. As [11, 17, 26] describe, one of the main advantages of an underactuated hand is the shape adaptability. In addition, this underactuated hand does not require a control algorithm to control each joint to adapt to the shape of an object. This shape adaptability was further improved by replacing rigid finger joints with compliant joints as shown in Figure 2.9. Normally, a revolute

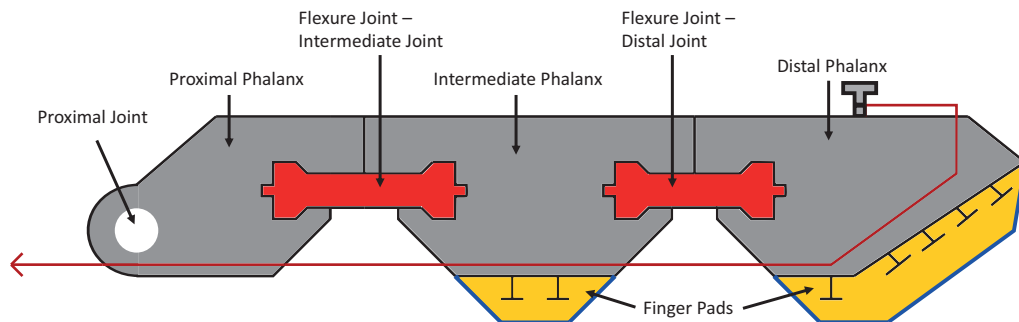


Fig. 2.9. Compliant finger design.

joint only has one DOF. On the other hand, a compliant joint can bend in different directions as well. This bending displacement can be controlled by changing the area moment of inertias of the joints. The flexion and extension direction of moment of in-

ertia is significantly lower compared to abduction and adduction direction of moment of inertia. Consequently, the finger is mainly extending and flexing to adapt to the shape of an object, but at the same time, the joints are capable of slightly deforming in other directions as well to adapt. This allows it to reject external disturbances [26], and such characteristic helps increase the durability of the hand. However, the second moment of inertias need to be carefully chosen. If the moment of inertia in abduction and adduction is too low, then the finger cannot hold a heavy object. A contact force generated on the finger pad is enough to bend the joints in undesired directions. Additionally, the moment of inertia directly impacts the required tension to operate the finger. Therefore, the size of the joints needs to be optimized based on the users. If thin joints are desired, thin spring steel can be embedded to the joints to increase the moment of inertia as described in [15] or side supports on the phalanges can be installed to prevent the joints from bending in undesired directions.

Another feature of this hand design is the finger pad. Between PLA material and an object, there is not much friction unless the object itself provides a lot of friction. Therefore, without exerting a high grasping force, the object cannot be grasped and would tend to slip. On the other hand, adding finger pads on each phalanx, which are made of Polydimethylsiloxane (PDMS), provide more friction between the finger and object. In addition to the material of the finger, the texture of pads is not smooth which would provide additional friction.

2.4.2 Supporting Finger

The proposed hand does not have a thumb which is a critical component when it needs to grasp an object because a thumb helps to support the object from sliding away from other four fingers. For the proposed hand, instead of having a thumb, it contains a rigidly supporting finger that acts like a thumb but it does not have any DOF. However, the supporting finger can be easily taken off and replaced. On the gauntlet of the hand, there are multiple levels to place the supporting finger to

help grasp different sizes of object as shown in Figure 2.10. Additionally, the friction between the object and the supporting finger has been increased by adding a pad that is made of PDMS.

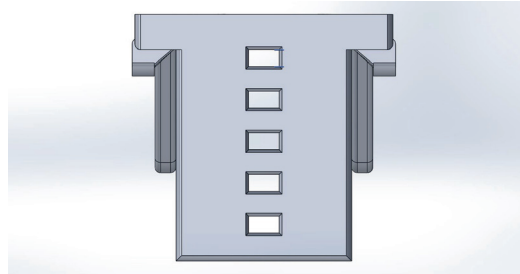


Fig. 2.10. Supporting finger mounting level.

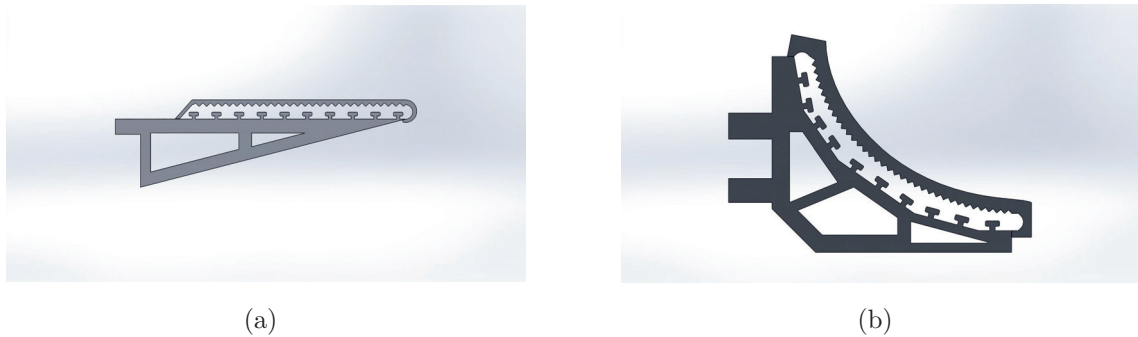


Fig. 2.11. Supporting finger design (a) Initial design (b) Second Design.

The initial design of the finger is shown in Figure 2.11(a). Even though the initial design helps to grasp an object, if there is only one finger attached to the hand, then the compliant finger has a small space to move. To resolve the problem seen from the initial concepts, the shape of the finger was changed to a curved L shape as shown in Figure 2.11(b). Such design helps to increase the workspace of the compliant finger. When the new design of the supporting finger is used then, the tip of the compliant finger does not touch the supporting finger as fast as using the the initial design.

2.4.3 Fabrication

- Compliant and Support Finger Frame Design

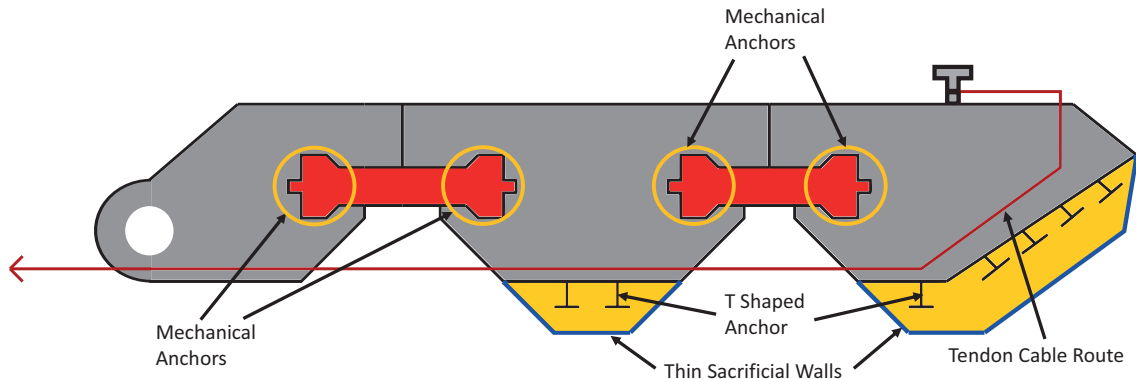
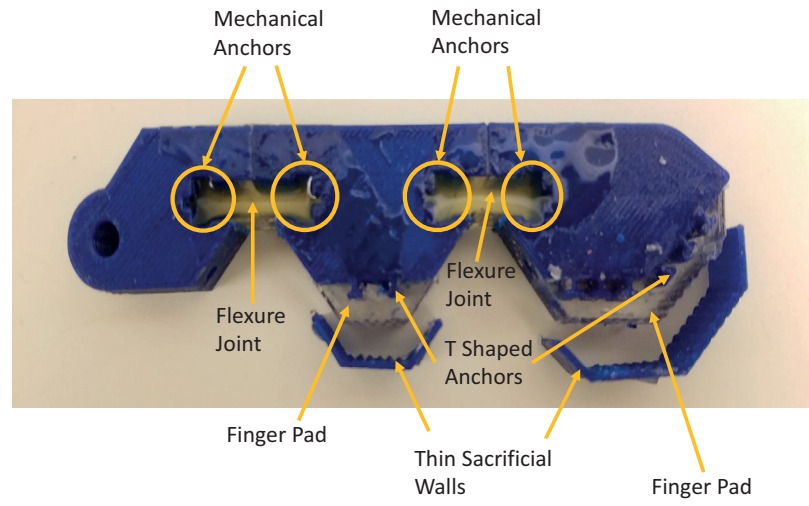


Fig. 2.12. Labeled drawing of the finger frame. The red line indicates the tendon cable route, the blue lines indicate the thin sacrificial walls, and the mechanical anchors are indicated with yellow circles.

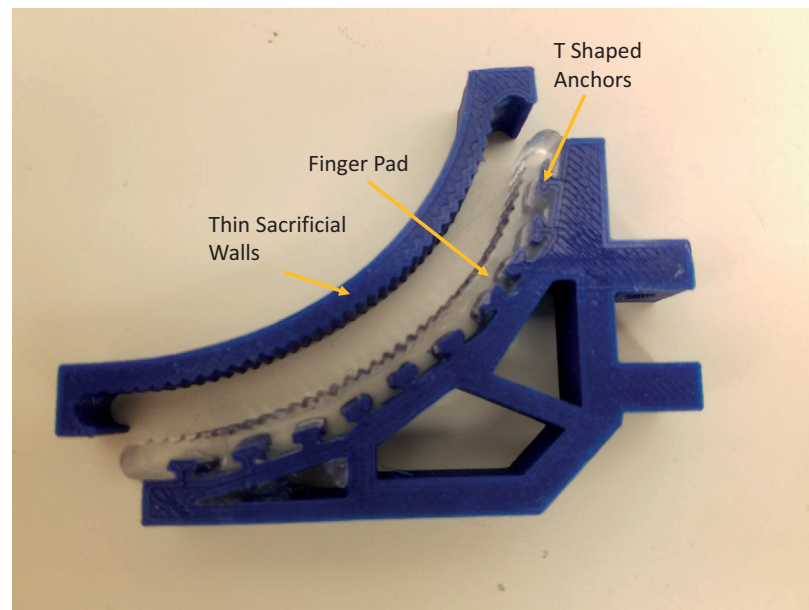
The frame of the fingers includes a tendon cable route, T shaped anchors for the pads, thin sacrificial walls, and a space for finger pads and joints. The frame was designed as one piece because the resolution of the printer was not high. It was difficult and inefficient to design a shell that fits multiple parts; therefore, the frame was designed as one body. Figure 2.12 illustrates the drawing of the finger frame with labels and Figure 2.13 shows the fabricated fingers. For the design of the finger joints, the shape of two sides of the flexure joints act as if the joints have an anchor on each side. Those shapes are referred to as mechanical anchors. The mechanical anchors help to interlock with the rigid links next to the joints.

Without the mechanical anchors, it would be too difficult to maintain their original condition over time. The paper [27] written by Ma further describes how the mechanical anchors help to interlock rigid bodies. Similarly, the T shaped anchors that are 3-D printed as a part of the frame help the compliant finger pads to stay attached to the finger over time. The design of the frame includes thin wall structures for

the shape of the joints. The thickness of the wall was reduced as much as possible; however, it heavily depends on the resolution of the printer. Additionally, in [27], Ma suggests a small gap, 0.25 times the 3-D printer nozzle diameter, between the sacrificial wall and the rigid body helps to remove the wall because of the stress concentration. Lastly, the polyurethane based finger pads were used to help the fingers grip an object. While grasping an object, the material of the pad and unevenness on the pad would provide more friction than without them [13].



(a)



(b)

Fig. 2.13. Fabricated fingers (a) Compliant finger (b) Supporting finger.

- **Fabrication Process**

To manufacture the compliant finger, hybrid deposition method(HDM) was applied. HDM combines additive manufacturing (AM) process with material deposition and embedded components. HDM process initially prints rigid parts of the mechanism with support structures, adds deposit materials, and removes the support structures [27].

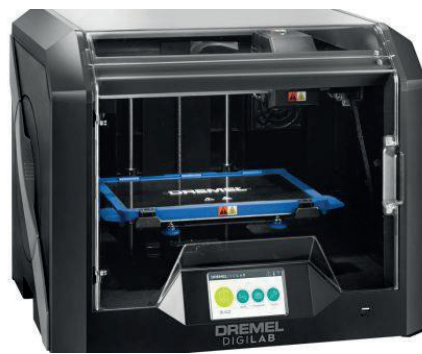


Fig. 2.14. Dremel 3D45 FDM 3D Printer.

To build compliant fingers, the frame of the fingers were 3D printed using 3D45 3D printer from Dremel. Polylactic acid (PLA) and Acrylonitrile butadiene styrene (ABS) filament were used to print. Even though PLA and ABS have different material properties, both filaments are strong enough for this research purpose. The 3D printer that was utilized to print uses fused deposition modeling (FDM) to print the rigid components. A commonly found FDM 3D printer was used to print to demonstrate that this finger manufacturing process does not require a high-quality printer.

Once the rigid frame of the fingers was printed, one side of the finger was taped to prevent the deposit materials for the flexure joints and the pads from leaking out from the designated space. For the fingers, Sylgard 184 Silicone Elastomer (Dow Corning) and PMC 780 (Smooth-On) were used for pads and joints in the corresponding order. Sylgard 184 was mixed with its curing agent in 10:1 ratio and they produce Shore 50A

hardness. PMC 780 has shore 80A hardness. To manufacture the urethanes, the two parts had to be mixed with 2:1 weight ratio and the air bubbles created by mixing the materials were removed ahead of time using a vacuum pump for about 30 minutes. A vacuum chamber can be used to substitute the vacuum pump. Eliminating air bubbles is not a necessary process; however, eliminating air bubbles helps to obtain consistent properties of the flexure joints. In addition, if the joints have excessive air bubbles, they can easily tear apart from fatigue. Once the air bubbles were removed, the deposit materials were poured onto the rigid frame. An excess of materials was removed before they were cured. After curing the materials, all of the sacrificial walls were removed using a utility knife.

2.5 Final Prototype

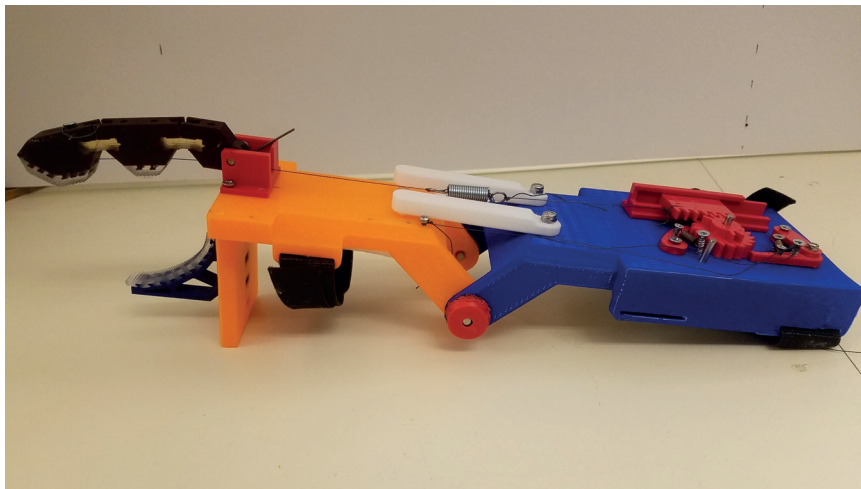


Fig. 2.15. Final Prototype.

Figure 2.15 shows a picture of the prototype. The total cost to build this prototype was 20.20 U.S. dollars. The detailed bill of material can be found in Appendix I. The total weight of this hand is 364.4 grams.

3. ANALYSIS

This chapter presents the preshaping and force analysis. The preshaping analysis helps to estimate how the compliant finger moves as the rotary ratchet rotates. The force analysis was conducted to calculate the contact force that can be generated by the hand and estimate how much load the finger can take.

3.1 Preshaping Analysis

The preshaping refers to the process of change in the configuration of the finger before contacting an object. Once the finger contacts the object, it starts to adapt to the shape of the object as shown in Figure 3.1. For this analysis, the pseudo-rigid body model is used to simplify the analysis of the flexure joints [28–30].

To compute the joint angles, θ_2 and θ_3 , two different methodologies were used: calculating by varying the input force and the rotary ratchet angle, θ_a . Computing the joint angles by changing the input force was performed to verify the results of the preshaping experiment. The behavior of the finger joints was observed in response to increasing the tension of the cable. The other method was performed to simulate the behavior of the finger joints in response to actuating the rotary ratchet which consequently provides an input force, F_a . By doing such simulation, the boundary of position workspace of the finger and the rotation of the finger joints can be determined ahead of time.

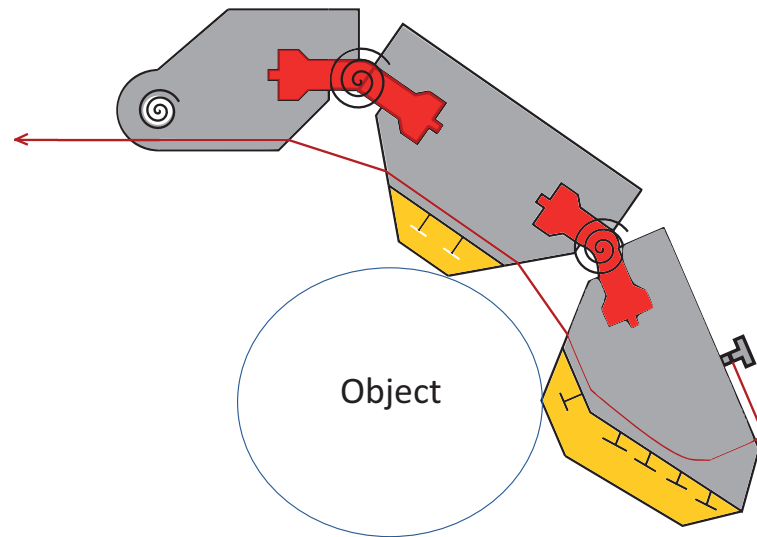


Fig. 3.1. The configuration of the compliant finger when it adapts to a circular shape of the object.

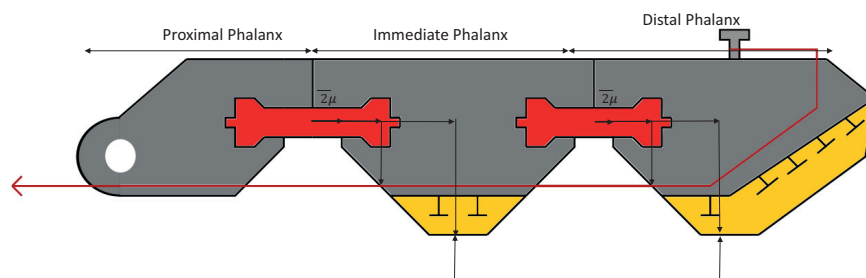


Fig. 3.2. The design of finger with parameters.

3.1.1 Assumptions

The following assumptions were made to proceed with the analysis:

1. It is a quasi-static analysis. The inertial effects are ignored because this hand is operating slowly such that the inertial effects are negligible.
2. An object is small enough such that the proximal joint does not move.
3. The finger phalanges are rigid bodies.
4. Force on an object is perpendicular to the finger pads.
5. The friction between an object and a pad of phalanx is 0.3.
6. The cable does not extend.
7. The joint angle locks when the corresponding finger pad contacts an object or reaches its joint limit

3.1.2 Finger Nomenclatures

Table 3.1.: Finger Parameters.

Symbol	Descriptions
θ_i	The i^{th} joint angle
$\theta_{i_{int}}$	The initial value of i^{th} joint angle
L_i	The length of i^{th} flexure joint
k_i	The rotational stiffness of the i^{th} joint
F_a	The magnitude of the applied cable force
B	The base length of the flexure joints
h	The height of the flexure joints
E	The modulus of elasticity of the flexure joints
I	The moment of inertia of the flexure joints
a_i	The x distance between the center of i^{th} joint and the end of cable route of i^{th} link
b_i	The y distance between the center of i^{th} joint and the end of cable route of i^{th} link
C	The length of cable
R_i	The length of i^{th} link
ϕ	The magnitude of contact angle
d_f	Deflected distance of a spring
k_f	The stiffness of a spring
r_{cix}	The x direction distance between the center of i^{th} joint and the contact location of the corresponding link
r_{ciy}	The y direction distance between the center of i^{th} joint and the contact location of the corresponding link
F_{ix}	The x component of i^{th} link reaction force
F_{iy}	The y component of i^{th} link reaction force

continued on next page

Table 3.1.: *continued*

Symbol	Descriptions
F_{cix}	The x component of i^{th} link contact force
F_{ciy}	The y component of i^{th} link contact force
T	The tension of the cable
γ_i	The angle between i^{th} and $i+1^{th}$ surface of the distal pad
N	The normal force

3.1.3 Flexure Joints

The pseudo-rigid body model (PRBM) is an appropriate model to use for a compliant mechanism. The PRBM simplifies the calculation by modeling a flexure joint as a spring and two rigid links. The representation of PRBM is shown in Figure 3.3. To use this model, it assumes that applied bending moment, τ , is the dominant load

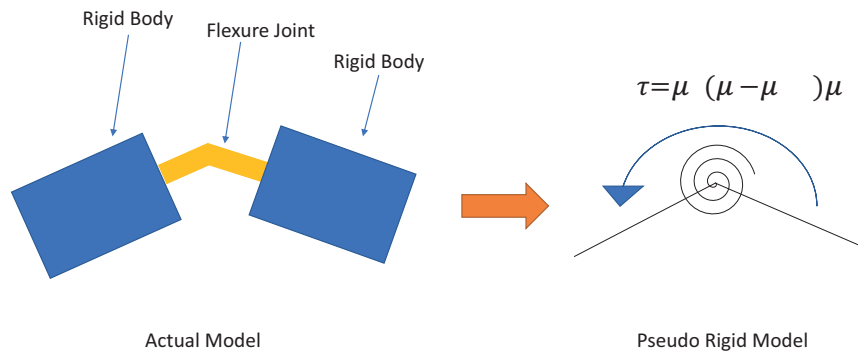


Fig. 3.3. Pseudo rigid body model representation.

compared to the transverse and axial forces applied to the joints. As described in [31], if the length of flexure joints is much smaller than that of rigid links, the approximation is accurate for large deflections as well. However, as the length of a flexure joint gets larger, then the accuracy of this model decreases. The PRBM assumes that a flexure joint acts like a revolute joint with a torsional spring and the center of rotation is at the center of the flexure joint. Figure 3.4 shows the parameters of flexure joints. The stiffness of the flexure joints is calculated using the following Equations 3.1 and 3.2:

$$k = \frac{M}{\theta} = \frac{EI}{L} \quad (3.1)$$

$$I = \frac{Bh^3}{3} \quad (3.2)$$

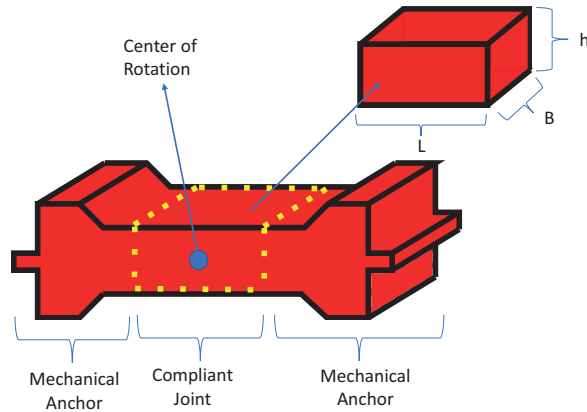


Fig. 3.4. The design of a flexure joint with parameters.

where M is the moment applied to the links, θ is the amount of rotation in the joint, E is the modulus of elasticity, I is the second moment of inertia, L is the arc length of flexure joints, b is the base of flexure joints, h is the height of joint.

3.1.4 Preshaping - Force Control

In this simulation, the force acting on the cable is a variable and based on that force, the distance traveled by the end of cable that is attached to the rack, C , the angle of distal phalanx, θ_3 , and intermediate phalanx, θ_2 , have been computed. Figures 3.5 and 3.6 show the relationship between the direction of the cable and the joint angles. This method is used to simulate the characteristics of the finger joints and to verify the experimental data. For this method, initially, it is assumed that the tension of the cable is consistently applied to each joint; hence, the friction applied on to the cable is negligible.

$$C = r_a \theta_a = \sum_{i=2}^3 (L_i - 2(L_i/2) \cos(\theta_i/2) + 2b_i \sin(\theta_i/2)) \quad (3.3)$$

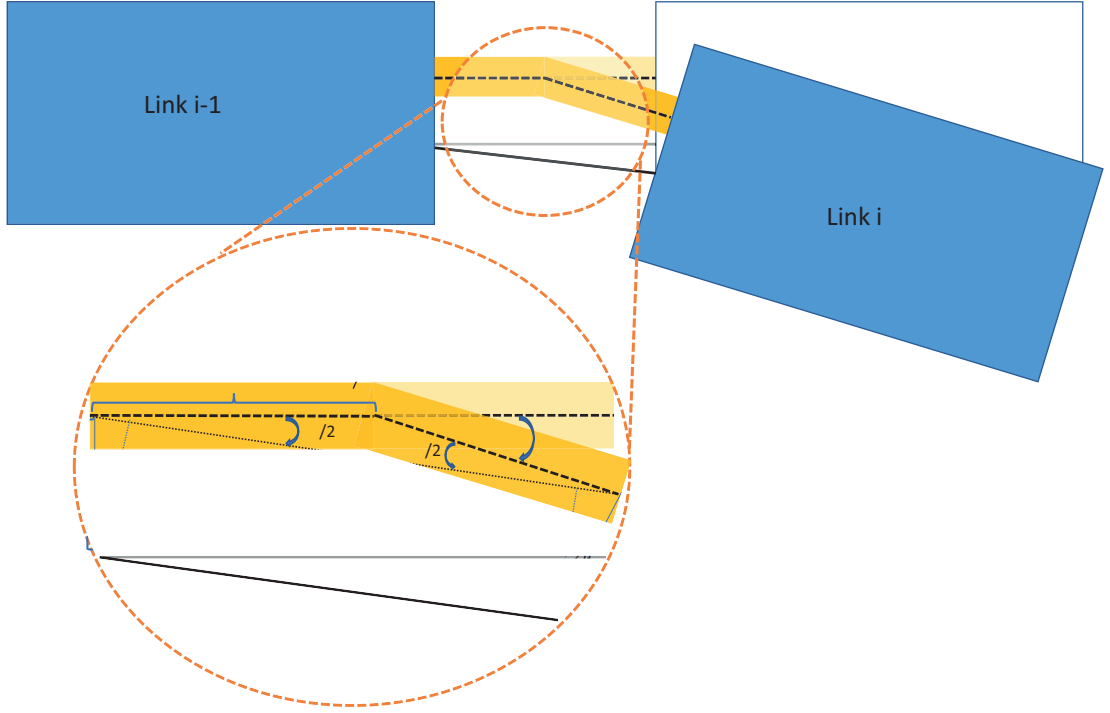


Fig. 3.5. Simplified diagram of a flexure joint.

The distance traveled by the rack can be computed using simple geometry. To simplify the actual model, each link is converted to a rectangle. Similar approach was performed in [32] to compute the joint position of the compliant finger. It was assumed that the flexure joints rotate about their center and the center of joints was not moving. With those assumptions, the geometry shown in Figure 3.5 can be obtained where a flexure joint is composed of two straight, black dotted lines.

Using the FBDs shown in Figure 3.7, Equations 3.4 and 3.5 can be derived.

$$(a_2 \hat{i}_2 + b_2 \hat{j}_2) \times (F_a (\cos(\frac{\theta_2}{2} + \pi)) \hat{i}_2 + F_a (\sin(\frac{\theta_2}{2} + \pi)) \hat{j}_2) + k_2 (\theta_2 - \theta_{2int}) = 0 \quad (3.4)$$

$$(a_3 \hat{i}_3 + b_3 \hat{j}_3) \times (F_a (\cos(\frac{\theta_3}{2} + \pi)) \hat{i}_3 + F_a (\sin(\frac{\theta_3}{2} + \pi)) \hat{j}_3) + k_3 (\theta_3 - \theta_{3int}) = 0 \quad (3.5)$$

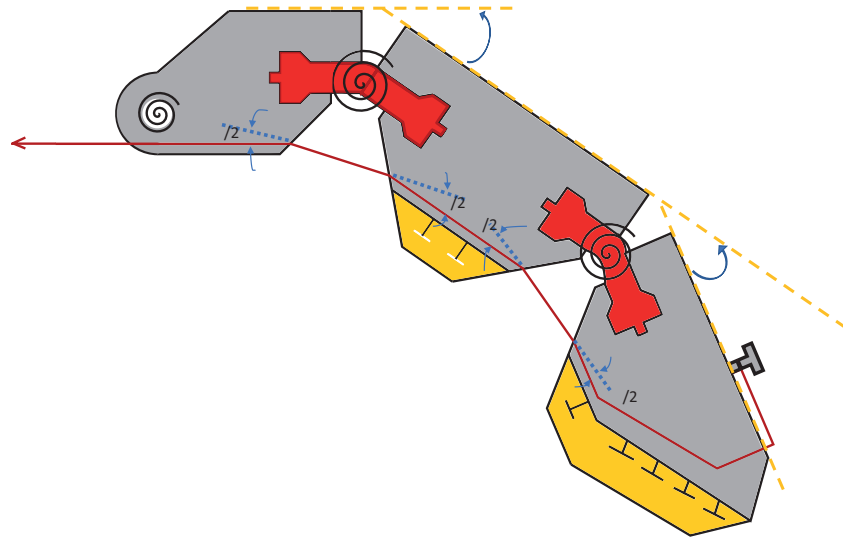
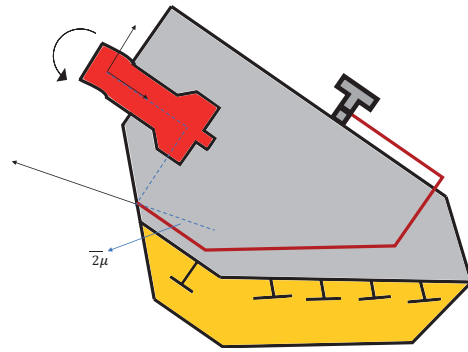


Fig. 3.6. Bent configuration of the compliant finger.

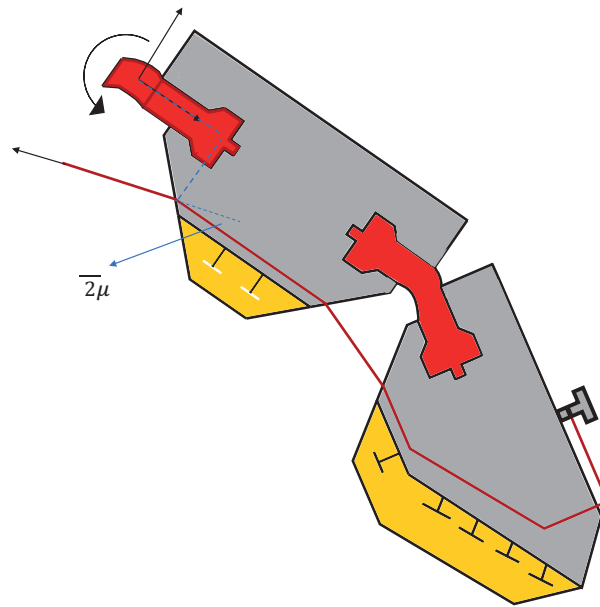
Using the Newton-Ralphson method and solving three equations above simultaneously, the angle of flexure joints and the distance traveled by the rack are computed. Refer to Appendix A for the detailed calculation. Based on those angles, the tension of the cable can be recomputed including the friction applied to the cable.

- **Point Contact Method**

To include the friction effects on the cable, the frictional forces were applied on the contacting points of the phalanges which are the start and the end of the cable route at each phalanx. It was assumed that the cable is only contacting the start and the end of the route and the curvature of the cable route inside of the distal phalanx. The frictional effects were ignored for the cable route in the middle of the phalanges assuming the cable does not touch the surface of that portion of the route. Additionally, it was assumed that the cable is contacting at specific points rather than surfaces since the start and the end of the cable route are sharp edges and the sharp edges have very small contacting surfaces. However, since the cable route inside of the distal phalanx has a curvature, the friction was applied over the surfaces of



(a)



(b)

Fig. 3.7. FBD of the compliant finger during preshaping. (a) DP (b) DP and IP.

that curvature using the capstan equation. The capstan equation, also known as the belt friction equation, is used to recompute the tension of the cable, T , including the effects of the friction. Equation 3.6 shows the general capstan equation. The derivation of this formula is shown in Appendix C.

$$T_{Load} = T_{hold}e^{\mu\phi} \quad (3.6)$$

where T_{load} is the cable facing toward the end of the cable route, T_{hold} is the cable facing toward the start of the cable route, μ is the coefficient of static friction, and ϕ is the total angle contacting the surface of the link. The equation can be modified as shown in Equation 3.22.

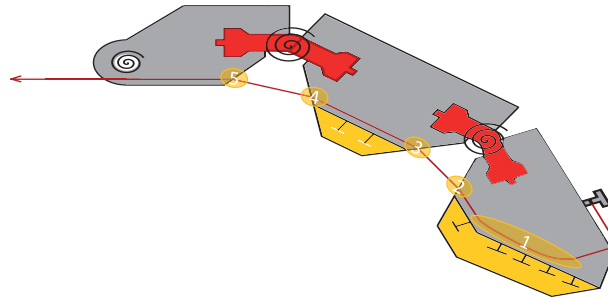


Fig. 3.8. Location of the friction effects where the highlighted regions experience the frictional effects.

For the friction effects around the sharp edges, the point contact friction method was applied. Figure 3.8 shows the locations where the static friction is applied and Figure 3.9 illustrates the FBD of the cable at different locations of the cable route.

The direction of the normal force was assumed to be half of the angle of the applied force at each joint. Using the free body diagrams of each section of the cable, the force and moment equations can be found. Refer to Appendix B for detailed calculations.

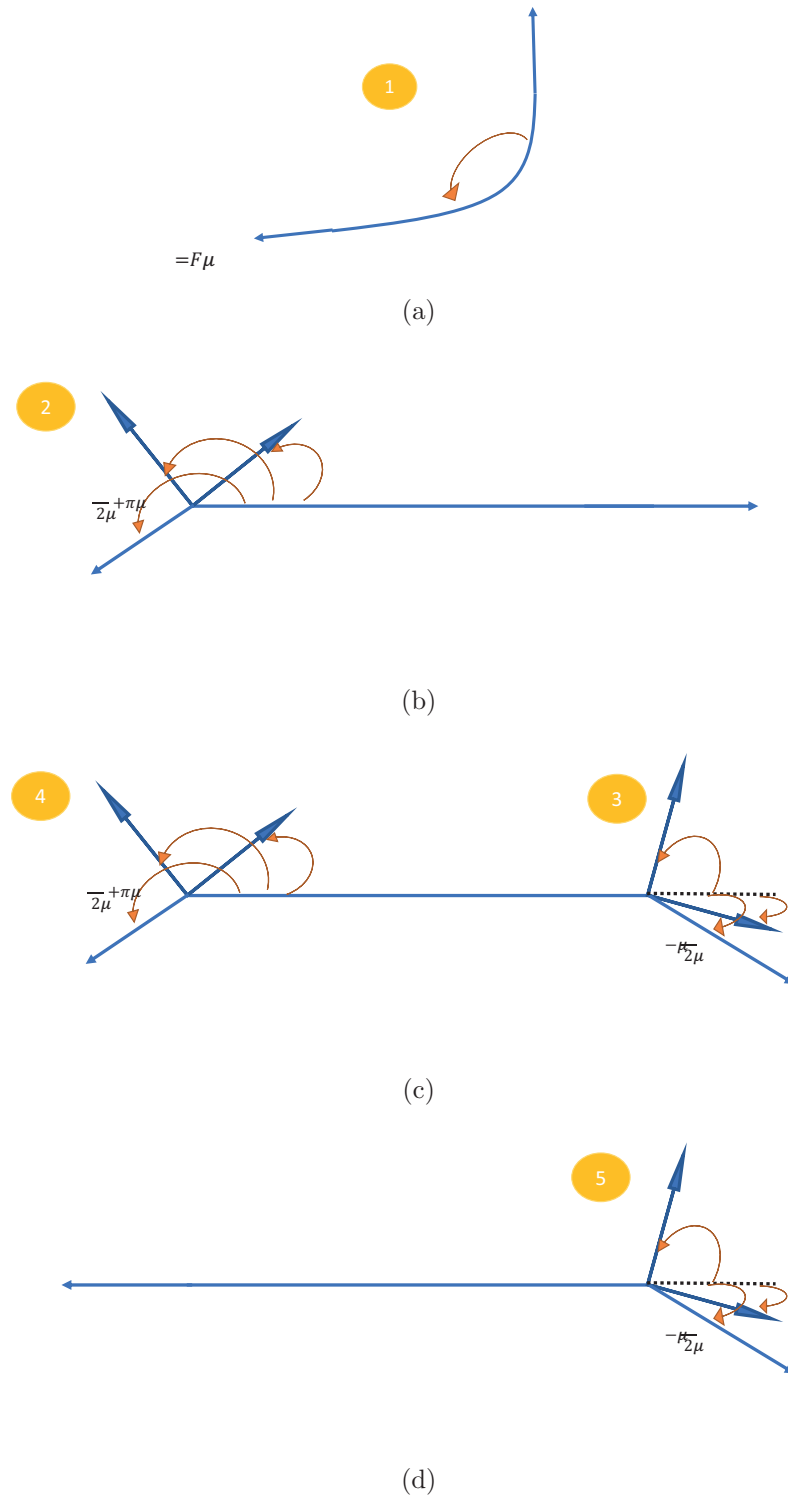


Fig. 3.9. FBD of the cable at different location of the cable route (a) Partial FBD of the cable at the curvature of the route (b) FBD of the cable at the end of the route inside of the DP (c) FBD of the cable at the IP (d) FBD of the cable at the PP.

$$F_x = 0 = N_1 \cos(\alpha_1) + N_1 \mu \cos(\beta_1) + F_{a2} \cos(\theta_3/2 + \pi) + F_{a1} \quad (3.7)$$

$$F_y = 0 = N_1 \sin(\alpha_1) + N_1 \mu \sin(\beta_1) + F_{a2} \sin(\theta_3/2 + \pi) \quad (3.8)$$

where

$$\alpha_1 = \frac{\theta_3/2 + \pi}{2} \quad (3.9)$$

$$\beta_1 = \theta_3/4 \quad (3.10)$$

$$\begin{aligned} F_x = 0 = & N_2 \cos(\alpha_2) + N_2 \mu \cos(\beta_2) + N_3 \cos(\alpha_3) + N_3 \mu \cos(\beta_3) \\ & + F_{a3} \cos(\theta_2/2 + \pi) + F_{a2} \cos(\theta_3/2) \end{aligned} \quad (3.11)$$

$$\begin{aligned} F_y = 0 = & N_2 \sin(\alpha_2) + N_2 \mu \sin(\beta_2) + N_3 \sin(\alpha_3) + N_3 \mu \sin(\beta_3) \\ & + F_{a3} \sin(\theta_2/2 + \pi) + F_{a2} \sin(\theta_3/2) \end{aligned} \quad (3.12)$$

$$\begin{aligned} M = 0 = & -R_2 \hat{i} \times ((N_3 \cos(\alpha_3) + \mu \cos(\beta_3) + F_{a3} \cos(\theta_2/2 + \pi)) \hat{i} \\ & + (N_3 \sin(\alpha_3) + \mu \sin(\beta_3) + F_{a3} \sin(\theta_2/2 + \pi)) \hat{j}) \\ = & -R_2 (N_3 \sin(\alpha_3) + \mu \sin(\beta_3) + F_{a3} \sin(\theta_2/2 + \pi)) \end{aligned} \quad (3.13)$$

where

$$\alpha_2 = -\theta_3/4 + \pi/2 \quad (3.14)$$

$$\beta_2 = -\theta_3/4 \quad (3.15)$$

$$\alpha_3 = \theta_2/4 + \pi/2 \quad (3.16)$$

$$\beta_3 = \theta_2/4 \quad (3.17)$$

$$F_x = 0 = N_4 \cos(\alpha_4) + N_4 \mu \cos(\beta_4) - F a_4 \quad (3.18)$$

$$F_y = 0 = N_4 \sin(\alpha_4) + N_4 \mu \sin(\beta_4) \quad (3.19)$$

where

$$\alpha_4 = -\theta_2/4 + \pi/2 \quad (3.20)$$

$$\beta_4 = -\theta_3/4 \quad (3.21)$$

In Equations 3.7, 3.8, 3.11 to 3.13, 3.18, and 3.19, α and β define the direction of corresponding normal force and friction force respectively. By solving Equations 3.7, 3.8, 3.11 to 3.13, 3.18, and 3.19, consecutively, the tension of the cable including the effects of friction can be solved. For the experiment that will be discussed in Chapter 5, an additional frictional effect is considered using the capstan equation assuming the total contact angle around the pulley is 90 degrees.

• Capstan Equation Method

Initially, in the previous section, it was assumed that the cable only contacts at certain points rather than surfaces. However, for the real system, the cable wraps around the surfaces of the sharp edges. Thus for the real system, the friction must be applied over those contacting surfaces, rather than at a contacting point of those edges [15]. As the finger bends, the cable wraps around the surfaces more, which increases the frictional force on the cable. To apply the effects of friction around the contacting surfaces, the capstan equation, also known as the belt friction equation, was used to recompute the tension of the cable. For this analysis, it was assumed there are some curvatures on the sharp edges as if there is a tiny pulley on each edge. The capstan

equation, Equation 3.6 can be modified as shown in Equation 3.22. Equation 3.22 multiples the frictional effects by using the capstan equation.

$$F_a = F_{a0} \prod_{j=1}^5 e^{(\mu\phi_j)} \quad (3.22)$$

where F_a is the input force and F_{a0} is the initial tension of the cable which is not affected by the friction. As the cable passes through the locations shown in Figure 3.10, the tension of the cable grows due to the effects of the friction to result in the input force, F_a . As can be seen from the capstan equation, Equation 3.6, the radius of the capstan does not affect the frictional resistance as long as the coefficient of friction and the contact area are the same. As described by [33], as the radius of the capstan increases, the local friction forces and the local normal forces become smaller and apply over the larger contacting surface. Vice versa, as the radius of the capstan decreases, the local friction forces and the local normal forces get larger and apply over the smaller contacting surface. Consequently, both cases produce the equal amount of total frictional force.

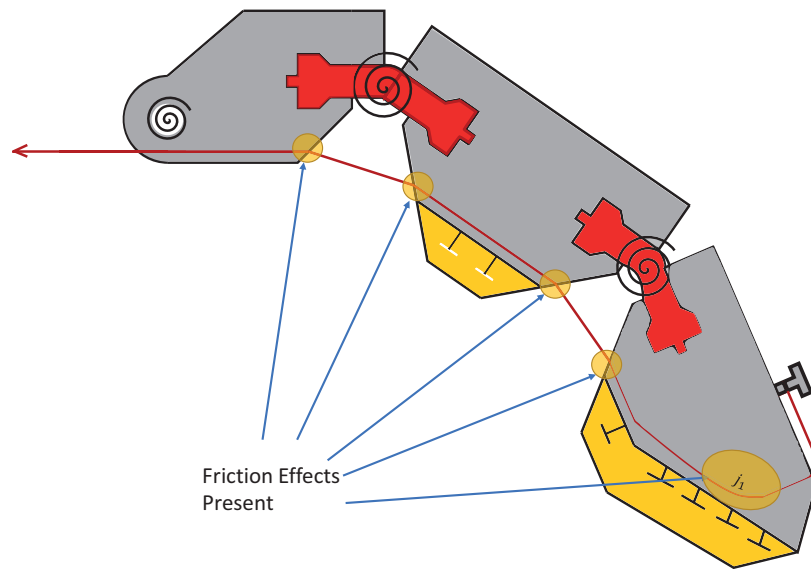


Fig. 3.10. Location of the capstan effect.

The total contacting angle on each edge of the cable route is assumed as $\theta_i/2$ since the direction of the cable needs to change twice when the corresponding joint changes its angle as shown in Figure 3.6 and the contacting angle inside the distal phalanx needs to be determined based on the shape of the cable path. Additionally, for the preshaping experiment that will be described in Chapter 4, the cable goes around a pulley and the contacting angle around the pulley was 90 degrees. The friction effects had been taken into account accordingly.

3.1.5 Preshaping - Rack Actuated Distance Control

To simulate the trajectory of the finger on the actual system, the control variable needs to be the angle of the actuator, which essentially controls how far the cable has been pulled back. Similar to the previous method, initially, the tension of the cable is consistent throughout each link and the effects of friction are neglected. For this method, the input force is initially unknown, but the angle of the rotary ratchet is

defined and known. Two moment equations, Equations 3.4 and 3.5, are combined as shown in Equation 3.23. Refer to Appendix A for the further details.

$$\begin{aligned} & (a_2 \sin(\frac{\theta_2}{2} + \pi) - b_2 \cos(\frac{\theta_2}{2} + \pi))k_3(\frac{\theta_3}{2} - \theta_{3int}) \\ & - (a_3 \sin(\frac{\theta_3}{2} + \pi) - b_3 \cos(\frac{\theta_3}{2} + \pi))k_2(\theta_2 - \theta_{2int}) = 0 \end{aligned} \quad (3.23)$$

Similarly, to solve Equations 3.23 and 3.3, the cable kinematic equation shown in the earlier section, the Newton-Ralphson method has been applied. Further details can be found in the Appendix A. Equation 3.24 computes the tension of the cable without the friction effects.

$$F_a = -\frac{k_2(\theta_2 - \theta_{2int})}{a_2 \sin(\theta_2/2 + \pi) - b_2 \cos(\theta_2/2 + \pi)} \quad (3.24)$$

Using the angles of each joint, the tension of the cable is recalculated including the effects of static friction using the capstan equation as shown in Equation 3.25.

$$F_a = -\frac{k_2(\theta_2 - \theta_{2int})}{a_2 \sin(\theta_2/2 + \pi) - b_2 \cos(\theta_2/2 + \pi)} \prod_{j=1}^5 e^{(\mu\phi_j)} \quad (3.25)$$

As described previously, ϕ_j is the total contacting angle and j is the location of capstan effect as shown in Figure 3.10. The first contacting angle needs to be determined from the path of cable route of distal phalanx and for the rest of the contacting angles, they depend on the joint angles. For this specific finger, ϕ_{j_2} and ϕ_{j_3} depend on the distal joint angle, $\theta_3/2$ and ϕ_{j_4} and ϕ_{j_5} depend on the intermediate joint angle, $\theta_2/2$. Similar to the input force controlled case, the point contact method can be applied for this analysis to calculate the input force including the frictional effects.

3.1.6 Mechanical Fuse Effect

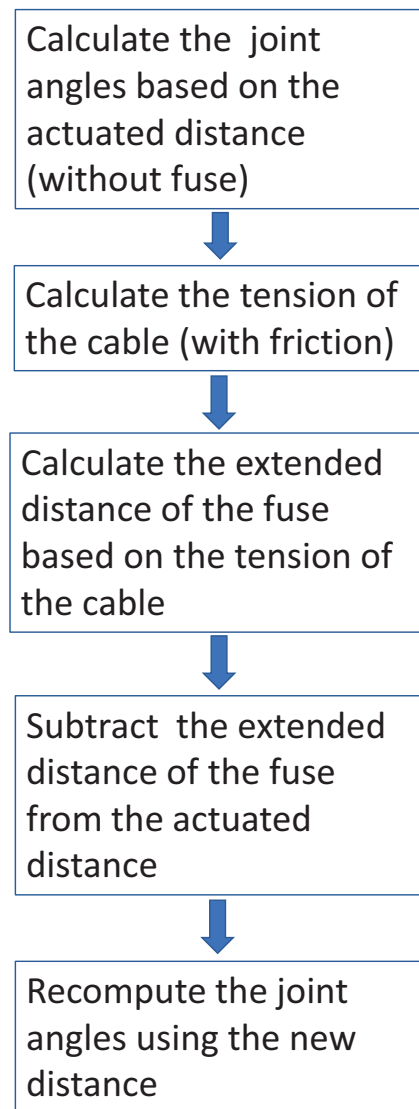


Fig. 3.11. Joint angle computation process including a mechanical fuse.

Initially, every time the rack is moved by the rotary ratchet, the amount of distance moved by the rack is compensated by reducing the length of the cable that goes through the finger by bending the joints. However, if the joints reach their joint limits or if they contact an object, the joints cannot be rotated further unless applying enough force to break the system or deform the object. Thus, for the actual system,

a spring is attached between the finger and the rack to act as a fuse. A fuse allows the finger joints to bend after their joint limits or contacting an object by taking up the additional input force from the rack and extending accordingly. In addition, by extending this spring while actuating, it allows the finger joints to bend less. Without the fuse, the finger almost reaches its joint limits or touches the object even before the rotary ratchet is fully actuated because the direction of the cable is changed as the wrist flexes to actuate. However, the new direction of the cable, pointing toward the top surface of the gauntlet, requires a longer length of cable between the finger and the rack. Figure 3.11 shows the flowchart of how the joint angles of the finger are computed including the mechanical fuse. Using the tension of the cable with the friction effects, the extended length of the spring can be calculated using Equation 3.26.

$$F_a = k_f * d_f \quad (3.26)$$

The distance moved by the rack can be computed using Equation 3.27.

$$C = r_a \theta_a - d_f \quad (3.27)$$

By substituting the distance traveled by the rack in Equation 3.3 with Equation 3.27, the equation can be modified as Equation 3.28.

$$C = r_a \theta_a - d_f = \sum_{i=2}^3 (L_i - 2(L_i/2) \cos(\theta_i/2) + 2b_i \sin(\theta_i/2)) \quad (3.28)$$

Finally, using Equations 3.23 and 3.28, the joint angles of the finger with a mechanical fuse can be computed.

3.2 Preshaping Analysis Results and Discussion

When this analysis was performed, it was assumed that the proximal joint is not moving; therefore, the preshaping results of the proximal joint angle were omitted. The size of intermediate phalanx joint used to calculate the joint angle was 7mm x 13mm x 5.5mm (L x B x h). The size of distal phalanx joint used to calculate the joint angle was 8mm x 13mm x 5.5mm (L x B x h). The young's modulus of the polyurethane was 276 MPa. Correspondingly, each size results in a stiffness of 0.0621 Nm/rad (intermediate joint) and 0.0710 Nm/rad (distal joint) using Equations 3.1 and 3.2.

3.2.1 Force Control Results

As described in the previous section, the input force, F_a , is the control variable for this analysis. By changing the magnitude of the input force by a constant amount, θ_2 and θ_3 were calculated. Figure 3.12 shows how θ_2 and θ_3 change with respect to F_a when the effects of friction are ignored. As shown in Figure 3.12, θ_2 changes at a faster rate than θ_3 , which is expected because the stiffness of the distal joint is slightly greater than that of the intermediate joint.

Using the computed joint angles, the tension of the cable with the effects of static friction was computed by including the capstan effects. Figure 3.13 shows the changes in joint angles with respect to F_a including the friction effects using the capstan equation method. As shown from Figures 3.12 and 3.13, the effect of the friction is significant. When the effect of the friction is considered, to actuate the same amount of angle, the input force almost quadrupled. Additionally, when the friction effects are included, Figure 3.13 indicates that it is harder to bend the joints because the cable wraps around more surfaces of the edges which makes it harder to pull the cable. According to the capstan equation, the input force needs to exponentially increase.

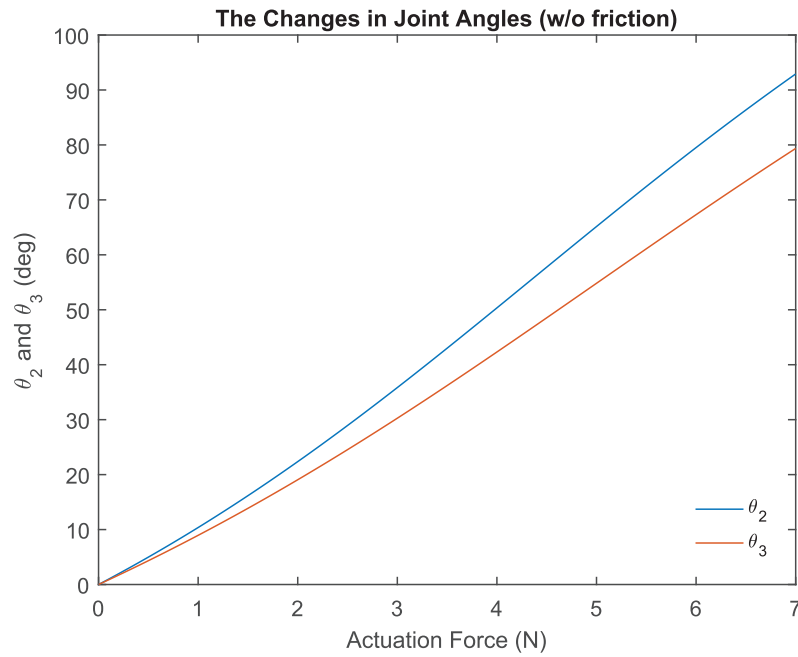


Fig. 3.12. The change in the joint angle of the phalanges without friction.

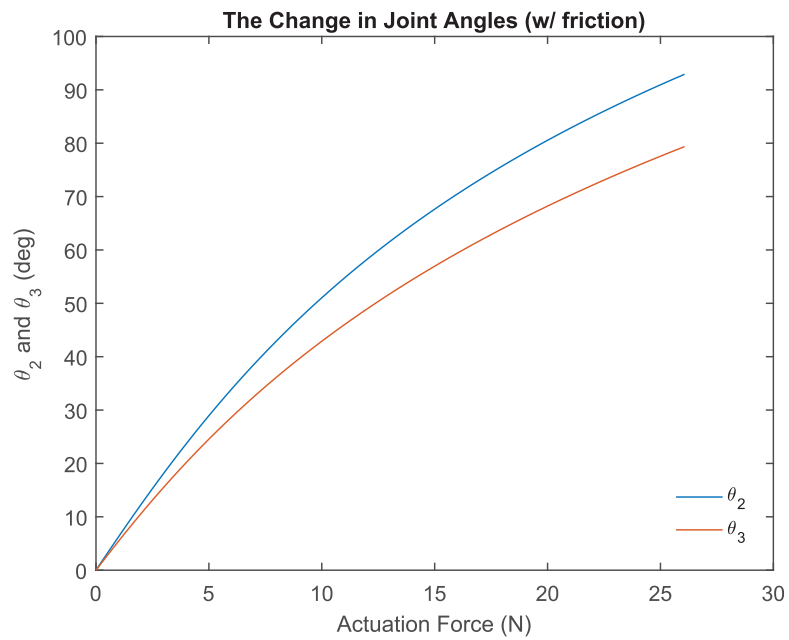


Fig. 3.13. The change in the joint angle of the phalanges with friction.

To compare the effectiveness of point contact method and the capstan equation, the joint angle plots are shown in Figure 3.14. As shown from Figure 3.14, there is not significant difference between two methods. From the results, it can be inferred that either method can be used to determine the tension of the cable and the friction on a sharp edge acts as if the cable is experiencing the friction effect on a contacting point because the contacting surface is small.

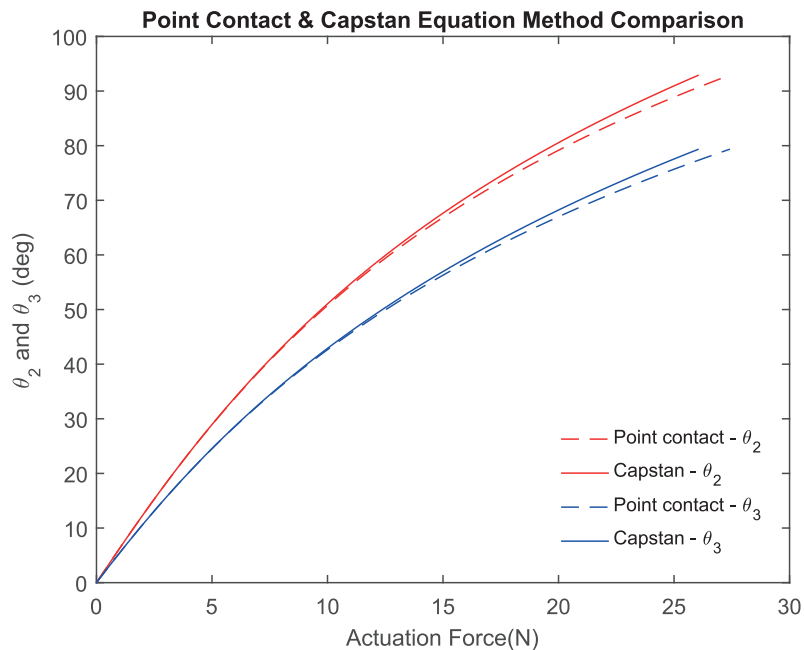


Fig. 3.14. Comparison of the point contact method and the capstan equation method.

If the intermediate link reaches its joint limit, 90 degrees, or if it touches an object, then the intermediate link stops moving and locks at that position. Consequently, only the distal link is able to move. Once θ_2 reaches its limit, the rate of change in θ_3 , $d\theta_3/d\theta_a$, changes to a much faster rate because the joints are no longer coupled and the distance traveled by the rack, C , directly changes θ_3 only.

$$C = r_a \theta_a = L_3 - 2(L_3/2) \cos(\theta_3/2) + 2b_3 \sin(\theta_3/2) \quad (3.29)$$

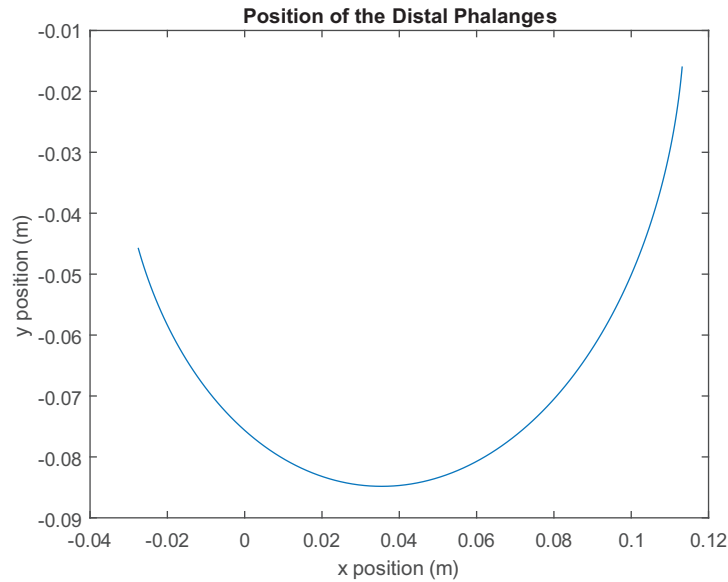


Fig. 3.15. The trajectory of the tip of finger.

Using the forward kinematics and the calculated joint angles, the trajectory of the finger tip was calculated. As mentioned before, it was assumed that the angle of the proximal joint is fixed at 8 degrees. The forward kinematic equations, Equations 3.30 and 3.31,

$$x_{position} = R_1 \cos(\theta_1) + R_2 \cos(\theta_1 + \theta_2) + R_3 \cos(\theta_1 + \theta_2 + \theta_3) \quad (3.30)$$

$$y_{position} = R_1 \sin(\theta_1) + R_2 \sin(\theta_1 + \theta_2) + R_3 \sin(\theta_1 + \theta_2 + \theta_3) \quad (3.31)$$

The trajectory of the tip of finger defines the outer boundary of the position workspace. Additionally, the result of this calculation was necessary information to design the size and location of the stationary finger. Figure 3.15 shows the trajectory of the distal phalanx using forward kinematics.

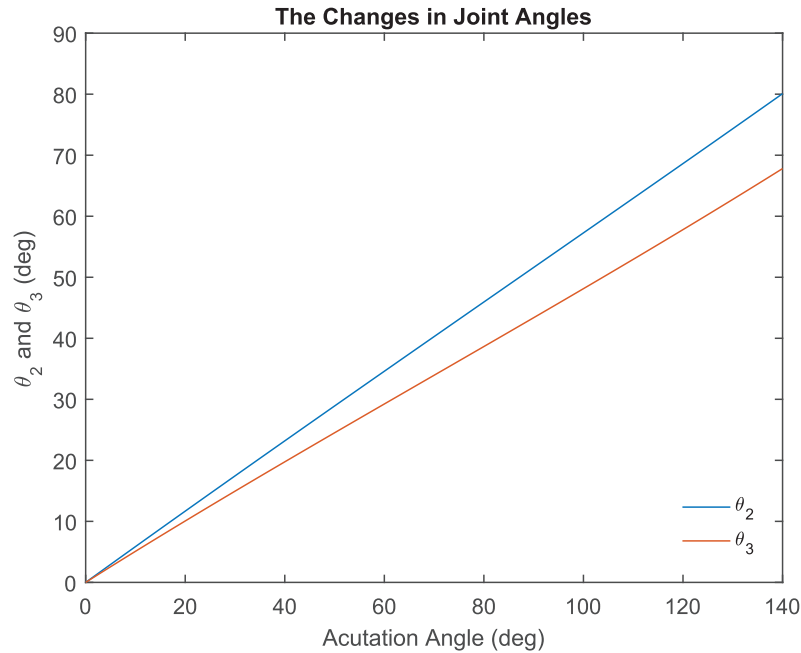


Fig. 3.16. The change in joint angles as actuator angle changes. The blue line represents θ_2 . The red line represents θ_3 .

3.2.2 Rack Actuated Distance Control Results

To estimate the actual trajectory of the finger, the distance traveled by the rack was controlled by varying the angle of the actuator. Figure 3.16 shows the changes in joint angles as the actuator angle changes. Because the joint angles depend only on the distance traveled by the rack, the static friction does not affect the results of the joint angles. The static friction makes the rack harder to pull, but it does not necessarily influence the movement of the joint angles. When the effects of static friction are present, the rotary ratchet needs to be able to withstand a greater amount of applied force. In addition, including the static friction, the pawl needs to exert a greater amount of force to actuate the rotary ratchet. Hence, the user needs to generate a higher torque from their wrist to actuate. Figure 3.17 compares the magnitude of input force without friction and with friction. It can be inferred that the tension of

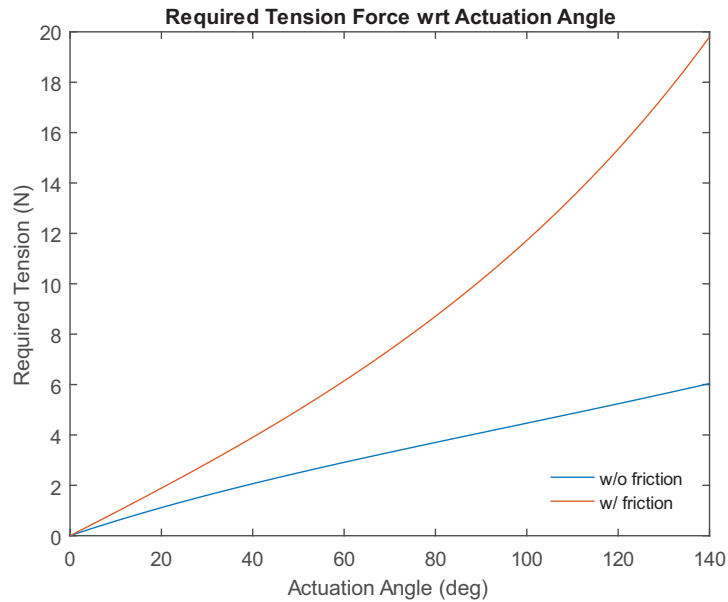


Fig. 3.17. Required force to actuate based on the actuation angle. The blue line represents the tension of the cable without friction. The red line represents the tension of the cable with friction.

the cable is mostly dominated by the force to overcome the friction force and this force increases as the finger curves more due to the capstan effect. When designing a hand, the tension of the cable needs to be examined because depending on the level of amputation and the age of the users, the range of torque generated from the wrist varies. Based on the level of amputation, the users will activate a different set of muscles to bend their wrist. This would be a potential area for future research.

3.2.3 Mechanical Fuse Results

For the actual system, a spring is attached between the finger and rack. When the rotary ratchet is actuated to curl the finger, the spring starts to extend as tension builds up on the cable. As seen from the previous section, the joint angles of the finger depend on the distance traveled by the rack. When a spring is not present,

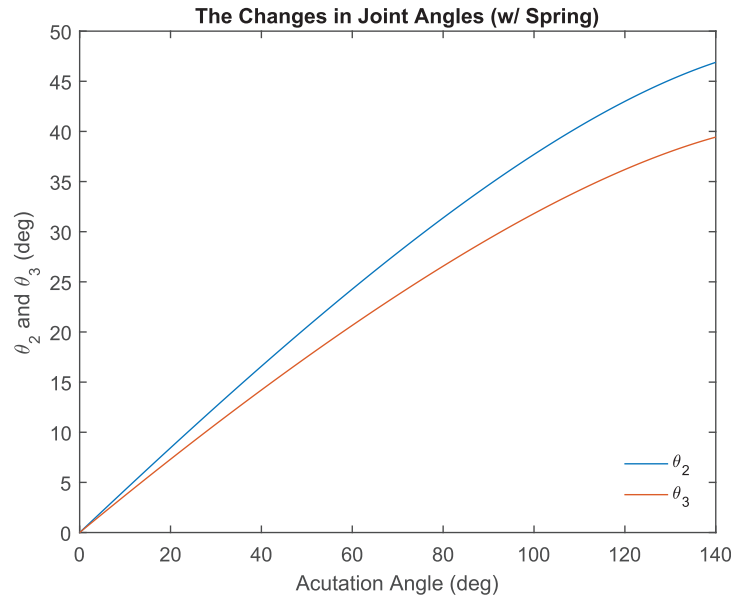


Fig. 3.18. The change in the joint angles as the actuation angle changes with spring.

such distance is reflected only on the joint angles. Therefore, once the joints are locked, the rack cannot be further moved. However, when a spring is included as a part of the system, not all the distance is reflected on the joint angles, rather a part of the distance moved is taken up by the deflection of the spring because the force is applied onto the spring to extend. As the input force increases, the spring extends more to generate an equivalent tension. As shown Figure 3.18, the joint angles are significantly reduced to compensate the deflection of the spring compared to Figure 3.16 which does not include the effect of a spring. Based on the stiffness of the spring, the trajectory of a finger can be further controlled. When the stiffness of the spring is low, the finger changes less because the spring needs to deflect more to produce an equal amount of tension.

3.3 Force Analysis

In this section, the contact force between an object and a finger is analyzed. It is important to calculate an approximate magnitude of contact force to predetermine the range of weight of an object that the hand can lift up. The tightness of the gripping force is mainly controlled by the tension of the cable, which depends on the angle of the rotary ratchet. As the tension of cable increases, the contacting force on an object increases proportionally. Additionally, the contacting location of the links and the object and the joint position of the links affect the magnitude of the contact force.

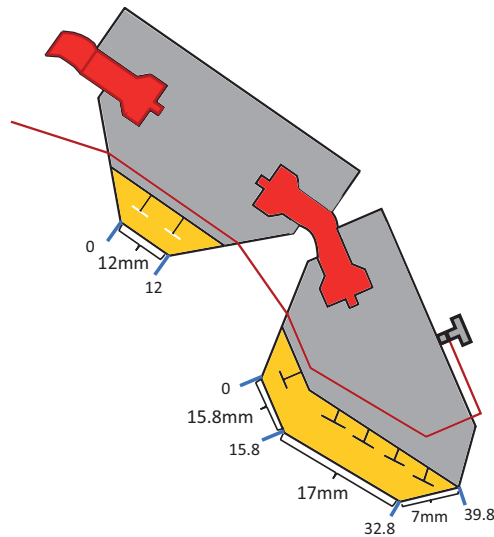


Fig. 3.19. Diagram of the finger with contacting distance labels.

3.3.1 Analysis

For this specific analysis, the effects of contact locations and joint angle positions had been analyzed. Using the moment equations shown in Equations 3.32 and 3.33 based on FBDs shown in Figure 3.20, the contact forces were calculated. Given an

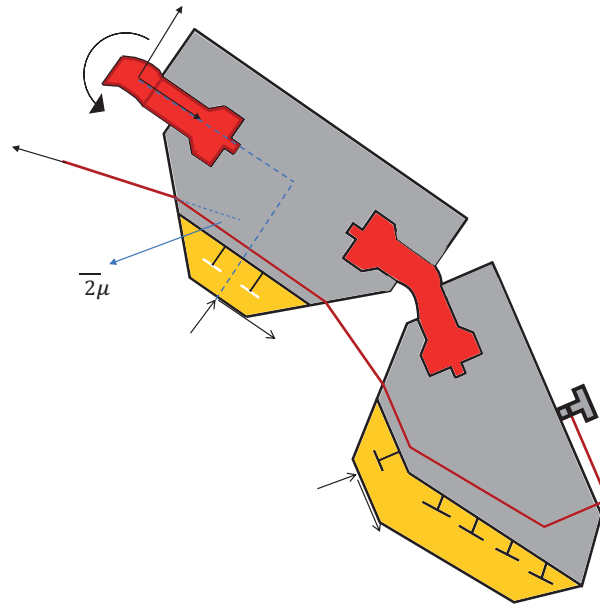
arbitrary tension of the cable, initially, the joint angles were varied and the contact locations were fixed at 21.88 mm (6.02 mm relatively) and at 23.28 mm (7.91 mm relatively) for the IP and DP respectively. Figure 3.19 indicates the relative finger contacting distances. In Figure 3.20(b), the numbers on the DP indicate the contact regions; the slopes of those regions all differ. Therefore, the coordinate needs to be transformed accordingly. Assuming the PP stays at the initial angle and the contact forces are acting perpendicularly, the moment equations of the intermediate and distal phalange were derived.

A stable region needs to have positive contact forces for both phalanges and requires tension on the cable. When the magnitude of the arbitrary tension is less than that of the tension required to hold the joints at a specific position, then it is defined as cable slacking. After the effects of joint angles were determined, the joint angles were fixed at a certain configuration and the contact locations were varied to further increase the size of the stable region.

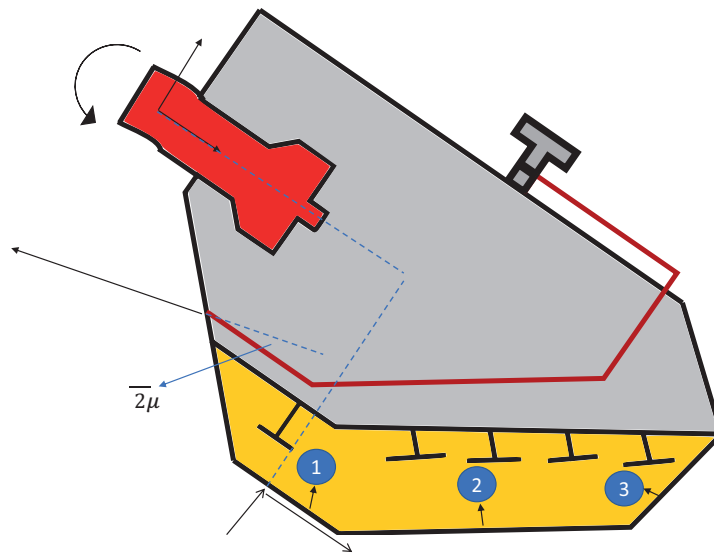
$$\begin{aligned} (a_3\hat{i}_3 + b_3\hat{j}_3) \times (F_{a3x}\hat{i}_3 + F_{a3y}\hat{j}_3) + (r_{c3x}\hat{i}_3 + r_{c3y}\hat{j}_3) \times (F_{c3x}\hat{i}_3 + F_{c3y}\hat{j}_3) \\ + k_3(\theta_3 - \theta_{3int}) = 0 \end{aligned} \quad (3.32)$$

$$\begin{aligned} (a_2\hat{i}_2 + b_2\hat{j}_2) \times (F_{a2x}\hat{i}_2 + F_{a2y}\hat{j}_2) + (r_{c2x}\hat{i}_2 + r_{c2y}\hat{j}_2) \times (F_{c2x}\hat{i}_2 + F_{c2y}\hat{j}_2) \\ (R_2\hat{i}_2 + r_{c3x}\hat{i}_3 + r_{c3y}\hat{j}_3) \times (F_{c3x}\hat{i}_3 + F_{c3y}\hat{j}_3) + k_2(\theta_2 - \theta_{2int}) = 0 \end{aligned} \quad (3.33)$$

Refer to Appendix D for the detailed calculation



(a)



(b)

Fig. 3.20. FBD of the phalanges with contact forces (a)IP and DP (b)DP.

3.3.2 Results

The range of both joint angles are 0 to 85 degrees. The range of contacting distance of IP pad is 12.04 mm and that of DP pad is 39.82 mm. However, for the DP, there are three contact regions as shown in Figure 3.20(b). The slope between contact region 1 and 2 is 42.34 degrees and the slope between contact region 2 and 3 is 47.66 degrees.

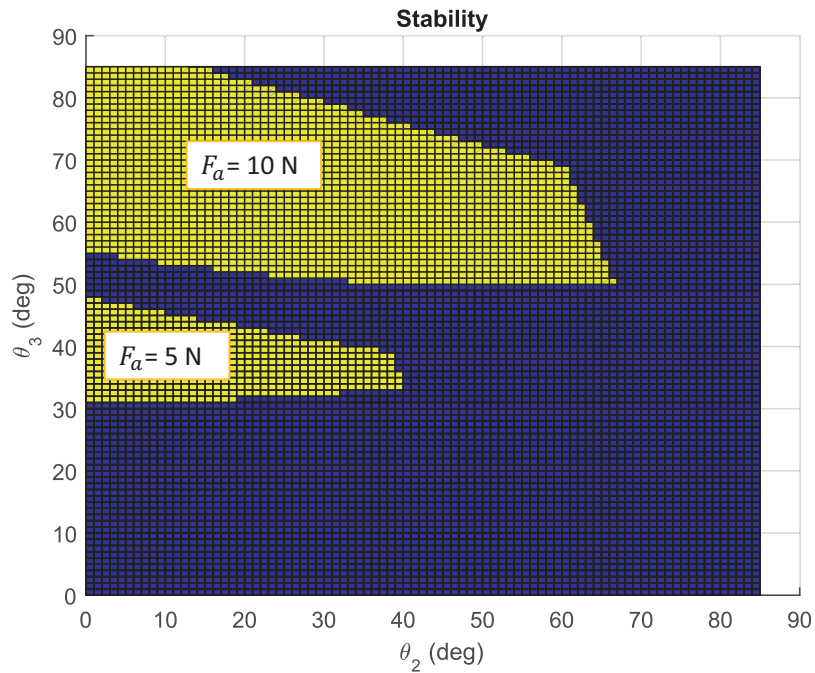


Fig. 3.21. Stability where DP contact location is 7.91 mm away relatively and IP contact location is 6.02 mm away relatively. The yellow regions represent a stable region and the dark blue region represents an unstable region.

Given the arbitrary tensions of the cable, 5 N and 10 N, in Figure 3.21, the yellow regions represent the contact force at the DP when the contact force at the IP are both positive and the input cable is not slacking. As the joints curl more, the required tension to be at those positions increase. When the cable slacks, the finger cannot further preshape since the input tension is not enough to move to the subsequent position. In other words, the yellow regions are the stable regions where

both phalanges have successfully wrapped around and contacted an object. As shown in Figure 3.21, when the tension of the cable is reduced from 10 N to 5 N, the stable region shifts down and becomes smaller. When the tension of the cable is low, the joint angles need to move further away from the maximum joint angles because the required tension to maintain such positions increases. The dark blue region in Figure 3.21 represents either one of the contact forces is less than zero or the cable is slacking. The dark blue region is where the compliant finger is not able to wrap around and grasp the object or the configuration of the finger is not possible since the tension of the cable is too low. The stable and unstable regions could change when the input tension or the contact location varies.

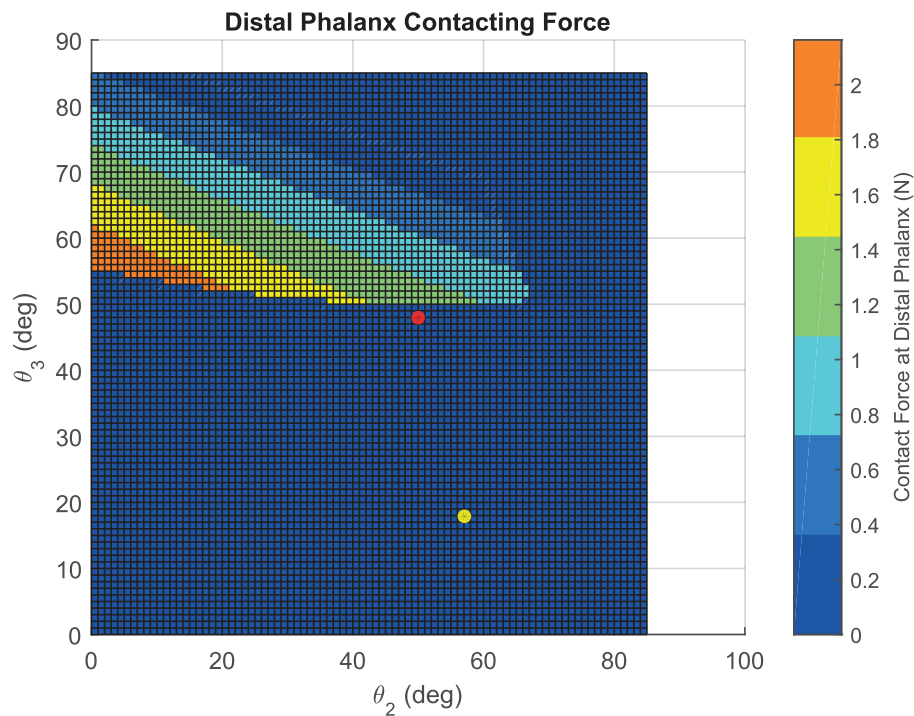


Fig. 3.22. Effects of the joint angles on the contact force produced by the DP. Contact location is at 21.88 mm (6.02 mm for the relative distance) for the IP and 23.28 mm (7.91 mm for the relative distance) for the DP.

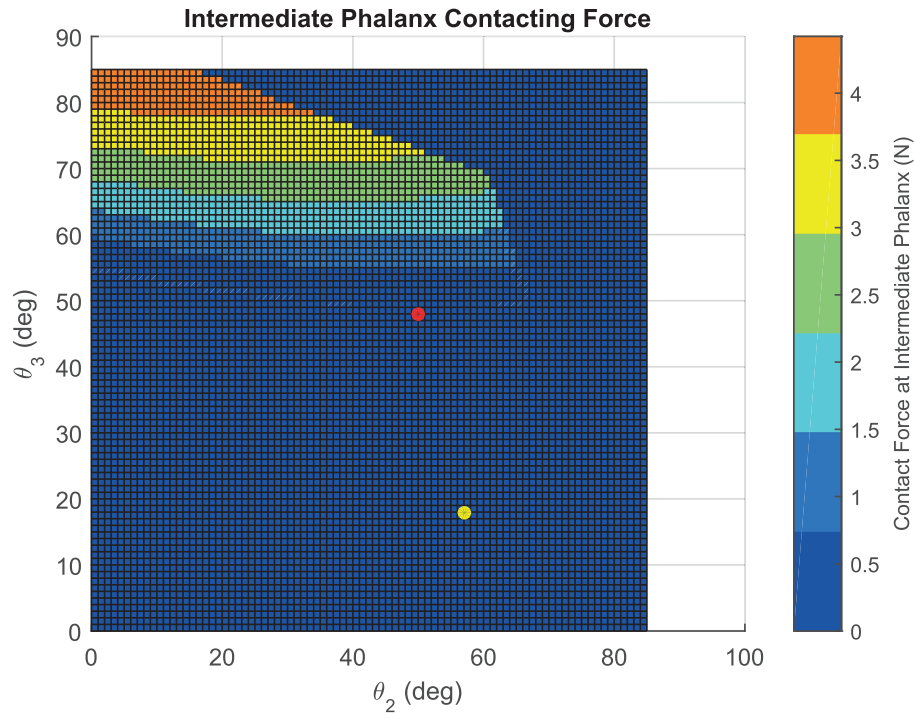


Fig. 3.23. Effects of the joint angles on the contact force produced by the IP. Contact location is at 21.88 mm (6.02 mm for the relative distance) for the IP and 23.28 mm (7.91 mm for the relative distance) for the DP.

Figure 3.22 shows the magnitude of the contact force at the DP including the mask from Figure 3.21. The dark blue region in Figure 3.22 represents where the grasp is unstable assuming the object is contacting at the center of the contact region 1 of the DP. As shown from the plot, the contact force at the DP increases as the intermediate joint angle gets smaller. In Figure 3.23, the contact force at the IP is higher when the contact force at the DP is low. From Figure 3.22 and 3.23, it can be inferred that the total amount of the contact force that can be generated from two phalanges is limited by the tension of the cable.

To further increase the area of the stable regions illustrated from Figure 3.21, the contact locations of two phalanges had been varied. As shown from Figure 3.24 and 3.25, the effects of the contact locations are small, but varying the contact locations helps to increase the size of the stable region. However, if the original configuration

is far apart from the stable region such as the configuration shown in Figure 3.22 and 3.23 as a yellow point, then the corresponding configuration would remain unstable; the effects of the contact location is small to change the magnitude of the contact forces significantly.

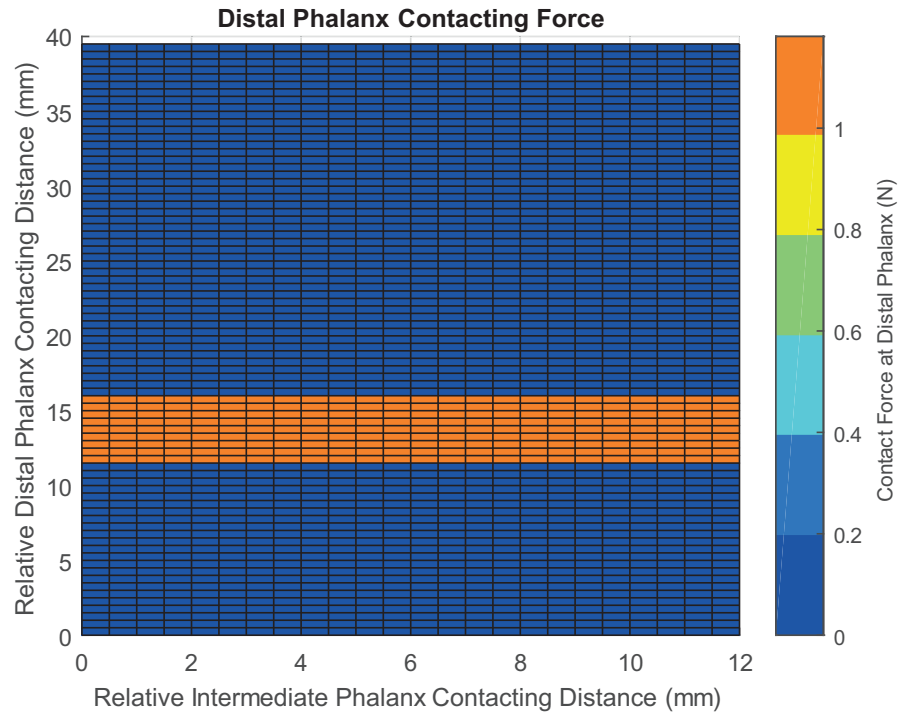


Fig. 3.24. Effects of the contact locations on the contact force produced by the DP when the DP is at 48 deg and the IP is at 50 deg.

In Figure 3.22 and 3.23, when the intermediate joint is at 50 degrees and the distal joint is at 48 degrees, represented as a red point, the configuration is unstable. However, in Figure 3.24 and 3.25, the configuration becomes stable once the contact locations of the DP and the IP change where the color of the unstable region is dark blue. If the configuration is close to the stable region, changing the contact locations helps to stabilize.

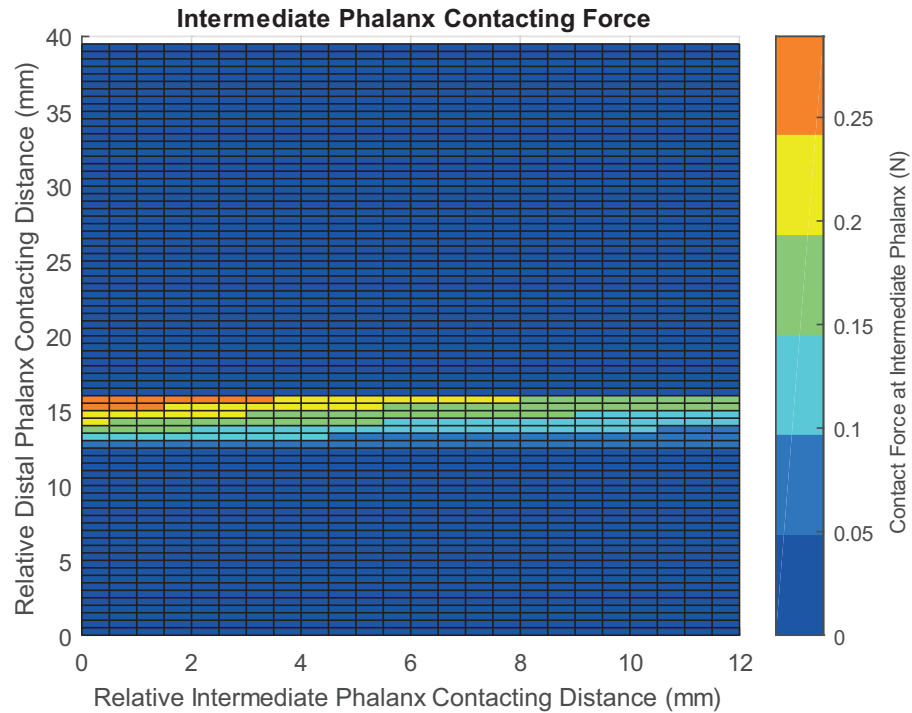


Fig. 3.25. Effects of the contact locations on the contact force produced by the IP when DP is at 48 deg and IP is at 50 deg.

Additionally, it was observed that the configuration of the finger cannot be stable when the object contacts the contact region 2 and 3 of the DP. This is physically reasonable because if the object contacts the contact region 2 and 3, then it is most likely that the object is grasped using the pinch grasp. Since there are changes in the slope of the DP finger pad, it is unlikely to contact both the IP finger pad and the contact region 2 and 3 of the DP finger pad unless the shape of the object enforces that. On the other hand, if the slopes on the DP pad do not exist, the stable region can be further increased. Hence, as the area of the flat surface of the pad increases, the stable region further increases as well.

For this analysis, it was assumed that the object is point contacting the phalanges, the thickness of the finger was neglected, and the compliance of the pad was ignored. However, for the actual system, the contact forces are distributed around the contact locations and the compliance on the finger pad is present. The more pad

is compressed, the higher contact force is exerted onto the object. The effects of the compliance of the pad should be further investigated to increase the accuracy of this analysis. Overall, this contact force analysis was performed to have a general idea of how much contact force the hand can generate and determine the best configuration to be at given an arbitrary tension of the cable.

4. EXPERIMENT

4.1 Preshaping Experiment

The tools to measure the joint angles of the finger are limited. In literature, some potential sensors to measure the joint angles of an underactuated hand are hall-effect sensors with magnets, strain gauges, piezoelectric rubber, or optoelectric sensors [34]. An alternative to those methods is using motion capture. Because it is simple to set up, a planar motion capture experiment was conducted using a cellphone camera to capture the changes in joint angles and processed the images using MATLAB image processing tool. The key objective of this experiment was determining the change in joint angles when there is an increase of the tension of cable and verifying the results of the simulation that control joint angles by varying input force.

4.1.1 Experimental Method

To track each joint of the finger, two 6 mm circular shaped stickers were attached to each link of the finger. To help to detect the stickers, the color of the stickers was chosen such that there was a clear contrast in colors between the finger and the stickers. For this specific experiment, the color of the links was navy and the color of the stickers was pink. The joints and the pads of the finger were painted black to obtain a clear contrast in colors.

Once the tracking markers were set up, the camera was positioned in front of the finger. The camera needed to be directly lined up with the finger. To ensure the camera had been lined up correctly, a horizontal line was drawn on a white background board and the top of the image from the camera was lined up with the horizontal line. To take pictures, a standard cellphone (Samsung Galaxy S7) was utilized and

the cellphone was set up on a cellphone tripod. Figure 4.1 shows the set up of the experiment.

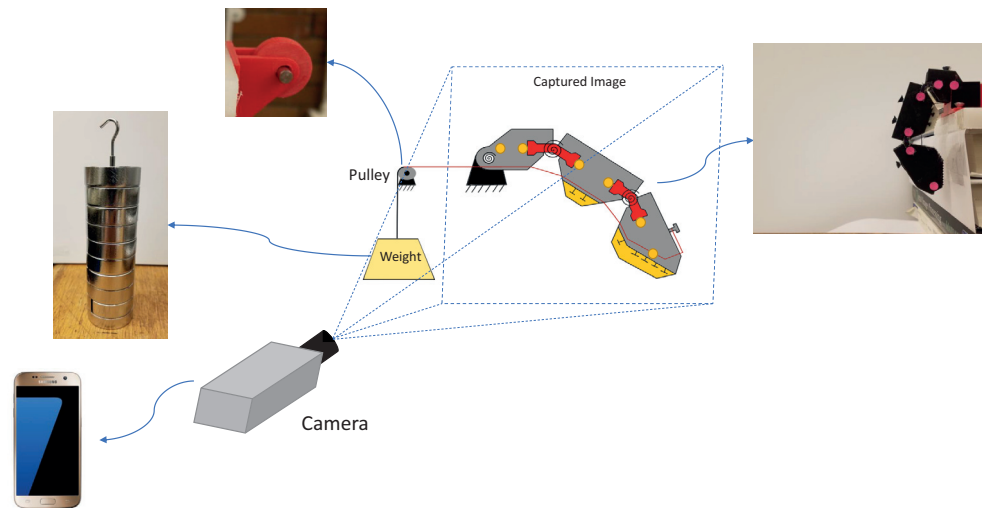


Fig. 4.1. Preshaping experiment setup.

The tension of the actuation cable was generated using weights. Each block of the weights was 100 grams. An additional pulley was used to support the cable and to maintain the direction of the cable steady. The weights were then changed carefully to see the effects of the change in the tension of the cable. Lastly, to determine the joint angles, MATLAB (R2016a) image processing tool was used. The images of the finger were taken and imported into the program to calculate the joint angles.

4.1.2 Results

Using the program, all six tracking markers on the finger were detected. Each of the detected stickers was marked with a red circle around it and a blue line was drawn between the stickers next to each other. as shown in Figure 4.2. Using the



Fig. 4.2. Processed image.

slopes of those lines, the joint angles were computed. Refer to Appendix E for the program algorithm and the derivation of joint angle calculation. In Figure 4.3, one cycle of results is shown. One cycle of results is composed of 42 positions where the weight is added from 0 g to 2000 g and then weights are removed from 2000 g to 0 g. To accurately obtain data, the experiment was conducted by adding weights more carefully. Because if the weights are added to the cable too fast, then it may apply an additional force. Therefore, the weight was added on more slowly and carefully. By taking measurements of one cycle of results, the presence of elastic hysteresis was observed. Because PMC 780 urethane is rubber, it was expected to experience elastic hysteresis.

In Figure 4.4 and Figure 4.5, a black dotted line represents simulation data that neglected the effects of friction, a blue line represents the simulation data that included the friction effects, a red dotted line is the line of average experimental values where the input mass was increased from 0 g to 2000 g, a green dotted line is the average experimental values where the input mass was decreased from 2000 g, and red and green dots are the actual experimental values. On the plot, the input mass is

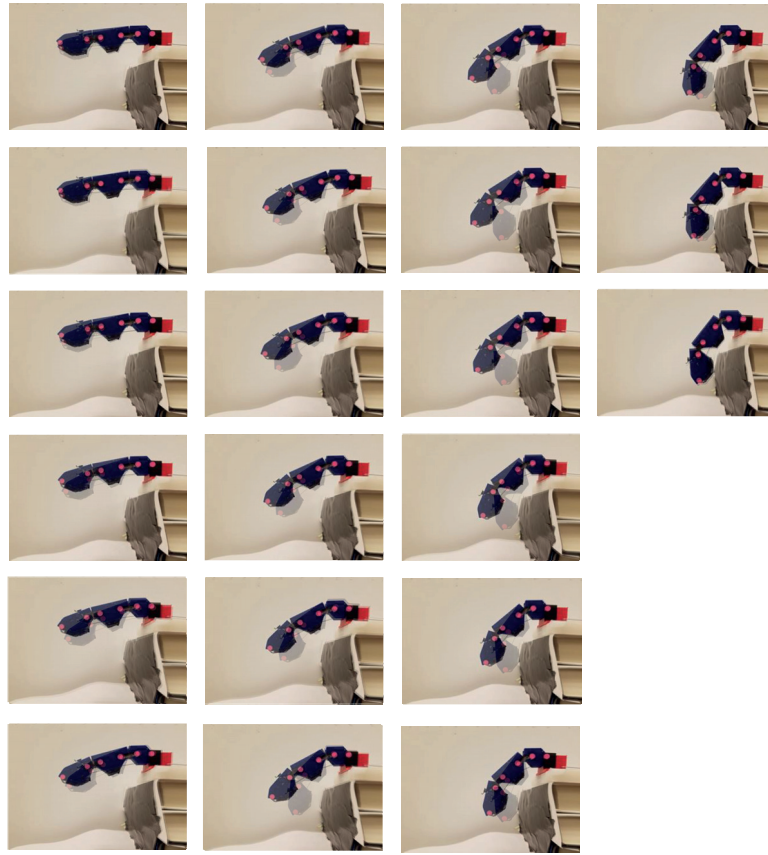
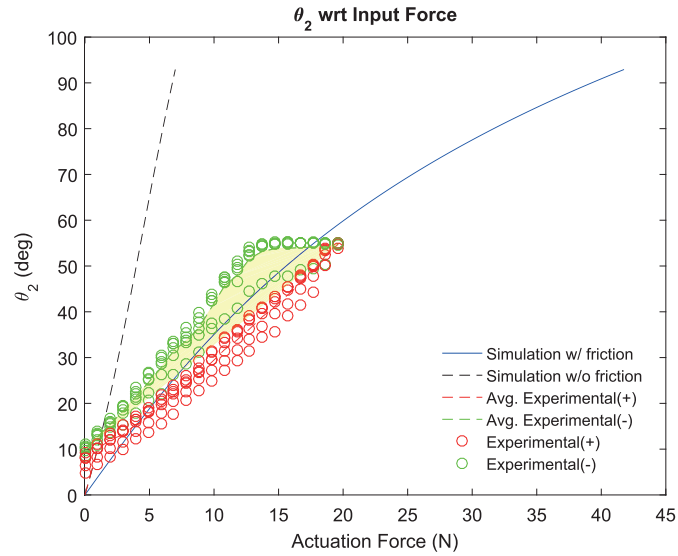
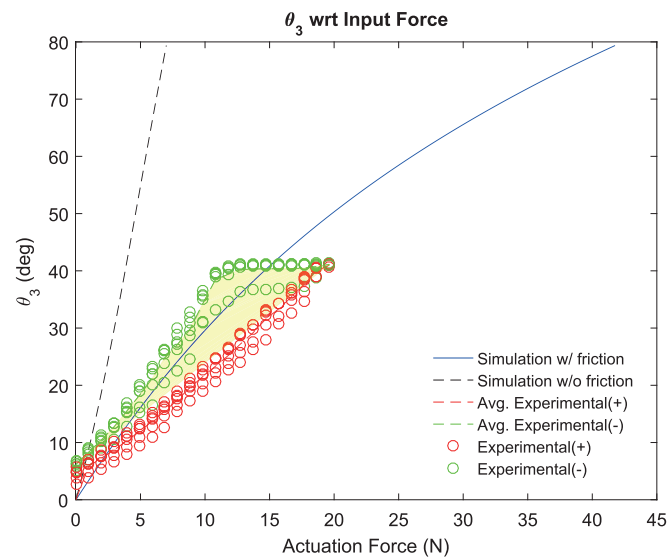


Fig. 4.3. One cycle of results. The weight was added from 0 g to 2000 g and subtracted from 2000 g to 0 g.

converted to weight. Lastly, the yellow area is the area of hysteresis loop. As shown from the plots, θ_2 and θ_3 increase as expected from the simulation and more force needs to be loaded to bend a finger than to unbend it. Such effect can be observed from a viscoelastic material. As expected, polyurethane is a viscoelastic material. A viscoelastic material does not conserve entire energy; rather, it dissipates energy in tension and compression. The area of the hysteresis loop is the amount of energy that cannot be restored. From Figures 4.4 and 4.5, it can be noted that a hysteresis loop is clearly present for each joint.

Fig. 4.4. θ_2 w.r.t. Input force.Fig. 4.5. θ_3 w.r.t. Input force.

4.1.3 Discussion

As shown in Figures 4.4 and 4.5, the joint angles do not correspond even though the input force is the same for the loading and unloading cases. Even at the rest configuration, the joints are not exactly at the original position. To return to the

original configuration of the finger, there is a delay period to return to the initial position. However, such delay does not affect the operating process of this prosthetic hand system since the actuator only rotates in one direction and this system does not require precise motion. However, if the actuator is bi-directional and the system needs to operate in a precise manner, such delay in the system and hysteresis are important factors to consider. Figures 4.3 and 4.6 illustrate a clear hysteresis between loading and unloading case. Additionally, in Figures 4.4 and 4.5, they show that the

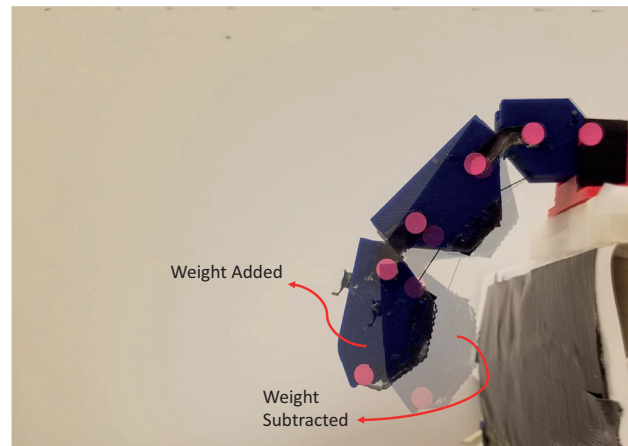


Fig. 4.6. Illustration of the hysteresis when the total input force is 16.7 N.

joint angles from the simulation require less force to move in comparison to the experimental joint angles. As the results clearly illustrate, the effects of friction are not negligible. In fact, as expected from the simulation, the friction force is a huge portion of the input force. Between the experimental and simulation results, additional discrepancies may have been resulted from unaccounted friction from the path of the cable route and other factors such as discrepancies in values between the actual system and the simulated system.

4.2 Grasping Experiment

To verify how well the hand can grasp, the maximum load the hand can handle was tested by adding weights onto a cup. Additionally, to demonstrate that the hand can grasp objects with different shape, size, and weight, different kinds of objects that can be found from daily life were attempted to be grasped.

4.2.1 Verification of the Maximum Load

To determine the maximum load that the hand can lift up, the weights, shown in figure 4.1, were added onto a cup. The weights were added until the hand was not able to hold the cup. Figure 4.7 shows the results of the experiment. From the experiment, it was observed that the cup slowly started to slide down after 400 grams of weights were added to the cup. But the cup was not sliding significantly to notice. However after adding 500 grams of weights, the cup started to slide noticeably. The cup started to slide because the contact force generated by the hand onto the cup was not enough to hold 500 grams of weights. As it can be seen from Figure 4.7, after loading 600 grams of weights, the finger joints twisted, causing the cup to contact the edges of the finger pads.

4.2.2 Grasping Demonstration

To demonstrate the hand can grasp objects from daily life, several objects with different sizes, weights, and shapes were attempted to be grasped. Figure 4.10 shows objects that were attempted to be grasped. Refer to Appendix F for more pictures. From the experiment, objects that are round, within the workspace of the finger, and light, such as the air refresher spray bottle, umbrella, and pencil case can be grasped easily by allowing the finger to wrap around the object. On the other hand, it was possible but difficult to pick up an object such as a pen and a knife that is long but thin relative to the length from the ground. Because the hand has only one finger,

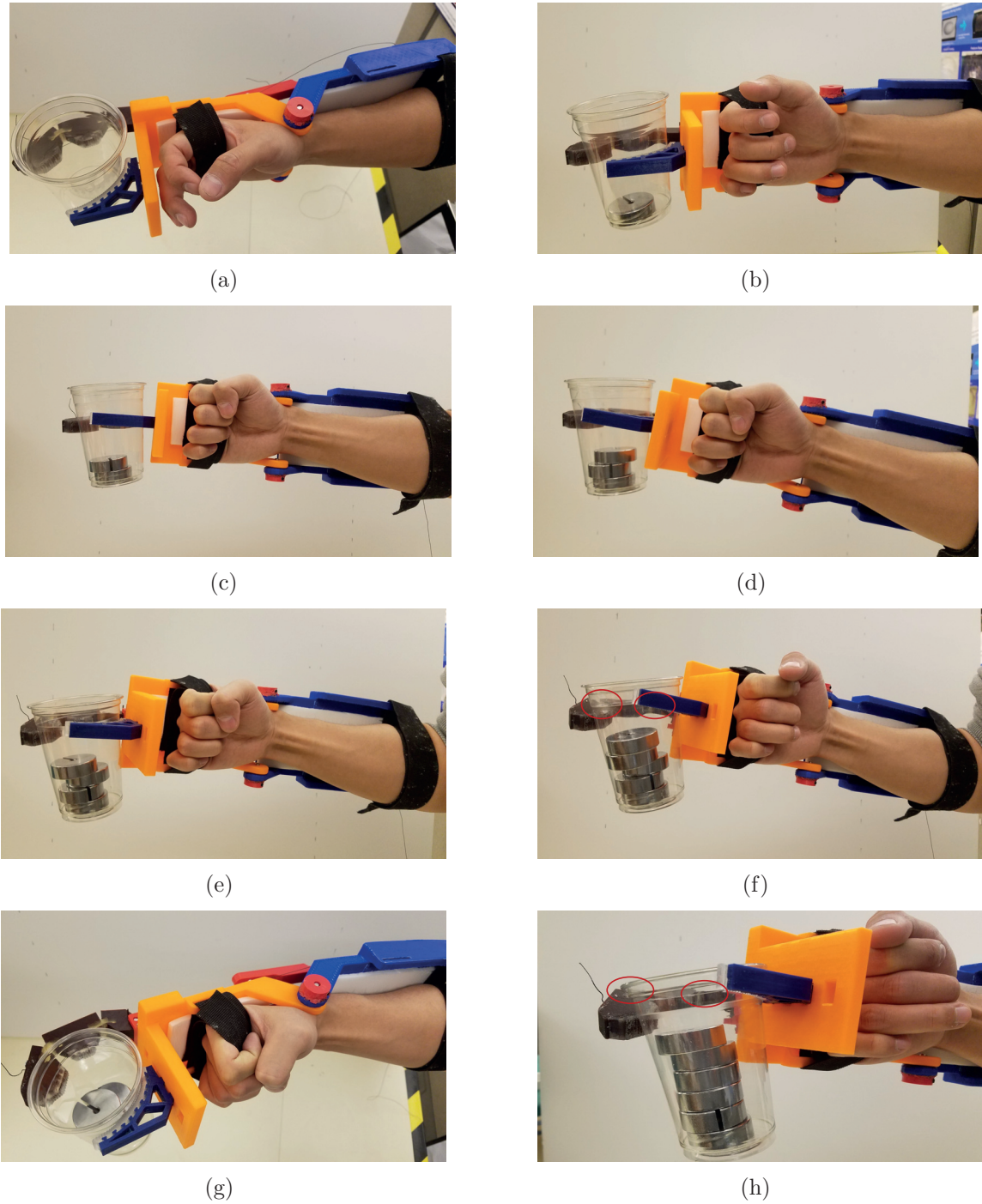


Fig. 4.7. Maximum load verification experiment. (a) 0g. (b) 100g. (c) 200g. (d) 300g. (e) 400g. (f) 500g. (g) 500g top view. (h) 600g.

unless those objects were grasped at their center of mass, they tend to rotate and slip out from the hand. In addition, the objects such as screws, nuts, and coins were difficult to be grasped because they were too close to the ground; the fingers were not able to contact the object.

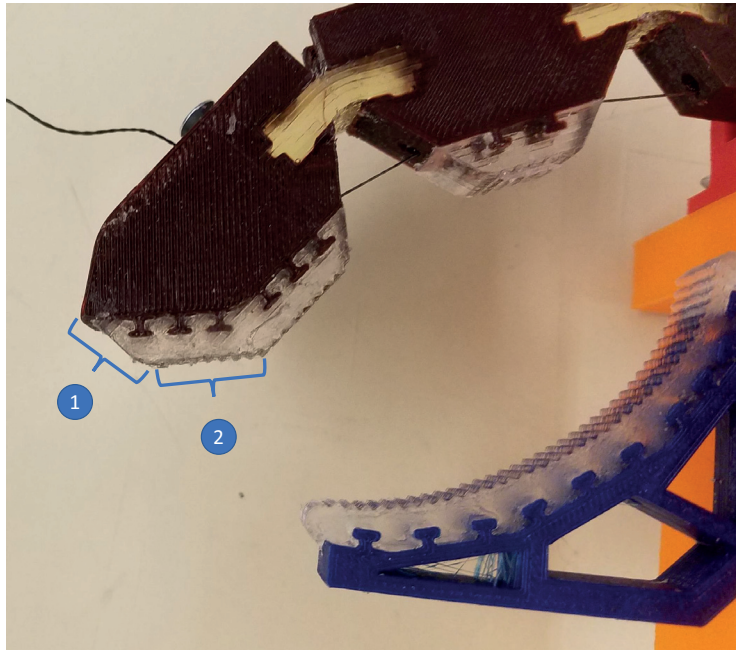


Fig. 4.8. Pinch grasp contact location.

Generally, using pinch grasp, the object needs to be held with a constant magnitude of force once the hand successfully grasps the object. If the user applies more force than it is required to hold, then the object may slip out depending on the initial contact location. Referring to Figure 4.9, the region 1 had a high chance of the object slipping out from the hand if an additional force was applied because the compliant finger tried to slide along the surface the object rather than pushing the object in toward the gauntlet. For example, when the hand tries to grasp a locknut as shown from Figure 4.9(a), most of the time, the finger touches the locknut with the contact region 1. If the compliant finger contacts the object with the region 1, then the compliant finger tends to slide along the surface of the locknut because the contact forces from the compliant finger and supporting finger onto the locknut point toward the

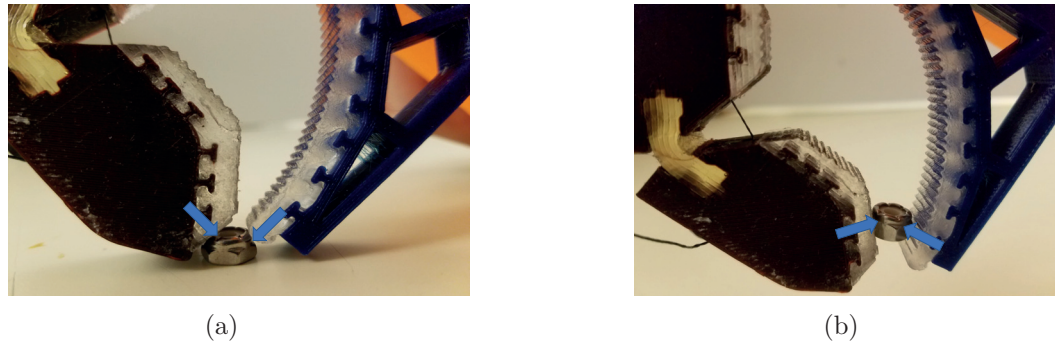
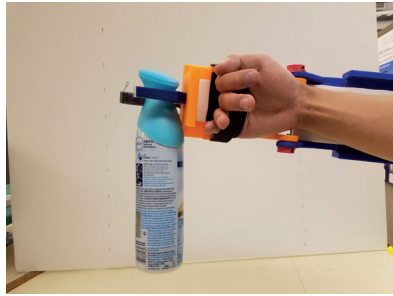


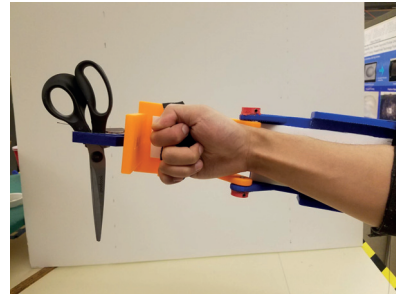
Fig. 4.9. Grasping a locknut using the tip of the finger.(a) Finger contacting at contact region 1.(b) Finger contacting at contact region 2.

ground and the compliant finger bends more as more input force is applied. However, if the finger contacts with the contact region 2, then there is a high chance of locking the object between the compliant finger and the supporting finger. For example, as it can be seen from Figure 4.9(b), the contact forces on the locknut point toward the supporting finger and the compliant finger. This helps to securely grasp the object. However, if an excessive force is applied onto the locknut, then the locknut would slip out from the hand.

To properly use the pinch grasp, the trajectory of the tip of the compliant finger needs to pass right above the tip of the supporting finger. If the level of the supporting finger is changed, then the compliant finger may not pass right above the tip of the supporting finger and the gap between two fingers may be too large to pinch grasp an object.



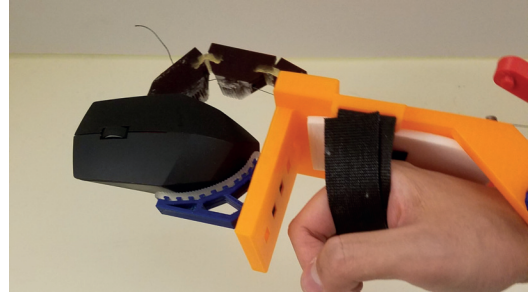
(a)



(b)



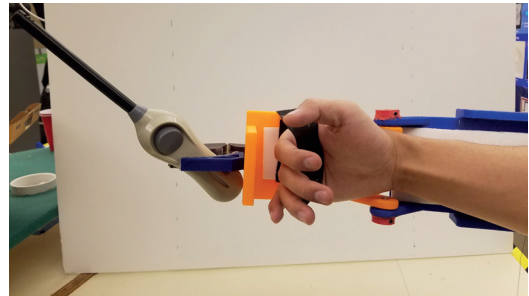
(c)



(d)



(e)



(f)



(g)



(h)

Fig. 4.10. Grasping Experiment. (a) Air refresher spray. (b) Scissors. (c) Pencil case. (d) Computer mouse. (e) Umbrella. (f) Lighter. (g) Knife. (h) Water bottle.

5. CONCLUSIONS

This thesis has presented a new design of a body-powered prosthetic hand. Based on the existing 3-D printed prosthetic hand from Enabling the Future, the actuation strategy of the hand had been redesigned. Using a novel ratcheting mechanism with a partial gear, the cable that changes the position of the compliant finger is controlled. By rotating the actuator, the rack attached to the actuator is moved to pull the cable that controls the joint angles of the finger. Using this mechanism with the cantilever bar structures attached to the forearm, the user does not need to maintain an awkward hand position to grasp an object since the mechanism holds the finger at a specific position based on the rotation of the ratchet. Unlike the previously developed 3-D printed prosthetic hands, with this mechanism the user can avoid awkward hand positions to hold objects and prevent from accidentally opening the finger by extending their wrist. Additionally, the work showed that the compliant finger effectively ejects the external disturbances that could damage the system.

Additionally, in this work, the preshaping motion of the underactuated hand and the contact force analysis had been conducted. In the literature, the effects of friction have often been ignored. However, friction is one of the most critical variable for the cable driven underactuated hands as proven from this work. Considering the effects of the friction, the force required to hold the finger in place was analyzed by controlling the tension of the cable. The behavior of the finger from that analysis was compared with the preshaping experiment. In addition, by varying the angle of the actuator, the change in the position of the finger and the tension of the cable to hold that position on the actual system were estimated. It was found that the effects of friction add up as the finger curves more and hysteresis of the flexure joints was clearly observed from the experiment. To estimate the magnitude of contact force the hand can generate, the contact force analysis was performed. This allows one

to estimate how much load this hand can handle and learn about the effects of the contact locations and joint angles on the contact force overall. Lastly, by grasping various types of objects, it was shown that the maximum load the hand can hold is around 500 grams and it has a higher chance of grasping objects that are cylindrical and circular.

6. RECOMMENDATIONS

For this project, there are additional design improvements that can be made. To start with, the effects of friction increase the required force to bend the joints. To reduce the friction effects, a linkage based finger with springs can be designed to substitute the compliant finger. By preventing the tendon cable from touching the surface of the phalanges, the effects of friction can be reduced. Even though a linkage based finger has friction between links, the effects of friction would be less than that of the cable driven finger.

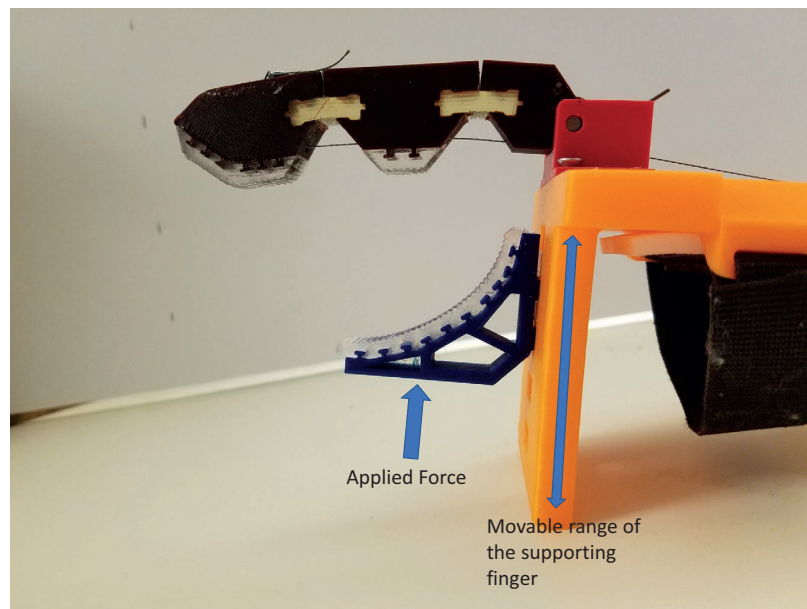


Fig. 6.1. The recommended design allows the support finger to move when force is applied.

From the prototype of the hand, it was noted that the range of size of an object that can be grasped is limited based on where the rigidly supporting finger is placed. Depending on which level it is placed at, the hand can grasp something relatively big

or small. However, the current design requires the user to pull out the supporting finger manually and put it on a different level. This can be very cumbersome for the users. In addition, the user will fatigue their wrist if they constantly bend their wrist to actuate the hand. An alternative design would be an environment interactive supporting finger. Instead of this finger being rigidly attached to the hand until the user pulls it out and pushes back it into a different level, they will use their surrounding environment or their other hand to control the position of the supporting finger. The location of this finger will be simply changed by pushing it against something like a table or pushing it using the other hand to make sure it is contacting the object. Figure 6.1 illustrates how the support finger moves.

Lastly, a program that computes the parameters of a prosthetic hand based on the size of the user's hand and the level of amputation would help to deliver a customized prosthetic hand to the users in a shorter period of time. Furthermore, this program would compute the best locations to grasp given the size and the shape of an object using the contact force analysis. By computing the best locations to grasp based on the given objects, this would reduce the job of the users. Without the program, the users need to find out the best locations to grasp by trial and error.

REFERENCES

- [1] F. Cordella, A. L. Ciancio, R. Sacchetti, A. Davalli, A. G. Cutti, E. Guglielmelli, and L. Zollo, “Literature review on needs of upper limb prosthesis users,” vol. 10, no. MAY, 2016.
- [2] Bebionic, “The Hand.” [Online]. Available: <http://bebionic.com/the{-}hand/>
- [3] V. Systems, “Vincent Evolution 3.” [Online]. Available: <https://vincentsystems.de/en/prosthetics/vincent-evolution-3/>
- [4] Touch Bionics, “i-limb Ultra.” [Online]. Available: <http://www.touchbionics.com/>
- [5] J. T. Belter, J. L. Segil, A. M. Dollar, and R. F. Weir, “Mechanical design and performance specifications of anthropomorphic prosthetic hands: A review,” *The Journal of Rehabilitation Research and Development*, vol. 50, no. 5, p. 599, 2013. [Online]. Available: <http://www.rehab.research.va.gov/jour/2013/505/pdf/belter505.pdf>
- [6] T. W. Williams III, “Progress on stabilizing and controlling powered upper-limb prostheses,” *The Journal of Rehabilitation Research and Development*, vol. 48, no. 6, p. ix, 2011. [Online]. Available: <http://www.rehab.research.va.gov/jour/11/486/pdf/williams486.pdf>
- [7] Medical Expo, “Body-powered hand prosthesis/hook clamp/adult.” [Online]. Available: <http://www.medicalexpo.com/prod/rslsteeper/product-74956-458468.html>
- [8] J. T. Belter, B. C. Reynolds, and A. M. Dollar, “Grasp and force based taxonomy of split-hook prosthetic terminal devices,” in *2014 36th Annual International Conference of the IEEE Engineering in Medicine and Biology Society, EMBC 2014*, 2014, pp. 6613–6618.
- [9] Enabling the Future, “The Raptor Reloaded.” [Online]. Available: enablingthefuture.org/upper-limb-prosthetics/raptor-reloaded/
- [10] R. Tedrake, *Underactuated Robotics: Learning, Planning, and Control of Efficient and Agile Machines*, 2009.
- [11] A. M. Dollar and R. D. Howe, “The SDM hand as a prosthetic terminal device: A feasibility study,” in *2007 IEEE 10th International Conference on Rehabilitation Robotics, ICORR’07*, 2007, pp. 978–983.
- [12] H. Stuart, S. Wang, O. Khatib, and M. R. Cutkosky, “The Ocean One hands: An adaptive design for robust marine manipulation,” *International Journal of Robotics Research*, vol. 36, no. 2, pp. 150–166, 2017.

- [13] J. P. Mayo, “Morphological Design Methodology of Rugged Underactuated Gripper,” Ph.D. dissertation, Massachusetts Institute of Technology, 2016.
- [14] L. U. Odhner, L. P. Jentoft, M. R. Claffee, N. Corson, Y. Tenzer, R. R. Ma, M. Buehler, R. Kohout, R. D. Howe, and A. M. Dollar, “A compliant, underactuated hand for robust manipulation,” *International Journal of Robotics Research*, vol. 33, no. 5, pp. 736–752, 2014.
- [15] J. Gafford, Y. Ding, A. Harris, T. McKenna, P. Polygerinos, D. Holland, C. Walsh, and A. Moser, “Shape Deposition Manufacturing of a Soft, Atraumatic, and Deployable Surgical Grasper,” *Journal of Mechanisms and Robotics*, vol. 7, no. 2, p. 021006, 2015. [Online]. Available: <http://mechanismsrobotics.asmedigitalcollection.asme.org/article.aspx?doi=10.1115/1.4029493>
- [16] T. Laliberté, L. Birglen, and M. C. Gosselin, “Underactuation in robotic grasping hands,” *Machine Intelligence & Robotic Control*, vol. 4, no. 3, pp. 1–11, 2003.
- [17] A. M. Dollar and R. D. Howe, “The highly adaptive SDM hand: Design and performance evaluation,” in *International Journal of Robotics Research*, vol. 29, no. 5, 2010, pp. 585–597.
- [18] —, “A robust compliant grasper via shape deposition manufacturing,” *IEEE/ASME Transactions on Mechatronics*, vol. 11, no. 2, pp. 154–161, 2006.
- [19] M. R. Cutkosky, “On Grasp Choice, Grasp Models, and the Design of Hands for Manufacturing Tasks,” *IEEE Transactions on Robotics and Automation*, vol. 5, no. 3, pp. 269–279, 1989.
- [20] E. Biddiss, D. Beaton, and T. Chau, “Consumer design priorities for upper limb prosthetics,” *Disability and Rehabilitation: Assistive Technology*, vol. 2, no. 6, pp. 346–357, 2007.
- [21] J. T. Belter and A. M. Dollar, “Performance characteristics of anthropomorphic prosthetic hands,” in *IEEE International Conference on Rehabilitation Robotics*, 2011.
- [22] J. ten Kate, G. Smit, and P. Breedveld, “3D-printed upper limb prostheses: a review,” vol. 12, no. 3, pp. 300–314, 2017.
- [23] G. Smit, R. M. Bongers, C. K. Van der Sluis, and D. H. Plettenburg, “Efficiency of voluntary opening hand and hook prosthetic devices: 24 years of development,” *The Journal of Rehabilitation Research and Development*, vol. 49, no. 4, p. 523, 2012. [Online]. Available: <http://www.rehab.research.va.gov/jour/2012/494/pdf/smit494.pdf>
- [24] J. Ryu, W. P. Cooney, L. J. Askew, K. N. An, and E. Y. Chao, “Functional ranges of motion of the wrist joint,” *Journal of Hand Surgery*, vol. 16, no. 3, pp. 409–419, 1991.
- [25] J. T. Belter and A. M. Dollar, “Novel differential mechanism enabling two DOF from a single actuator: Application to a prosthetic hand,” in *IEEE International Conference on Rehabilitation Robotics*, 2013.
- [26] A. M. Dollar and R. D. Howe, “Joint coupling design of underactuated hands for unstructured environments,” *International Journal of Robotics Research*, vol. 30, no. 9, pp. 1157–1169, 2011.

- [27] R. R. Ma, J. T. Belter, and A. M. Dollar, “Hybrid Deposition Manufacturing: Design Strategies for Multimaterial Mechanisms Via Three-Dimensional Printing and Material Deposition,” *Journal of Mechanisms and Robotics*, vol. 7, no. 2, p. 021002, 2015. [Online]. Available: <http://mechanismsrobotics.asmedigitalcollection.asme.org/article.aspx?doi=10.1115/1.4029400>
- [28] L. L. Howell, “A Generalized Loop-Closure Theory for the Analysis and Synthesis of compliant mechanisms,” Ph.D. dissertation, 1993.
- [29] L. L. Howell and A. Midha, “A Generalized Loop-Closure Theory for The Analysis and Synthesis of Compliant Mechanisms,” in *American Society of Mechanical Engineers, Design Engineering Division (Publication) DE*, vol. 71, 1994, pp. 491–500.
- [30] L. L. Howell, S. P. Magleby, and B. M. Olsen, *Handbook of Compliant Mechanisms*, 2013.
- [31] L. L. Howell and A. Midha, “A Method for the Design of Compliant Mechanisms With Small-Length Flexural Pivots,” *Journal of Mechanical Design*, vol. 116, no. 1, p. 280, 1994.
- [32] G. Salvietti, I. Hussain, M. Malvezzi, and D. Prattichizzo, “Design of the Passive Joints of Underactuated Modular Soft Hands for Fingertip Trajectory Tracking,” *IEEE Robotics and Automation Letters*, vol. 2, no. 4, pp. 2008–2015, 2017. [Online]. Available: <http://ieeexplore.ieee.org/document/7954638/>
- [33] V. A. Lubarda, “The mechanics of belt friction revisited,” *International Journal of Mechanical Engineering Education*, vol. 42, 2014.
- [34] L. P. Jentoft, A. M. Dollar, C. R. Wagner, and R. D. Howe, “Intrinsic embedded sensors for polymeric mechatronics: Flexure and force sensing,” *Sensors (Switzerland)*, vol. 14, no. 3, pp. 3861–3870, 2014.
- [35] D. M. Aukes, B. Heyneman, J. Ulmen, H. Stuart, M. R. Cutkosky, S. Kim, P. Garcia, and A. Edsinger, “Design and testing of a selectively compliant underactuated hand,” *International Journal of Robotics Research*, vol. 33, no. 5, pp. 721–735, 2014.
- [36] D. Aukes, S. Kim, P. Garcia, A. Edsinger, and M. R. Cutkosky, “Selectively compliant underactuated hand for mobile manipulation,” in *Proceedings - IEEE International Conference on Robotics and Automation*, 2012, pp. 2824–2829.
- [37] M. Baril, T. Laliberté, C. Gosselin, and F. Routhier, “On the Design of Mechanically Programmable Underactuated Anthropomorphic Robotic and Prosthetic Grippers,” in *Volume 4: 36th Mechanisms and Robotics Conference, Parts A and B*, 2012, p. 85. [Online]. Available: <http://proceedings.asmedigitalcollection.asme.org/proceeding.aspx?doi=10.1115/DETC2012-70705>
- [38] M. Baril, T. Laliberte, F. Guay, and C. Gosselin, “Static Analysis of Single-Input/Multiple-Output Tendon-Driven Underactuated Mechanisms for Robotic Hands,” in *Volume 2: 34th Annual Mechanisms and Robotics Conference, Parts A and B*, 2010, pp. 155–164. [Online]. Available: <http://proceedings.asmedigitalcollection.asme.org/proceeding.aspx?articleid=1611169>

- [39] B. Belzile and L. Birglen, “Optimal Design of Self-Adaptive Fingers for Proprioceptive Tactile Sensing,” *Journal of Mechanisms and Robotics*, vol. 9, no. 5, p. 051004, 2017. [Online]. Available: <http://mechanismsrobotics.asmedigitalcollection.asme.org/article.aspx?doi=10.1115/1.4037113>
- [40] E. Biddiss and T. Chau, “Upper limb prosthesis use and abandonment: A survey of the last 25 years,” pp. 236–257, 2007.
- [41] Biomimetic Robotics Lab, “The MIT HERMES humanoid robot system.” [Online]. Available: <http://biomimetics.mit.edu/>
- [42] W. G. Bircher, A. M. Dollar, and N. Rojas, “A two-fingered robot gripper with large object reorientation range,” in *Proceedings - IEEE International Conference on Robotics and Automation*, 2017, pp. 3453–3460.
- [43] M. D. Bland, J. A. Beebe, D. D. Hardwick, and C. E. Lang, “Restricted Active Range of Motion at the Elbow, Forearm, Wrist, or Fingers Decreases Hand Function,” *Journal of Hand Therapy*, vol. 21, no. 3, pp. 268–275, 2008.
- [44] J. Borràs and A. M. Dollar, “Actuation Torque Reduction in Parallel Robots Using Joint Compliance,” *Journal of Mechanisms and Robotics*, vol. 6, no. 2, p. 021006, 2014. [Online]. Available: <http://mechanismsrobotics.asmedigitalcollection.asme.org/article.aspx?doi=10.1115/1.4026628>
- [45] J.-M. Boucher and L. Birglen, “Performance Augmentation of Under-actuated Fingers’ Grasps Using Multiple Drive Actuation,” *Journal of Mechanisms and Robotics*, vol. 9, no. 4, p. 041003, 2017. [Online]. Available: <http://mechanismsrobotics.asmedigitalcollection.asme.org/article.aspx?doi=10.1115/1.4036220>
- [46] S. L. Carey, D. J. Lura, and M. J. Highsmith, “Differences in myoelectric and body-powered upper-limb prostheses: Systematic literature review,” *Journal of Rehabilitation Research and Development*, 2015.
- [47] S. L. Carey, R. V. Dubey, G. S. Bauer, and M. J. Highsmith, “Kinematic comparison of myoelectric and body powered prostheses while performing common activities,” *Prosthetics and Orthotics International*, vol. 33, no. 2, pp. 179–186, 2009.
- [48] C. Dally, D. Johnson, M. Canon, S. Ritter, and K. Mehta, “Characteristics of a 3D-printed prosthetic hand for use in developing countries,” in *Proceedings of the 5th IEEE Global Humanitarian Technology Conference, GHTC 2015*, 2015, pp. 66–70.
- [49] A. Dollar and R. Howe, “Joint coupling design of underactuated grippers,” in *30th Annual ASME Mechanisms and Robotics Conference, 2006 International Design Engineering Technical Conferences (IDETC)*, vol. 2, 2006, pp. 903–911. [Online]. Available: <http://proceedings.asmedigitalcollection.asme.org/proceeding.aspx?articleid=1595047>
- [50] M. Goldfarb and J. E. Speich, “A Well-Behaved Revolute Flexure Joint for Compliant Mechanism Design,” *Journal of Mechanical Design*, vol. 121, no. 3, p. 424, 1999. [Online]. Available: <http://mechanicaldesign.asmedigitalcollection.asme.org/article.aspx?articleid=1445671>

- [51] F. Guay and C. Gosselin, "Static model for a 3-DOF underactuated finger," *Mechanical Sciences*, vol. 2, no. 1, pp. 65–71, 2011. [Online]. Available: <http://www.mech-sci.net/2/65/2011/>
- [52] J. Guo and K. M. Lee, "Compliant joint design and flexure finger dynamic analysis using an equivalent pin model," *Mechanism and Machine Theory*, vol. 70, pp. 338–353, 2013.
- [53] G. A. Kragten, M. Baril, C. Gosselin, and J. L. Herder, "Stable precision grasps by underactuated grippers," *IEEE Transactions on Robotics*, vol. 27, no. 6, pp. 1056–1066, 2011.
- [54] T. Laliberté, M. Baril, F. Guay, and C. Gosselin, "Towards the design of a prosthetic underactuated hand," *Mechanical Sciences*, vol. 1, no. 1, pp. 19–26, 2010. [Online]. Available: <http://www.mech-sci.net/1/19/2010/>
- [55] M. V. Liarokapis and A. M. Dollar, "Post-Contact, In-Hand Object Motion Compensation With Adaptive Hands," 2016.
- [56] R. R. Ma, W. G. Bircher, and A. M. Dollar, "Toward robust, whole-hand caging manipulation with underactuated hands," in *Proceedings - IEEE International Conference on Robotics and Automation*, 2017, pp. 1336–1342.
- [57] R. R. Ma and A. M. Dollar, "Linkage-Based Analysis and Optimization of an Underactuated Planar Manipulator for In-Hand Manipulation," *Journal of Mechanisms and Robotics*, vol. 6, no. 1, p. 011002, 2013.
- [58] R. R. Ma, A. Spiers, and A. M. Dollar, "M2 gripper: Extending the dexterity of a simple, Underactuated gripper," in *Mechanisms and Machine Science*, 2016, vol. 36, pp. 795–805.
- [59] R. R. Ma, L. U. Odhner, and A. M. Dollar, "A modular, open-source 3D printed underactuated hand," in *Proceedings - IEEE International Conference on Robotics and Automation*, 2013, pp. 2737–2743.
- [60] S. Montambault and C. M. Gosselin, "Analysis of Underactuated Mechanical Grippers," *Journal of Mechanical Design*, vol. 123, no. 3, p. 367, 2001. [Online]. Available: <http://mechanicaldesign.asmedigitalcollection.asme.org/article.aspx?articleid=1446481>
- [61] L. U. Odhner and A. M. Dollar, "Dexterous manipulation with underactuated elastic hands," in *Proceedings - IEEE International Conference on Robotics and Automation*, 2011, pp. 5254–5260.
- [62] R. Pape, "The Effect of Joint Locks in Underactuated Hand Prostheses," Ph.D. dissertation, Delft University of Technology, 2011.
- [63] M. Polisiero, P. Bifulco, A. Liccardo, M. Cesarelli, M. Romano, G. D. Gargiulo, A. L. McEwan, and M. D'Apuzzo, "Design and assessment of a low-cost, electromyographically controlled, prosthetic hand," *Medical Devices: Evidence and Research*, vol. 6, no. 1, pp. 97–104, 2013.
- [64] S. A. J. Spanjer, R. Balasubramanian, J. L. Herder, and A. M. Dollar, "Improved grasp robustness through variable transmission ratios in underactuated fingers," in *IEEE International Conference on Intelligent Robots and Systems*, 2012, pp. 2289–2294.

- [65] H. S. Stuart, S. Wang, B. Gardineer, D. L. Christensen, D. M. Aukes, and M. Cutkosky, "A compliant underactuated hand with suction flow for underwater mobile manipulation," in *Proceedings - IEEE International Conference on Robotics and Automation*, 2014, pp. 6691–6697.
- [66] J. Zuniga, D. Katsavelis, J. Peck, J. Stollberg, M. Petrykowski, A. Carson, and C. Fernandez, "Cyborg beast: A low-cost 3d-printed prosthetic hand for children with upper-limb differences," *BMC Research Notes*, vol. 8, no. 1, 2015.
- [67] R. Balasubramanian, J. T. Belter, and A. M. Dollar, "External Disturbances and Coupling Mechanisms in Underactuated Hands," in *Volume 2: 34th Annual Mechanisms and Robotics Conference, Parts A and B*, 2010.

A. JOINT ANGLE CALCULATION DERIVATION

To solve multiple equations simultaneously, Newton Raphson method is used. Newton Raphson is a numerical method that looks for the roots of a real valued function by continuously approximating the roots of the function based on the previous approximation the value of the roots is within the desired tolerance.

A.1 Force Controlled

This method calculates the joint angles by changing the magnitude of input force. Initially, it is assumed that friction is not present along the path of cable. Therefore, the input force is changed without considering the effects of friction.

$$f_1 : C = r_a \theta_a = \sum_{i=2}^3 (L_i - 2(L_i/2) \cos(\theta_i/2) + 2b_i \sin(\theta_i/2)) \quad (\text{A.1})$$

Figure A.1 shows the free body diagram of the intermediate phalanx. By summing a moment about the center of rotation, Equation A.2 can be derived. a_2 and b_2 are the moment arm between the input force and the center of the joint.

$$f_2 : (a_2 \hat{i}_2 + b_2 \hat{j}_2) \times (F_a(\cos(\frac{\theta_2}{2} + \pi)) \hat{i}_2 + F_a(\sin(\frac{\theta_2}{2} + \pi)) \hat{j}_2) + k_2(\theta_2 - \theta_{2int}) = 0 \quad (\text{A.2})$$

Equation A.2 can be expanded as shown below.

$$a_2 F_a(\sin(\frac{\theta_2}{2} + \pi) - b_2 F_a(\cos(\frac{\theta_2}{2} + \pi) + k_2(\theta_2 - \theta_{2int})) = 0 \quad (\text{A.3})$$

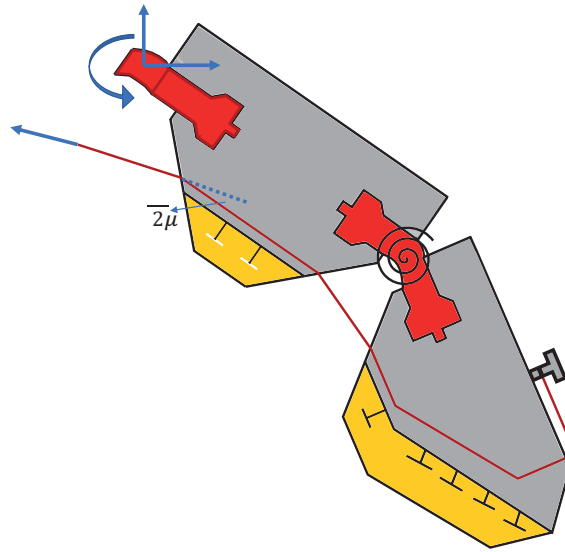


Fig. A.1. FBD of distal and intermediate phalanx during preshaping.

Figure A.2 shows the free body diagram of the distal phalanx. Similarly, by summing moment about the center of rotation, equation can be derived where a_3 and b_3 are the moment arm between the input force and the center of the joint.

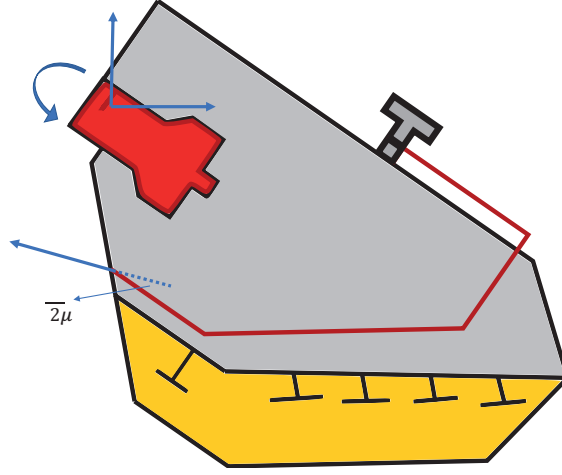


Fig. A.2. FBD of distal phalanx during preshaping.

$$f_3 : (a_3 \hat{i}_3 + b_3 \hat{j}_3) \times (F_a (\cos(\frac{\theta_3}{2} + \pi)) \hat{i}_3 + F_a (\sin(\frac{\theta_3}{2} + \pi)) \hat{j}_3) + k_3 (\theta_3 - \theta_{3int}) = 0 \quad (\text{A.4})$$

Equation A.4 is expanded as Equation A.5

$$a_3 F_a (\sin(-\frac{\theta_3}{2} + \pi) - b_3 F_a (\cos(\frac{\theta_3}{2} + \pi) + k_3 (\theta_3 - \theta_{3int})) = 0 \quad (\text{A.5})$$

To solve Equation A.1, A.3, and A.5 simultaneously, Newton Raphson method has to be used. To obtain roots of θ_2 , θ_3 , and θ_a , partial derivatives of Equations A.1, A.3, and A.5 with respect to θ_2 , θ_3 , and θ_a need to be taken.

$$\frac{\partial f_1}{\partial \theta_2} = L_2/2 \sin(\theta_2/2) + b_2 \cos(\theta_2/2) \quad (\text{A.6})$$

$$\frac{\partial f_1}{\partial \theta_3} = L_3/2 \sin(\theta_3/2) + b_3 \cos(\theta_3/2) \quad (\text{A.7})$$

$$\frac{\partial f_1}{\partial \theta_a} = -r_a \quad (\text{A.8})$$

$$\frac{\partial f_2}{\partial \theta_2} = a_2 F_a \cos(\frac{\theta_2}{2} + \pi)/2 + b_2 F_a \sin(\frac{\theta_2}{2} + \pi)/2 + k_2 = 0 \quad (\text{A.9})$$

$$\frac{\partial f_2}{\partial \theta_3} = 0 \quad (\text{A.10})$$

$$\frac{\partial f_2}{\partial \theta_a} = 0 \quad (\text{A.11})$$

$$\frac{\partial f_3}{\partial \theta_2} = 0 \quad (\text{A.12})$$

$$\frac{\partial f_3}{\partial \theta_3} = a_3 F_a \cos\left(\frac{\theta_3}{2} + \pi\right)/2 + b_3 F_a \sin\left(\frac{\theta_3}{2} + \pi\right)/2 + k_3 = 0 \quad (\text{A.13})$$

$$\frac{\partial f_3}{\partial \theta_a} = 0 \quad (\text{A.14})$$

Until $\Delta\theta_2$, $\Delta\theta_3$, $\Delta\theta_a$ converges to zero, θ_2 , θ_3 , and θ_a need to be updated and solved iteratively using Equation A.16.

$$\begin{bmatrix} \Delta f_1 \\ \Delta f_2 \\ \Delta f_3 \end{bmatrix} = \begin{bmatrix} \frac{\partial f_1}{\partial \theta_2} & \frac{\partial f_1}{\partial \theta_3} & \frac{\partial f_1}{\partial \theta_a} \\ \frac{\partial f_2}{\partial \theta_2} & \frac{\partial f_2}{\partial \theta_3} & \frac{\partial f_2}{\partial \theta_a} \\ \frac{\partial f_3}{\partial \theta_2} & \frac{\partial f_3}{\partial \theta_3} & \frac{\partial f_3}{\partial \theta_a} \end{bmatrix} \begin{bmatrix} \Delta\theta_2 \\ \Delta\theta_3 \\ \Delta\theta_a \end{bmatrix} \quad (\text{A.15})$$

$$\begin{bmatrix} \theta_{2new} \\ \theta_{3new} \\ \theta_{anew} \end{bmatrix} = \begin{bmatrix} \theta_{2past} \\ \theta_{3past} \\ \theta_{apast} \end{bmatrix} - \begin{bmatrix} \frac{\partial f_1}{\partial \theta_2} & \frac{\partial f_1}{\partial \theta_3} & \frac{\partial f_1}{\partial \theta_a} \\ \frac{\partial f_2}{\partial \theta_2} & \frac{\partial f_2}{\partial \theta_3} & \frac{\partial f_2}{\partial \theta_a} \\ \frac{\partial f_3}{\partial \theta_2} & \frac{\partial f_3}{\partial \theta_3} & \frac{\partial f_3}{\partial \theta_a} \end{bmatrix}^{-1} \begin{bmatrix} f_1 \\ f_2 \\ f_3 \end{bmatrix} \quad (\text{A.16})$$

A.2 Rack Distance Controlled

To simulate how the joint angles change on the actual system, the angle of actuator needs to be varied. Therefore, for this method, θ_a is varied.

$$f_1 : C = r_a \theta_a = \sum_{i=2}^3 L_i - 2(L_i/2) \cos(\theta_i/2) + 2b_i \sin(\theta_i/2) \quad (\text{A.17})$$

For this method, Equation A.3 and A.5 are combined as one equation.

$$\begin{aligned} & (a_2(\sin(\frac{\theta_2}{2} + \pi) - b_2(\cos(\frac{\theta_2}{2} + \pi)))k_3(\theta_3 - \theta_{3int}) \\ & - (a_3(\sin(\frac{\theta_3}{2} + \pi) - b_3(\cos(\frac{\theta_3}{2} + \pi)))k_2(\theta_2 - \theta_{2int}) = 0 \end{aligned} \quad (\text{A.18})$$

To solve Equation A.17 and A.18 simultaneously, Newton Raphson method is used again. For this method, roots of θ_2 , θ_3 need to be obtained. To start, partial derivatives of Equation A.17 and A.18 with respect to θ_2 , θ_3 need to be taken.

$$\frac{\partial f_1}{\partial \theta_2} = L_2/2 \sin(\theta_2/2) + b_2/2 \cos(\theta_2/2) \quad (\text{A.19})$$

$$\frac{\partial f_1}{\partial \theta_3} = L_3/2 \sin(\theta_3/2) + b_3/2 \cos(\theta_3/2) \quad (\text{A.20})$$

$$\begin{aligned} \frac{\partial f_2}{\partial \theta_2} = & \left(\frac{a_2}{2} (\cos(\frac{\theta_2}{2} + \pi)) + \frac{b_2}{2} (\sin(\frac{\theta_2}{2} + \pi)) k_3(\theta_3 - \theta_{3int}) - \right. \\ & \left. (a_3 \sin(\frac{\theta_3}{2} + \pi) - b_3 \cos(\frac{\theta_3}{2} + \pi)) k_2 = 0 \right. \end{aligned} \quad (\text{A.21})$$

$$\begin{aligned} \frac{\partial f_2}{\partial \theta_3} = & - \left(\frac{a_3}{2} (\cos(\frac{\theta_3}{2} + \pi)) + \frac{b_3}{2} (\sin(\frac{\theta_3}{2} + \pi)) k_2(\theta_2 - \theta_{2int}) + \right. \\ & \left. (a_2 \sin(\frac{\theta_2}{2} + \pi) - b_2 \cos(\frac{\theta_2}{2} + \pi)) k_3 = 0 \right. \end{aligned} \quad (\text{A.22})$$

Until $\Delta\theta_2$ and $\Delta\theta_3$ converges to zero, θ_2 and θ_3 need to be updated and solved iteratively using Equation A.24.

$$\begin{bmatrix} \Delta f_1 \\ \Delta f_2 \end{bmatrix} = \begin{bmatrix} \frac{\partial f_1}{\partial \theta_2} & \frac{\partial f_1}{\partial \theta_3} \\ \frac{\partial f_2}{\partial \theta_2} & \frac{\partial f_2}{\partial \theta_3} \end{bmatrix} \begin{bmatrix} \Delta\theta_2 \\ \Delta\theta_3 \end{bmatrix} \quad (\text{A.23})$$

$$\begin{bmatrix} \theta_{2new} \\ \theta_{3new} \end{bmatrix} = \begin{bmatrix} \theta_{2past} \\ \theta_{3past} \end{bmatrix} - \begin{bmatrix} \frac{\partial f_1}{\partial \theta_2} & \frac{\partial f_1}{\partial \theta_3} \\ \frac{\partial f_2}{\partial \theta_2} & \frac{\partial f_2}{\partial \theta_3} \end{bmatrix}^{-1} \begin{bmatrix} f_1 \\ f_2 \end{bmatrix} \quad (\text{A.24})$$

B. POINT CONTACT METHOD DERIVATION

To consider the frictional effects between the cable and the cable route, the friction were applied at the contacting points of the phalanges which are the start and the end of the cable route at each phalanx. It was assumed that the cable is only contacting the start and the end of the route except for the curvature of the cable route inside of the distal phalanx. The friction was applied around the surface of the curvature using the capstan equation described in Appendix C.

$$T_{a1} = T_{a0}e^{\mu\phi} \quad (\text{B.1})$$

Using the equation B.1, the frictional effects from the surface of the curvature are taken into account. For the friction effects around the sharp edges, the point contact friction method was applied. Figure B.1 shows the locations where the static friction is applied and Figure B.2 illustrates the free body diagram of the cable at different locations of the cable route. The direction of the normal force was assumed to be the

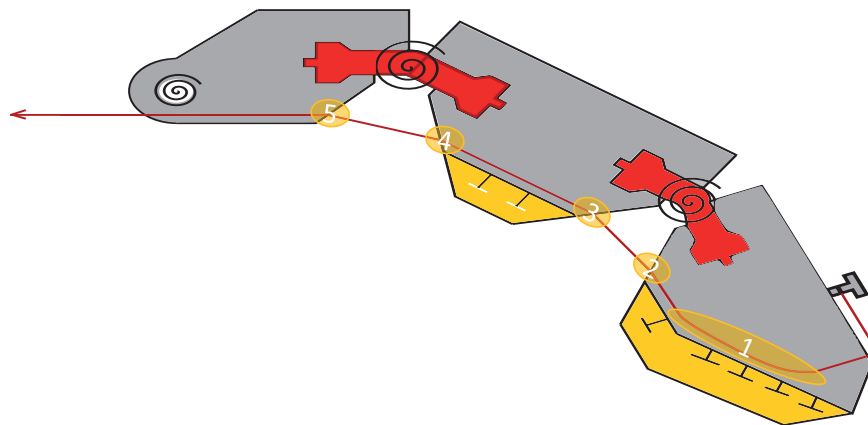


Fig. B.1. Location of the friction effects.

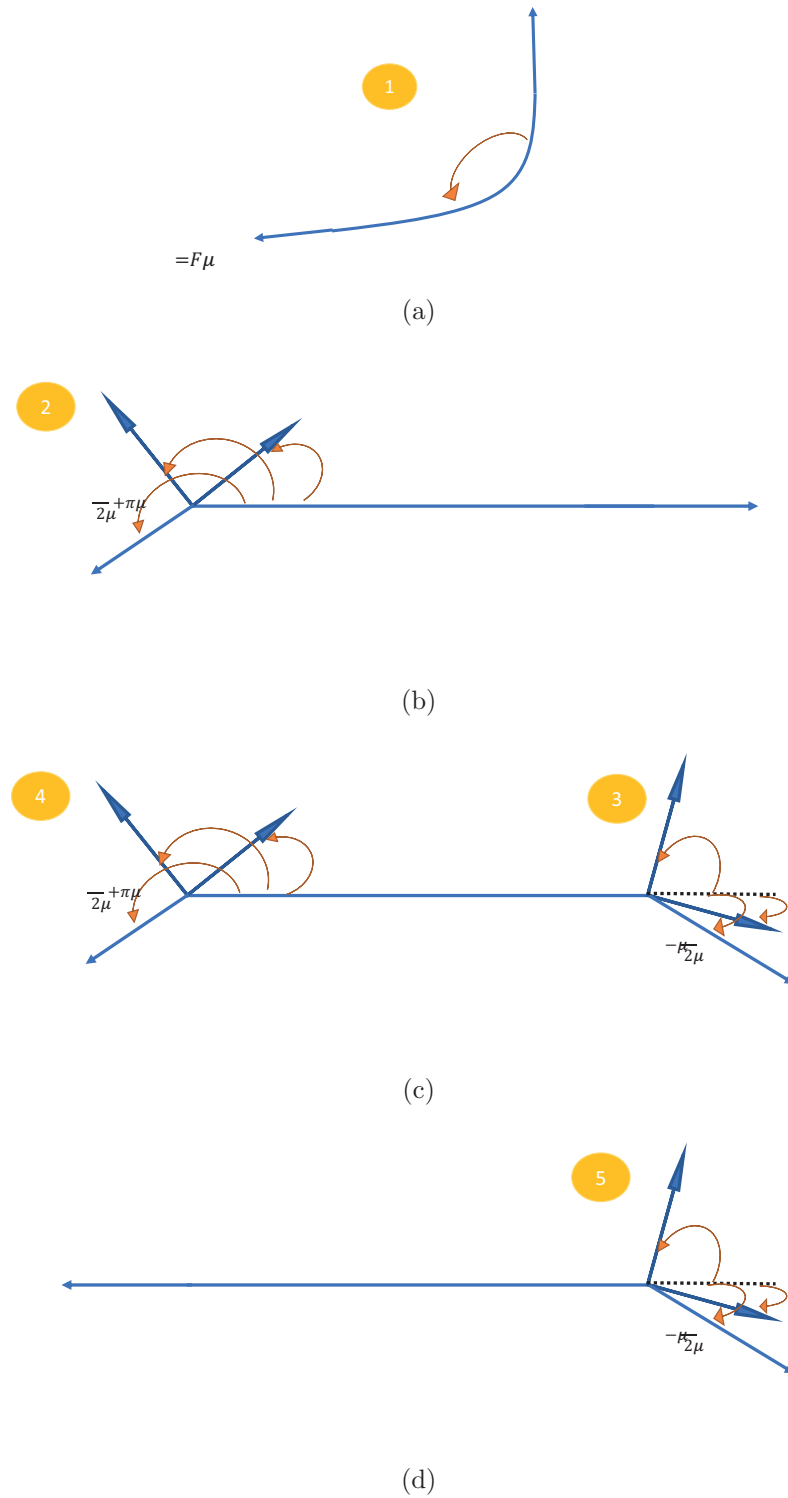


Fig. B.2. FBD of the cable at different location of the cable route (a) FBD of the cable at the curvature of the route (b) FBD of the cable at the end of the route inside of the DP (c) FBD of the cable at the IP (d) FBD of the cable at the PP.

half of the angle of the applied force at the each joint. Using the free body diagrams of each section of the cable, the force and moment equations can be determined. To start, using the known cable tension from Equation B.1, the tension of the cable including the frictional effect at the end of the cable route at the distal phalanx can be calculated.

$$F_x = 0 = N_1 \cos(\alpha_1) + N_1 \mu \cos(\beta_1) + F_{a2} \cos(\theta_3/2 + \pi) + F_{a1} \quad (\text{B.2})$$

$$F_y = 0 = N_1 \sin(\alpha_1) + N_1 \mu \sin(\beta_1) + F_{a2} \sin(\theta_3/2 + \pi) \quad (\text{B.3})$$

where

$$\alpha_1 = \frac{\theta_3/2 + \pi}{2} \quad (\text{B.4})$$

$$\beta_1 = \theta_3/4 \quad (\text{B.5})$$

Equation B.2 and B.3 can be put into as a matrix format as shown in Equation B.6 to solve the tension of the cable.

$$\begin{bmatrix} \cos(\alpha_1) + \mu \cos(\beta_1) & \cos(\theta_3/2 + \pi) \\ \sin(\alpha_1) + \mu \sin(\beta_1) & \sin(\theta_3/2 + \pi) \end{bmatrix} \begin{bmatrix} N_1 \\ F_{a2} \end{bmatrix} = \begin{bmatrix} -F_{a1} \\ 0 \end{bmatrix} \quad (\text{B.6})$$

Similarly, F_{a3} can be determined using the moment and force equations.

$$F_x = 0 = N_2 \cos(\alpha_2) + N_2 \mu \cos(\beta_2) + N_3 \cos(\alpha_3) + N_3 \mu \cos(\beta_3) + F_{a3} \cos(\theta_2/2 + \pi) + F_{a2} \cos(\theta_3/2) \quad (\text{B.7})$$

$$F_y = 0 = N_2 \sin(\alpha_2) + N_2 \mu \sin(\beta_2) + N_3 \sin(\alpha_3) + N_3 \mu \sin(\beta_3) + F_{a3} \sin(\theta_2/2 + \pi) + F_{a2} \sin(\theta_3/2) \quad (\text{B.8})$$

$$\begin{aligned}
M = 0 &= -R_2 \hat{i} \times ((N_3 \cos(\alpha_3) + \mu \cos(\beta_3) + F_{a3} \cos(\theta_2/2 + \pi)) \hat{i} \\
&\quad + (N_3 \sin(\alpha_3) + \mu \sin(\beta_3) + F_{a3} \sin(\theta_2/2 + \pi)) \hat{j}) \\
&= -R_2 (N_3 \sin(\alpha_3) + \mu \sin(\beta_3) + F_{a3} \sin(\theta_2/2 + \pi))
\end{aligned} \tag{B.9}$$

where

$$\alpha_2 = -\theta_3/4 + \pi/2 \tag{B.10}$$

$$\beta_2 = -\theta_3/4 \tag{B.11}$$

$$\alpha_3 = \theta_2/4 + \pi/2 \tag{B.12}$$

$$\beta_3 = \theta_2/4 \tag{B.13}$$

Equation 3.11,3.12,3.13 can be put into as a matrix format as show in Equation B.14.

$$\begin{bmatrix} \cos(\alpha_2) + \mu \cos(\beta_2) & \cos(\alpha_3) + \mu \cos(\beta_3) & \cos(\theta_2/2 + \pi) \\ \sin(\alpha_2) + \mu \sin(\beta_2) & \sin(\alpha_3) + \mu \sin(\beta_3) & \sin(\theta_2/2 + \pi) \\ 0 & R_2 \sin(\alpha_3) - R_2 \mu \sin(\beta_3) & -R_2 \sin(\theta_2/2 + \pi) \end{bmatrix} \begin{bmatrix} N_2 \\ N_3 \\ F_{a3} \end{bmatrix} = \begin{bmatrix} -F_{a2} \cos(\theta_3/2) \\ -F_{a2} \sin(\theta_3/2) \\ 0 \end{bmatrix} \tag{B.14}$$

Finally, by summing the forces in x and y direction, F_{a4} can be found.

$$F_x = 0 = N_4 \cos(\alpha_4) + N_4 \mu \cos(\beta_4) - F_{a4} \tag{B.15}$$

$$F_y = 0 = N_4 \sin(\alpha_4) + N_4 \mu \sin(\beta_4) \tag{B.16}$$

$$\begin{bmatrix} \cos(\alpha_4) + \mu \cos(\beta_4) & -1 \\ \sin(\alpha_4) + \mu \sin(\beta_4) & 0 \end{bmatrix} \begin{bmatrix} N_4 \\ F_{a4} \end{bmatrix} = \begin{bmatrix} -F_{a3} \cos(\theta_2/2) \\ -F_{a3} \sin(\theta_2/2) \end{bmatrix} \tag{B.17}$$

where

$$\alpha_4 = -\theta_2/4 + \pi/2 \quad (\text{B.18})$$

$$\beta_4 = -\theta_3/4 \quad (\text{B.19})$$

In Equation B.6, B.14, B.6, α and β define the direction of corresponding normal force and friction force respectively. By solving Equation B.6, B.14, B.6 consecutively, the tension of the cable including the effects of friction can be solved.

C. CAPSTAN EQUATION DERIVATION

To consider the friction around the edges of the cable route, the capstan equation is used. Using the capstan equation, the frictional force is applied around the contacting surfaces instead of considering the frictional force at a contacting point.

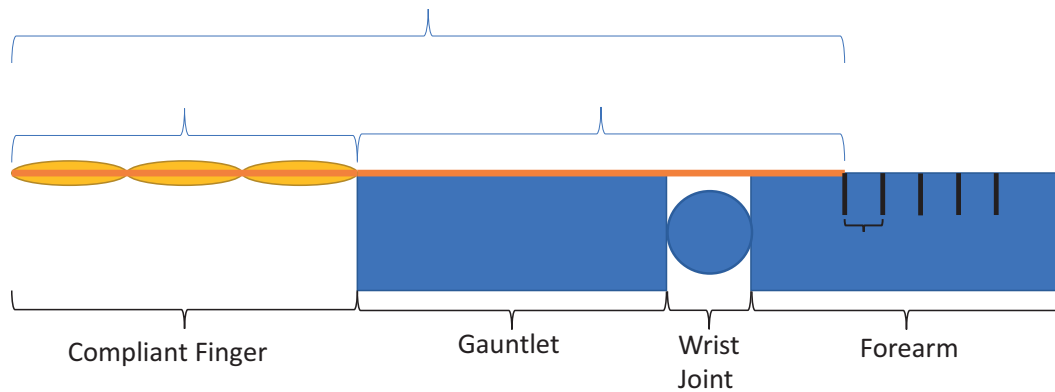


Fig. C.1. Free body diagram used to derive the capstan equation.

$$\hat{i} : 0 = T \cos(\Delta\theta/2) - f_s - (T + \Delta T) \cos(\Delta\theta/2) \quad (\text{C.1})$$

$$\hat{j} : 0 = -T \sin(\Delta\theta/2) + N - (T + \Delta T) \sin(\Delta\theta/2) \quad (\text{C.2})$$

Using small angle approximation, the equation can be simplified.

$$\begin{aligned} \hat{i} : 0 &= T \cos(\Delta\theta/2) - f_s - (T + \Delta T) \cos(\Delta\theta/2) \\ &\approx T - f_s - (T + \Delta T) \\ &= -f_s - \Delta T \end{aligned} \quad (\text{C.3})$$

$$\begin{aligned}
\hat{j} : 0 &= -T \sin(\Delta\theta/2) + N - (T + \Delta T) \sin(\Delta\theta/2) \\
&\approx -T\Delta\theta/2 + N - (T + \Delta T)\theta/2 \\
&= -T\Delta\theta + N - \Delta T\Delta\theta/2
\end{aligned} \tag{C.4}$$

Equation C.4 can be further simplified by ignoring $\Delta T\Delta\theta/2$ term because this term produces a small value in comparison to other terms. Using Equation C.4, the magnitude of the normal force is found.

$$\hat{j} : N = T\Delta\theta \tag{C.5}$$

The magnitude of static friction is shown in Equation C.6

$$f_s = \mu_s N \tag{C.6}$$

By combining Equations C.3 and C.6, following equation is found.

$$\Delta T = -\mu_s N \tag{C.7}$$

Now, the magnitude of normal force, Equation C.5, can be substituted into Equation C.8.

$$\begin{aligned}
0 &= -\mu_s T \Delta\theta - \Delta T \\
\frac{\Delta T}{\Delta\theta} &= -\mu_s T
\end{aligned} \tag{C.8}$$

$$\frac{dT}{d\theta} = -\mu_s T \tag{C.9}$$

$$\frac{T_{Load}}{T_{Hold}} \frac{dT}{T} = \frac{\theta_f}{\theta_i} \mu_s d\theta \tag{C.10}$$

$$\ln\left(\frac{T_{Load}}{T_{Hold}}\right) = -\mu_s(\theta_f - \theta_i) \tag{C.11}$$

$\theta_f - \theta_i$ is the magnitude of contact angle which can be represented as ϕ . By organizing Equations C.11 and C.12 can be found.

$$T_{Load} = T_{Hold} * e^{\mu_s \phi} \quad (C.12)$$

The capstan equation can be applied to derive the required input force to bend a finger.

$$F_{a_{new}} = F_{a_{prev}} \prod_{j=1}^5 e^{(\mu \phi_j)} \quad (C.13)$$

For the force controlled method, the input force starts from 0 and constantly increased. On the other hand for the cable length controlled method, the input force is derived from the one of the moment equations, Equations A.2 and A.4. By reorganizing one of those equations, following equation has been derived.

$$F_a = - \frac{k_2(\theta_2 - \theta_{2int})}{a_2 \sin(\frac{\theta_2}{2} + \pi) - b_2 \cos(\frac{\theta_3}{2} + \pi)} \quad (C.14)$$

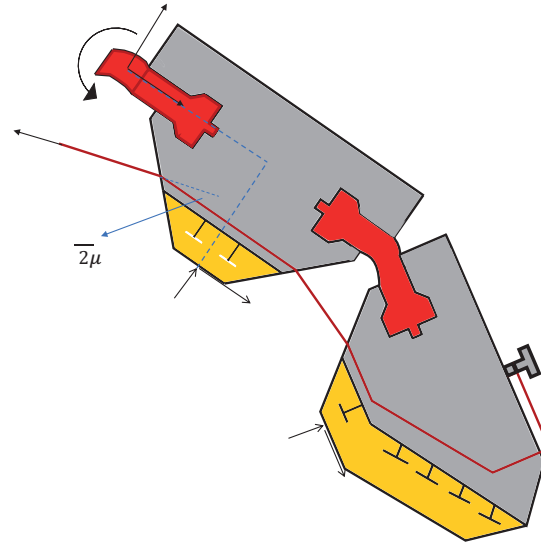
D. CONTACT FORCE ANALYSIS DERIVATION

The FBD of distal phalanx and intermediate phalanx is shown in Figure D.1(a) and D.1(b). Based on the FBDs, the moment equation of each phalanx is derived as shown in Equation D.2 and D.1.

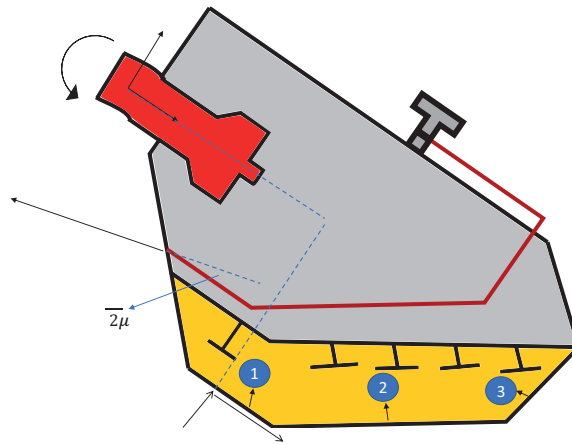
$$(a_3\hat{i}_3 + b_3\hat{j}_3) \times (F_{a3x}\hat{i}_3 + F_{a3y}\hat{j}_3) + (r_{c3x}\hat{i}_3 + r_{c3y}\hat{j}_3) \times (F_{c3x}\hat{i}_3 + F_{c3y}\hat{j}_3) + k_3(\theta_3 - \theta_{3int}) = 0 \quad (D.1)$$

$$(a_2\hat{i}_2 + b_2\hat{j}_2) \times (F_{a2x}\hat{i}_2 + F_{a2y}\hat{j}_2) + (r_{c2x}\hat{i}_2 + r_{c2y}\hat{j}_2) \times (F_{c2x}\hat{i}_2 + F_{c2y}\hat{j}_2) + (R_2\hat{i}_2 + r_{c3x}\hat{i}_3 + r_{c3y}\hat{j}_3) \times (F_{c3x}\hat{i}_3 + F_{c3y}\hat{j}_3) + k_2(\theta_2 - \theta_{2int}) = 0 \quad (D.2)$$

Figure D.2 indicates contact region 1,2 and 3 for the distal phalanx pad with angle between pad surfaces, γ_1 and γ_2 . γ_1 equals to 42.34 degrees and γ_2 equals to 47.66 degrees for this specific design. For this analysis, it was assumed that the contact force is perpendicular to the finger pad. Therefore, if the contact force is applied on region 2 and 3, then the coordinate of the force needs match with the coordinate frame of the moment arm which is in \hat{i}_1 and \hat{j}_1 coordinate frame.



(a)



(b)

Fig. D.1. FBD of the phalanges with contact forces (a)IP and DP (b)DP.

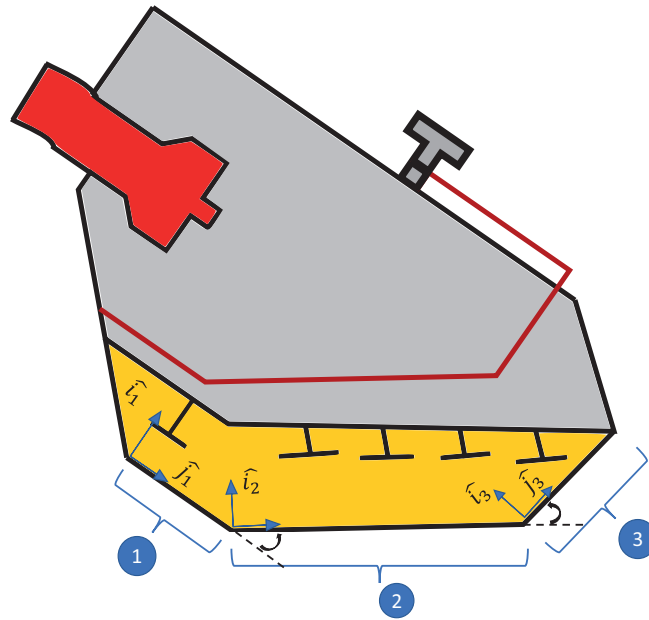


Fig. D.2. DP Finger Pad with Labels.

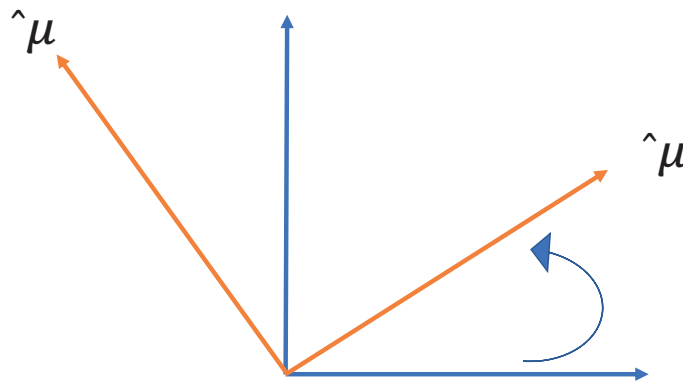


Fig. D.3. Rotation about Z axis.

The rotation matrix is based on Figure D.3.

$$\begin{bmatrix} \hat{i} \\ \hat{j} \end{bmatrix} = \begin{bmatrix} \cos \theta & -\sin \theta \\ \sin \theta & \cos \theta \end{bmatrix} \begin{bmatrix} \hat{X} \\ \hat{Y} \end{bmatrix} \quad (\text{D.3})$$

Equation D.4 shows the contact force in \hat{i}_1 and \hat{j}_1 coordinate frame for the contact force in different coordinate frame.

$$F_{c3y} = \begin{cases} F_{c3y} \hat{j}_1, & \text{if } F_{c3y} \text{ @ contact region 1} \\ F_{c3y} \cos(\gamma_1) \hat{i}_1 + F_{c3y} \sin(\gamma_1) \hat{j}_1, & \text{if } F_{c3y} \text{ @ contact region 2} \\ F_{c3y} \cos(\gamma_1 + \gamma_2) \hat{i}_1 + F_{c3y} \sin(\gamma_1 + \gamma_2) \hat{j}_1, & \text{if } F_{c3y} \text{ @ contact region 3} \end{cases} \quad (\text{D.4})$$

E. PRESHAPING DATA ANALYZING ALGORITHM

To start the program, the image to analyze has to be imported to the program. The program detects the tracking markers based on the color and the shape. The program has to extract the RGB color space and the user needs to determine which color space has the most contrast in color between the links and the tracking markers. Using that

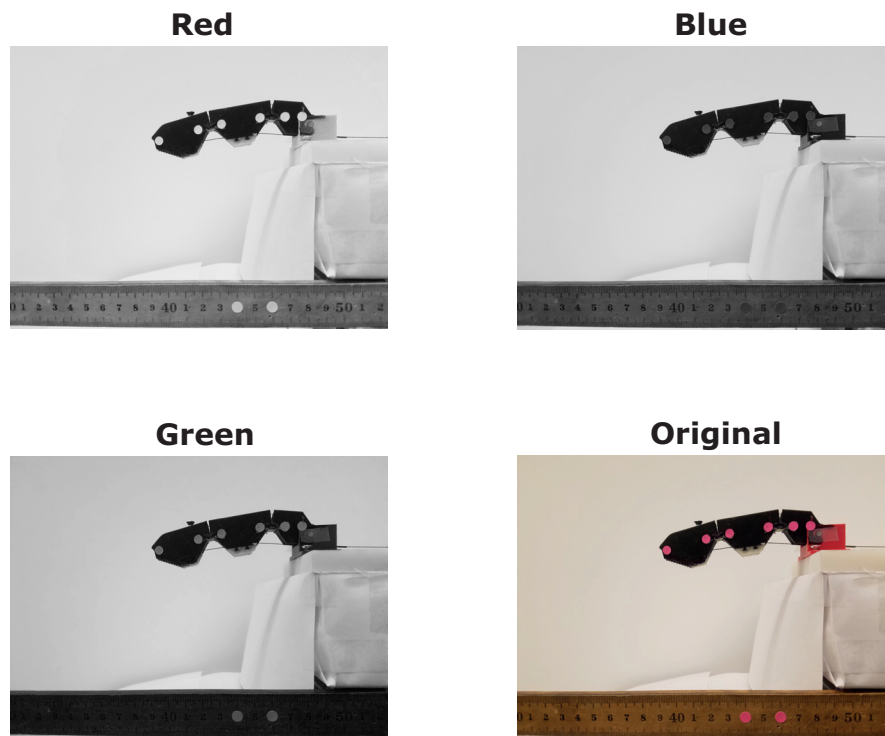


Fig. E.1. The extracted color data.

color space data and circle detection function, the location of the markers and the size of the markers are defined. Then, the data of the center positions is organized

based on the x and y coordinates of the markers. With the position of the markers, the slope of a line between two markers can be computed. The angle between two lines is calculated using the slope of the lines and Equation E.1.

$$\tan(\theta) = \frac{m_1 - m_2}{1 + m_1 m_2} \quad (\text{E.1})$$

where m is the slope of a line. The joint angles were calibrated using the initial joint angles where the hand is perfectly straight. Because the markers are not attached as a perfectly straight line, the offsets result from the alignment of the markers Figure E.2(a) shows the original image of the finger that needs to be processed. The RGB



Fig. E.2. Example of Conversion Process (a)Original image (b)Binary image of the red color space.

data is extracted and converted to a black and white image to see which color has the most contrast with the color of the link. As shown in Figure E.2(b), the red color has the most contrast in color between the finger and the markers. Therefore, the red color space from the original RGB data is converted to a binary image and used to detect the tracking stickers. By converting the image to a binary image, there is a clear color contrast between the markers and the hand that would help detecting the markers. Once the program successfully detects the markers, it puts a red circle around the detected marker and draw a blue line to the consecutive marker that is

detected. By looking at the processed image, it is clear to see whether the program has successfully detected all the markers or not. Figure E.3 shows a successfully processed image.



Fig. E.3. Processed image.

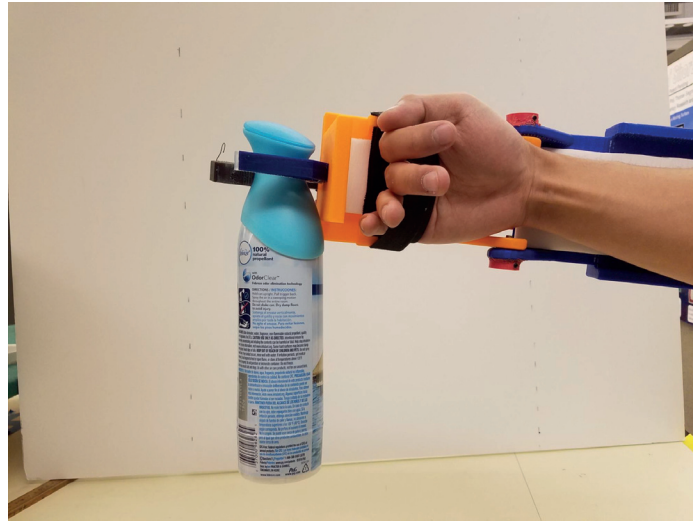
F. GRASPING DEMONSTRATION

F.1 Successful

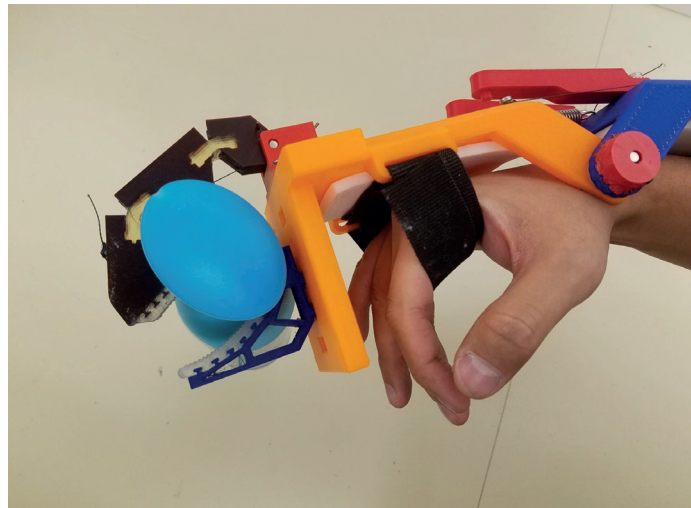
The objects shown in this section were successfully grasped without any trouble.



Fig. F.1. Cup.



(a)



(b)

Fig. F.2. Air refresher spray bottle. (a) Side view. (b) Top View

F.2 Partially Successful

The objects shown in this section were successfully grasping most of the times (> 70 %) if the objects are standing on the ground. However, if the objects are laying

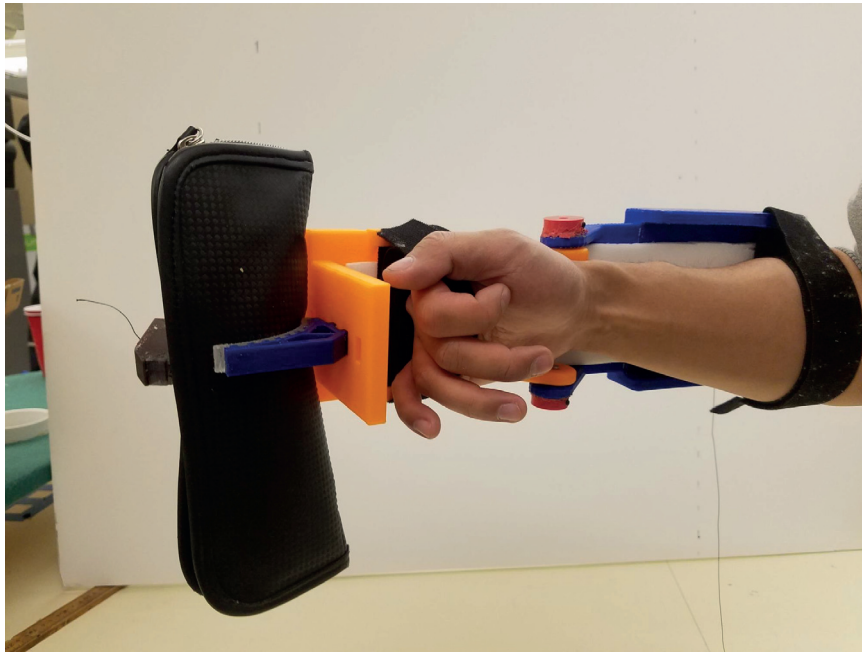


Fig. F.3. Pencil Case.

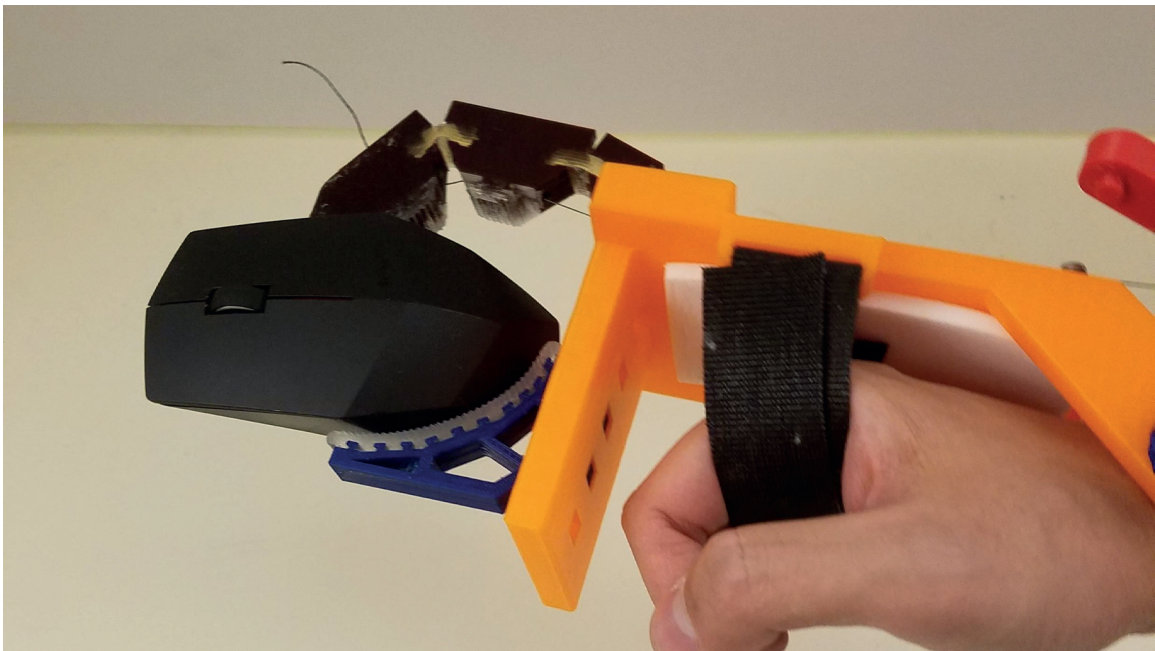


Fig. F.4. Computer mouse.



Fig. F.5. Umbrella.

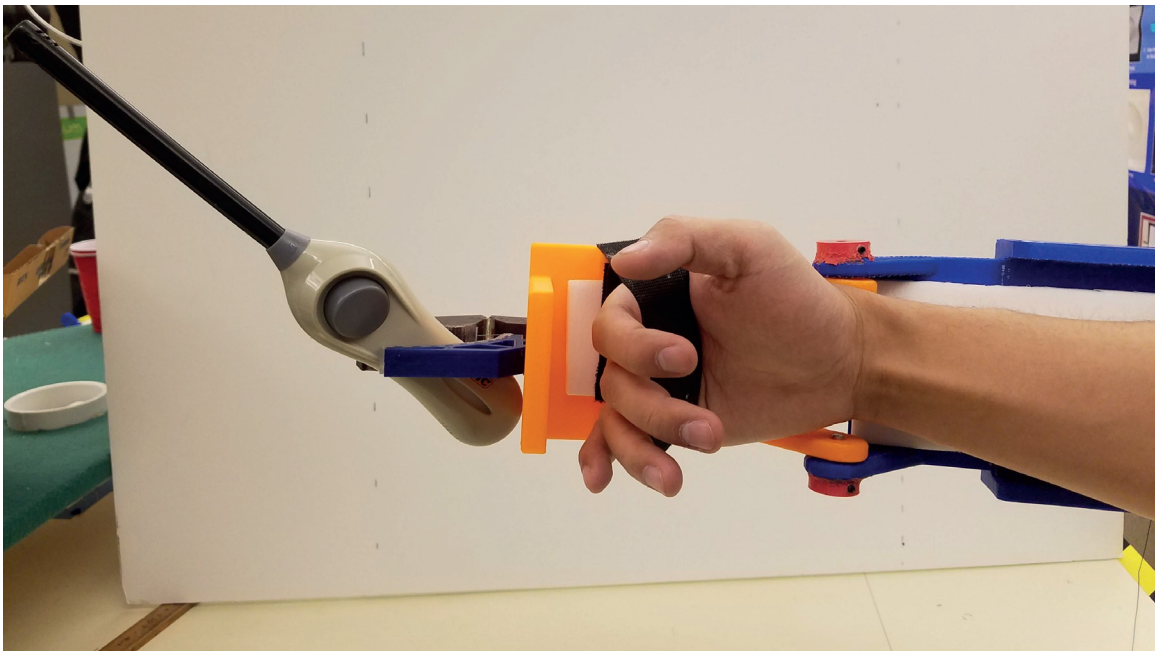


Fig. F.6. Lighter.



Fig. F.7. Knife.



Fig. F.8. Pen.

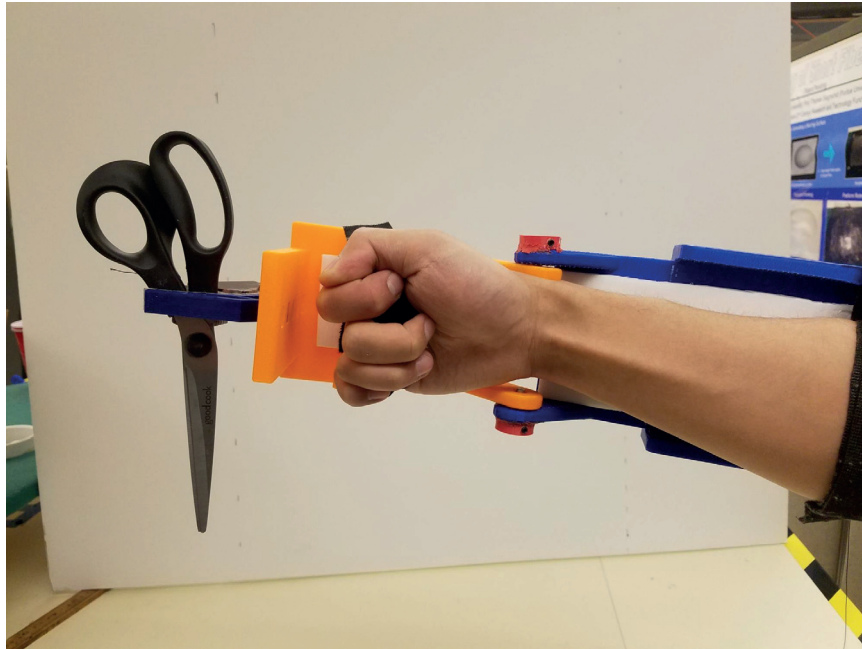


Fig. F.9. Scissor.

on the ground, then they were unsuccessful at grasping most of the times (< 15 30 %)

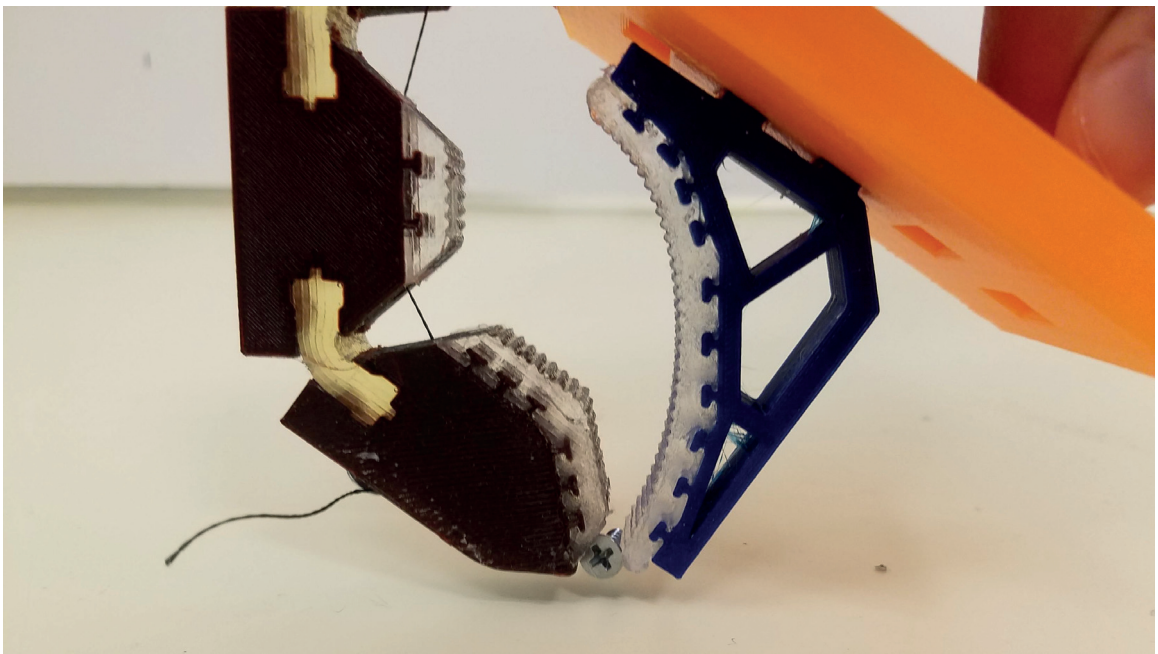


Fig. F.10. Screw.

F.3 Unsuccessful

The objects shown in this section were not able to be grasped.

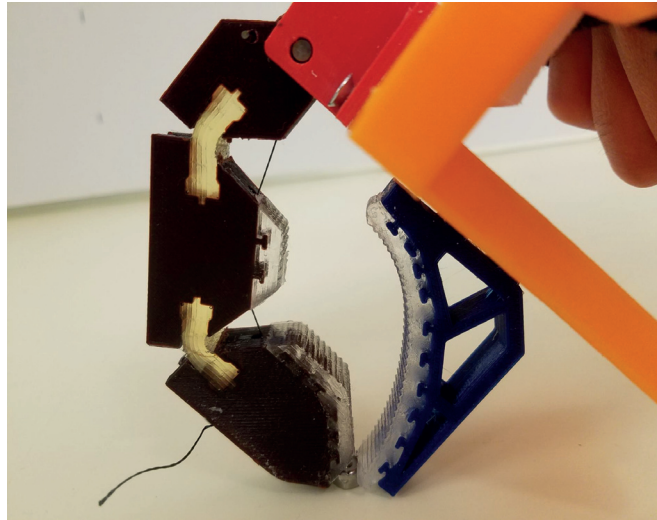


Fig. F.11. Nut.

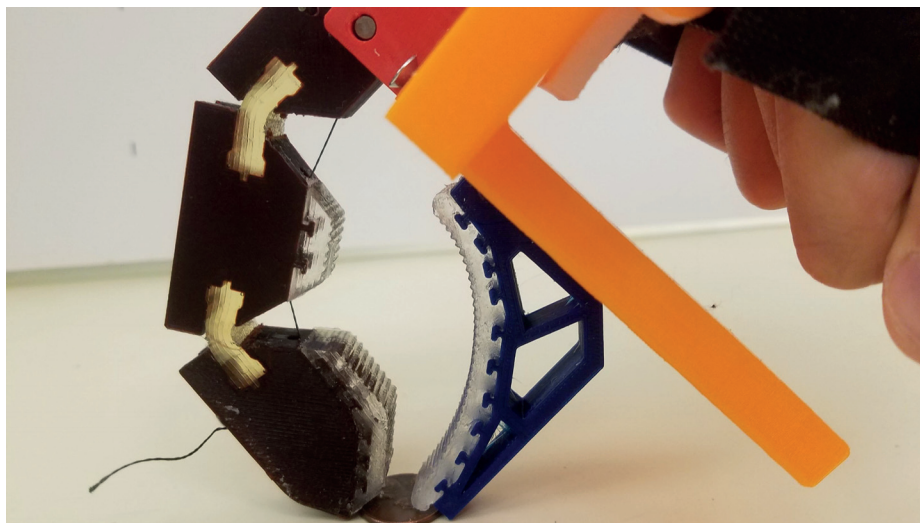


Fig. F.12. Coin.

G. MECHANISM DRAWINGS

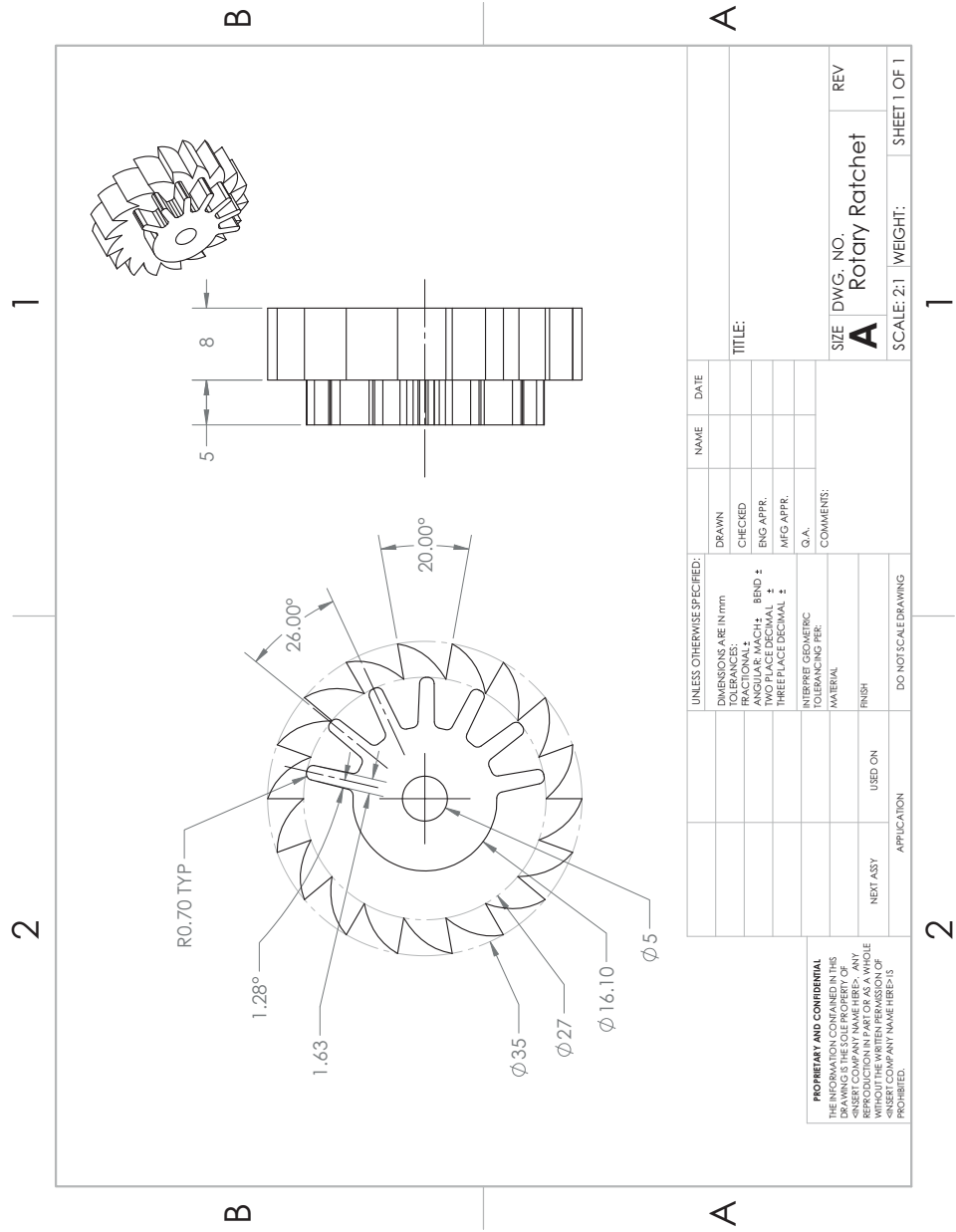


Fig. G.1. Rotary ratchet drawing.

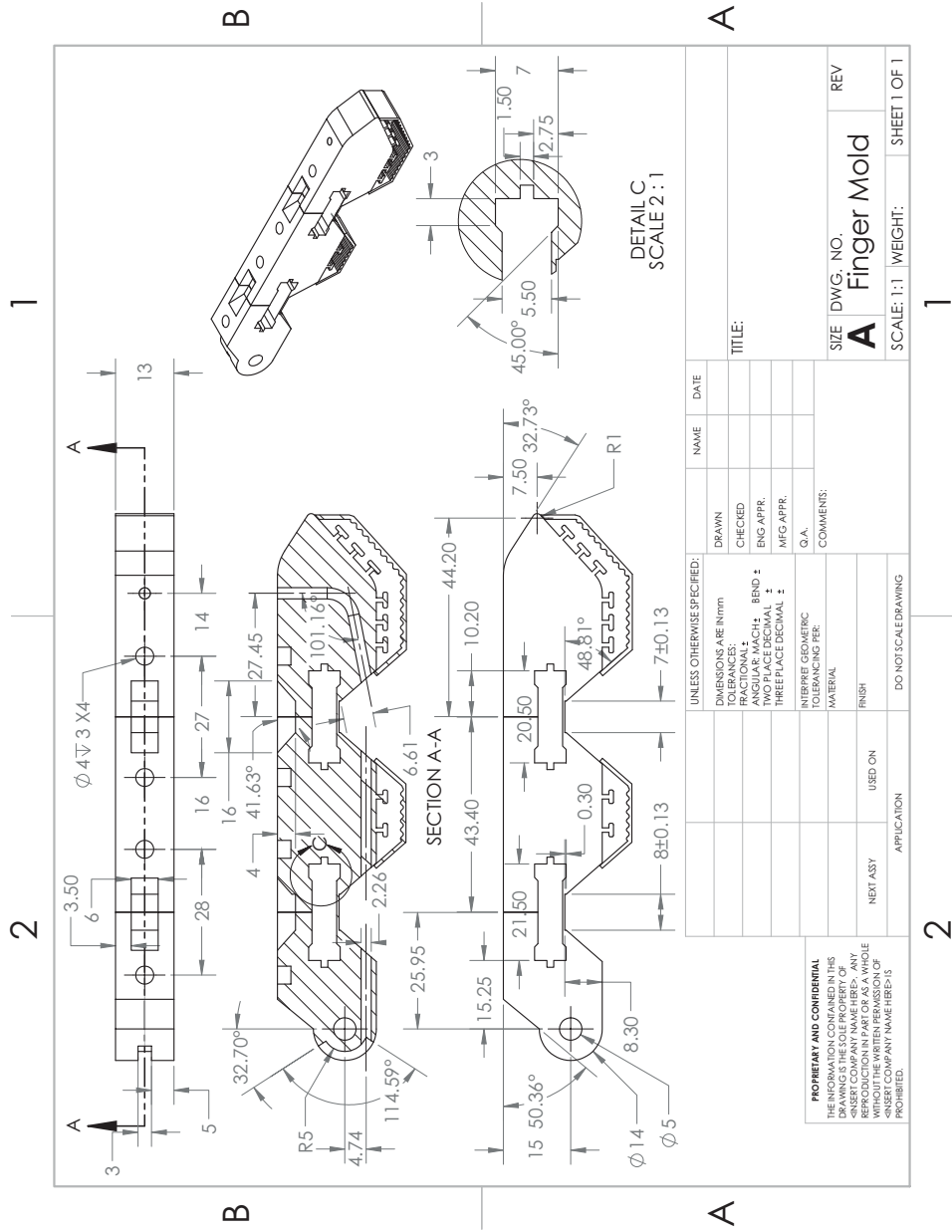
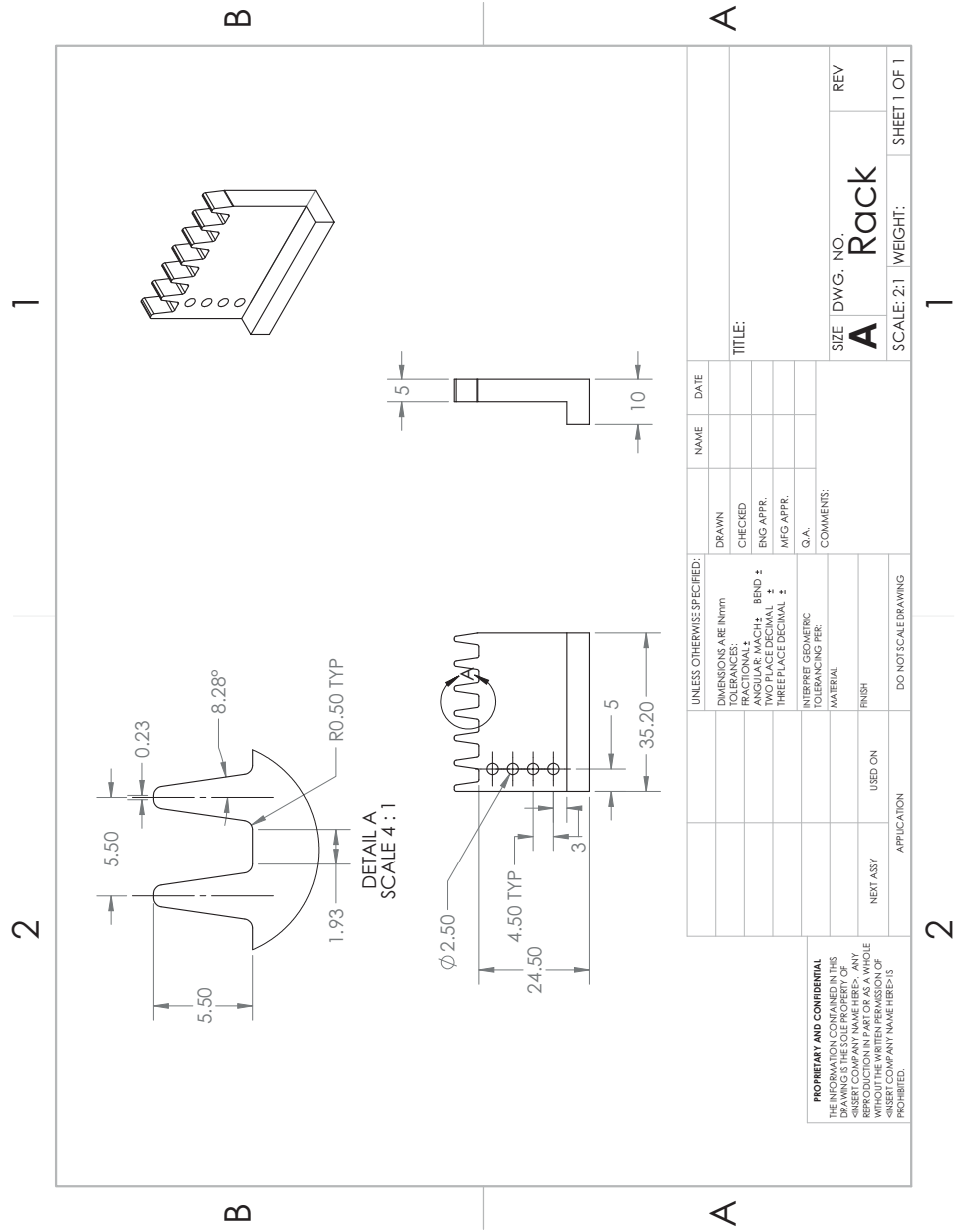


Fig. G.2. Compliant finger mold drawing.



<p>PROPRIETARY AND CONFIDENTIAL THE INFORMATION CONTAINED IN THIS DRAWING IS THE PROPERTY OF ANDREW COMPANY. NO PART OF THIS DRAWING IS TO BE REPRODUCED OR TRANSMITTED IN ANY FORM OR BY ANY MEANS, ELECTRONIC OR MECHANICAL, INCLUDING PHOTOCOPYING, RECORDING, OR BY ANY INFORMATION STORAGE AND RETRIEVAL SYSTEM, WITHOUT THE WRITTEN PERMISSION OF ANDREW COMPANY. NAME, ITEM NO. IS PROHIBITED.</p>		<p>UNLESS OTHERWISE SPECIFIED: DIMENSIONS ARE IN mm FINISH: RA 0.8 TOLERANCES: ANGULAR: MACH ± BEND ± TWO PLACE DECIMAL ± THREE PLACE DECIMAL ± MFG APPR. Q.A. COMMENTS:</p>		<p>NAME</p>	<p>DATE</p>
<p>DRAWN</p>	<p>CHECKED</p>	<p>ENG. APPR.</p>	<p>MFG APPR.</p>	<p>Q.A.</p>	<p>COMMENTS:</p>
<p>DO NOT SCALE DRAWING</p>					
<p>NEXT ASSY</p>	<p>USED ON</p>	<p>FINISH</p>	<p>SCALE: 2:1</p>	<p>WEIGHT:</p>	<p>SHEET 1 OF 1</p>
<p>APPLICATION</p>			<p>SIZE DWG. NO.</p>	<p>REV</p>	<p>TITLE:</p>
<p>A</p>			<p>A</p>	<p>Rack</p>	<p>1</p>

Fig. G.3. Rack drawing.

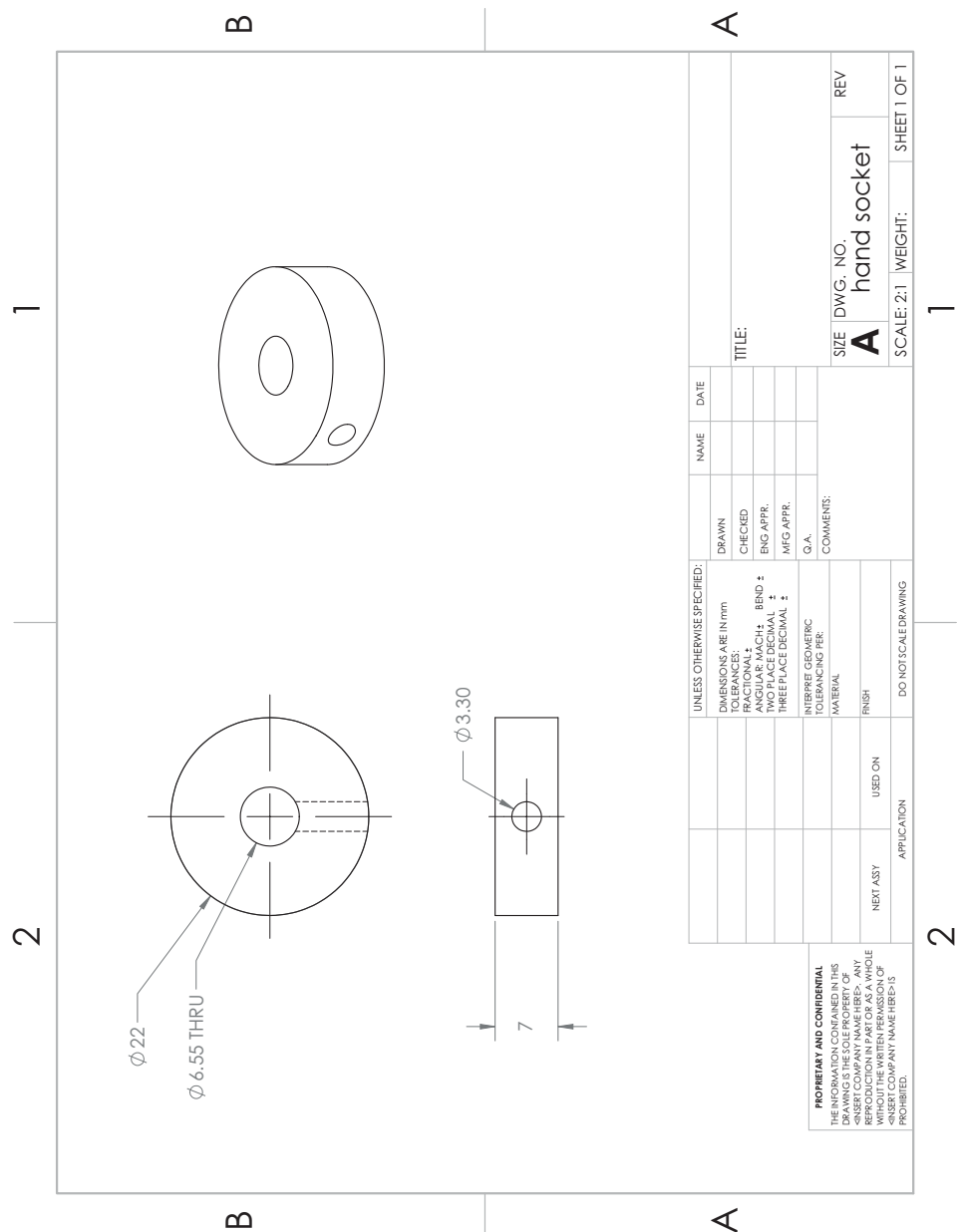


Fig. G.4. Hand socket drawing.

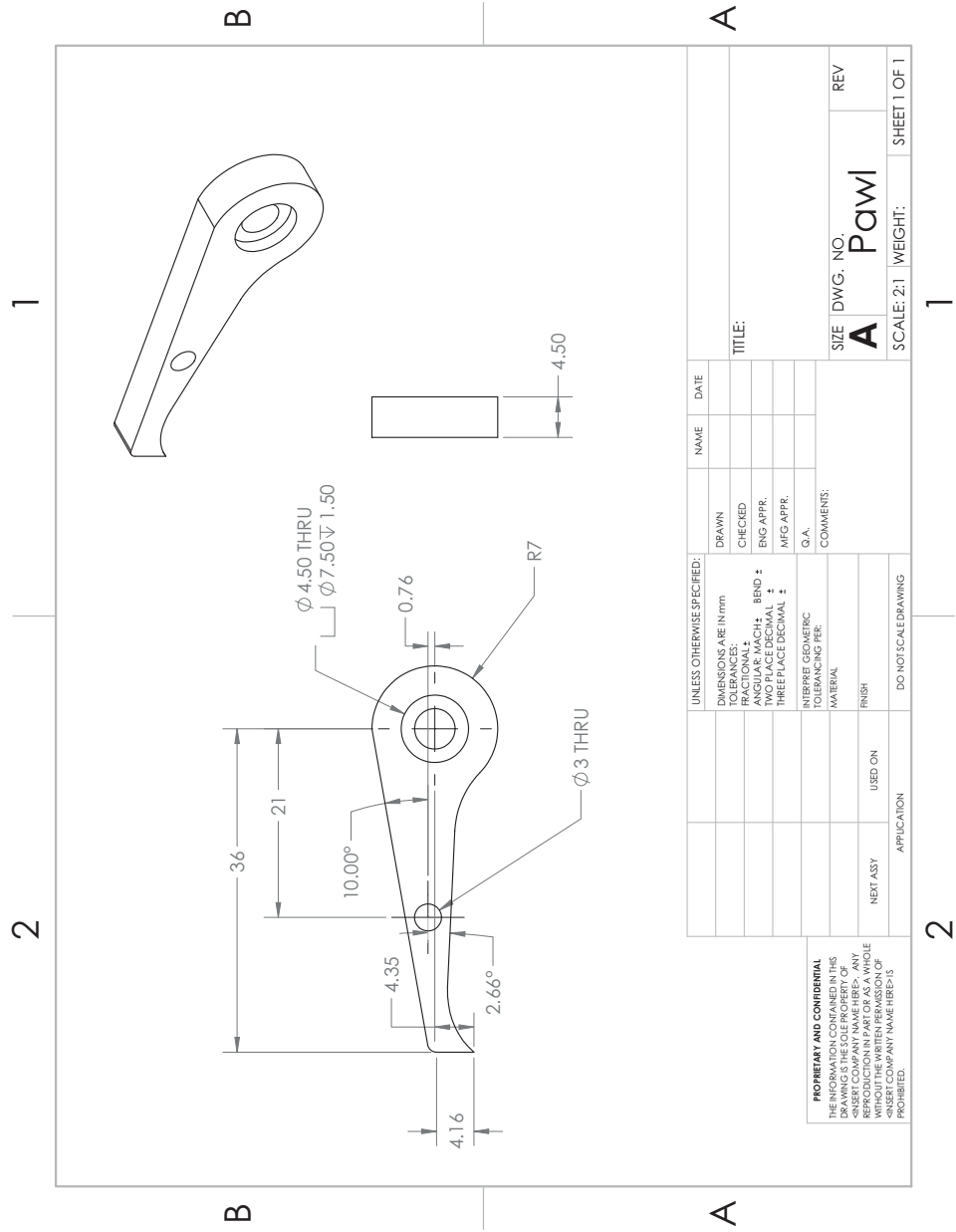
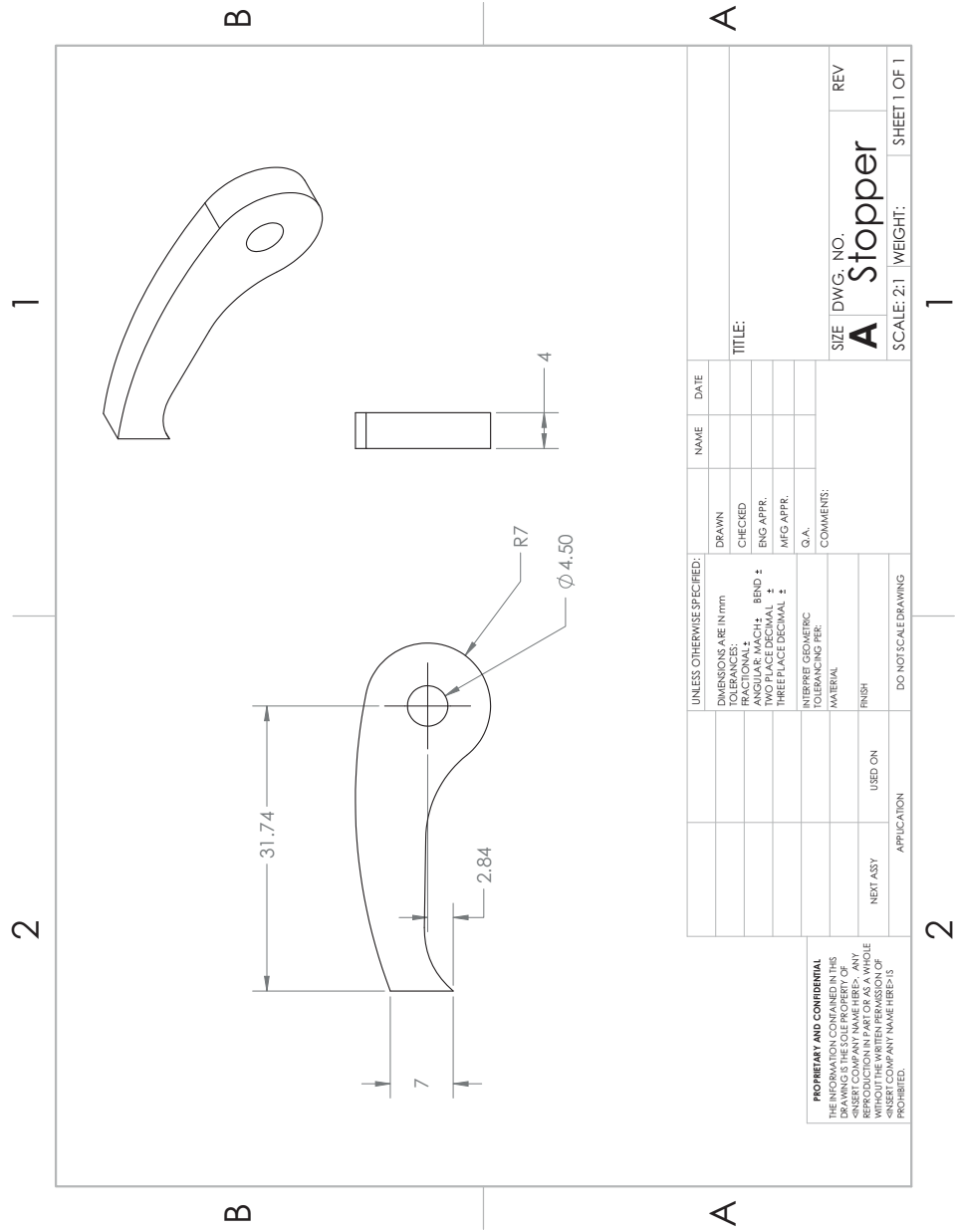


Fig. G.5. Pawl drawing.



<p>PROPRIETARY AND CONFIDENTIAL THE INFORMATION CONTAINED IN THIS DRAWING IS THE PROPERTY OF AND IS NOT TO BE REPRODUCED OR TRANSMITTED IN ANY FORM OR BY ANY MEANS, ELECTRONIC OR MECHANICAL, INCLUDING PHOTOCOPYING, RECORDING, REPRODUCTION IN PART OR AS A WHOLE WITHOUT THE WRITTEN PERMISSION OF THE COMPANY. COMPANY NAME (TYPED) IS PROHIBITED.</p>		UNLESS OTHERWISE SPECIFIED: DIMENSIONS ARE IN mm DECIMALS FRACTIONS ANGULAR: MACH: BEND : TWO PLACE DECIMAL : THREE PLACE DECIMAL : O.A. INTERPRET GEOMETRIC TOLERANCING PER: MATERIAL FINISH		DRAWN CHECKED ENG. APPR. MFG. APPR. Q.A. COMMENTS:	NAME DATE	TITLE: SIZE DWG. NO. A Stopper SCALE: 2:1 WEIGHT: SHEET 1 OF 1
		DO NOT SCALE DRAWING	NEXT ASSY USED ON APPLICATION	REV		

Fig. G.6. Stopper drawing.

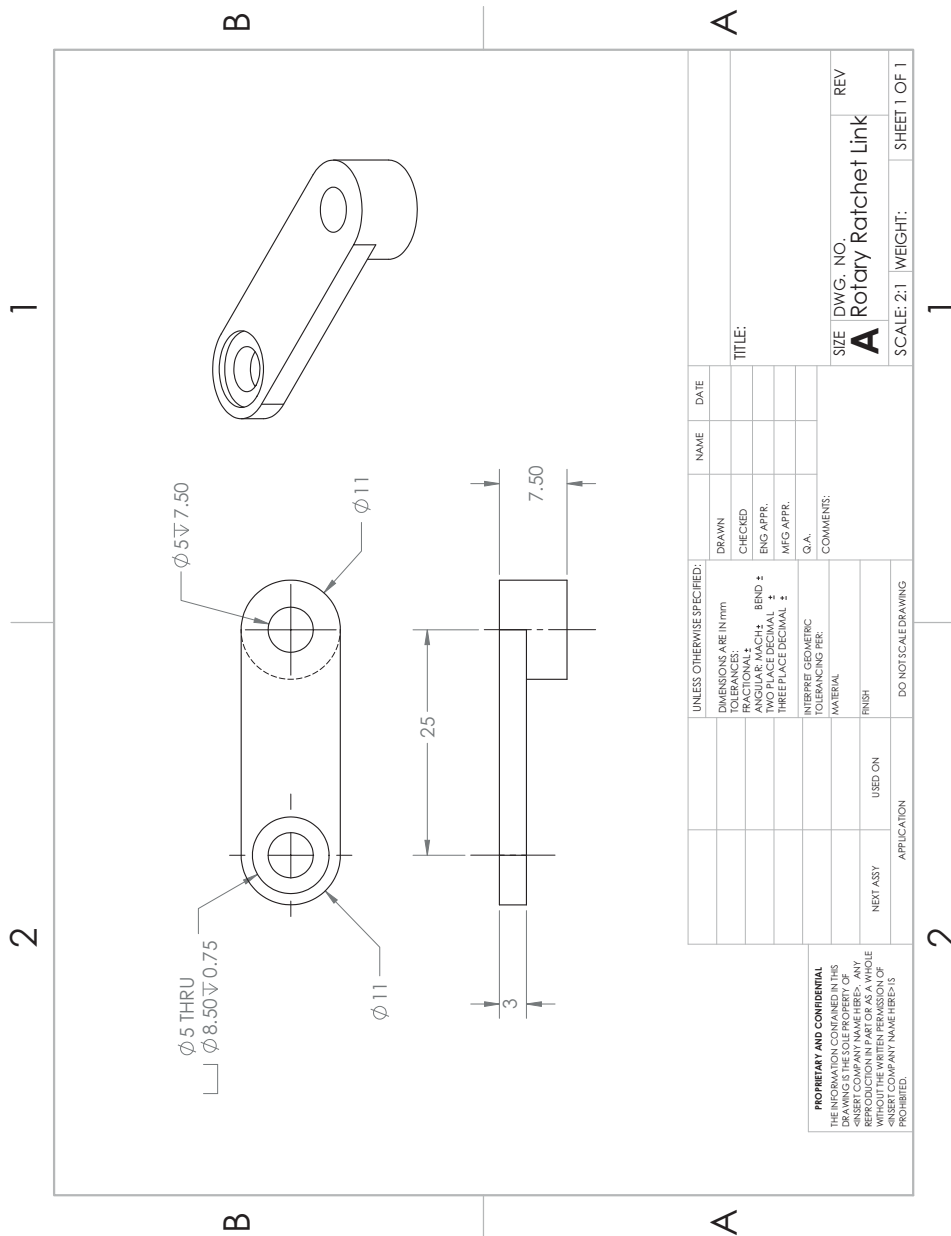


Fig. G.7. Rotary ratchet link drawing.

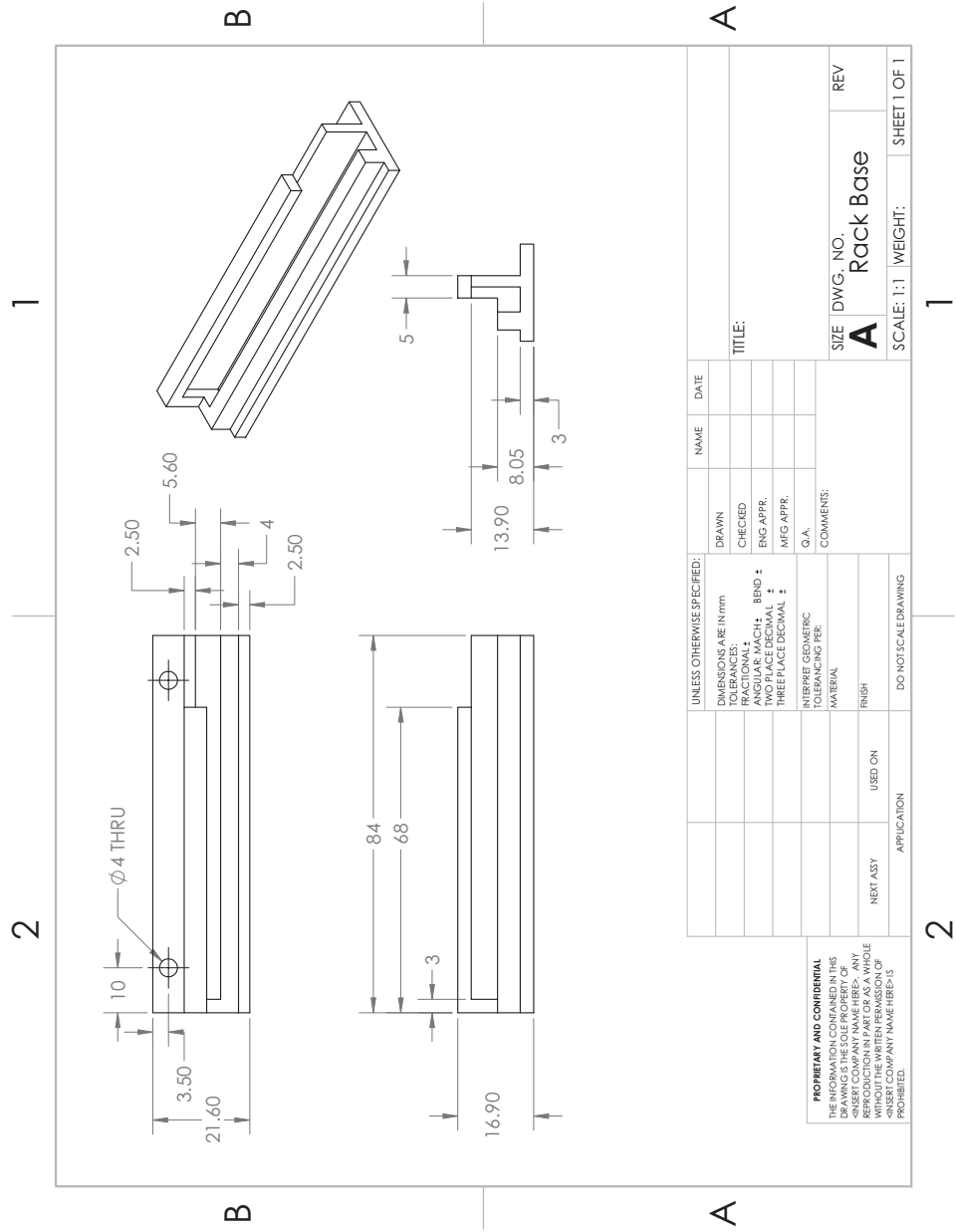


Fig. G.8. Rack base drawing.

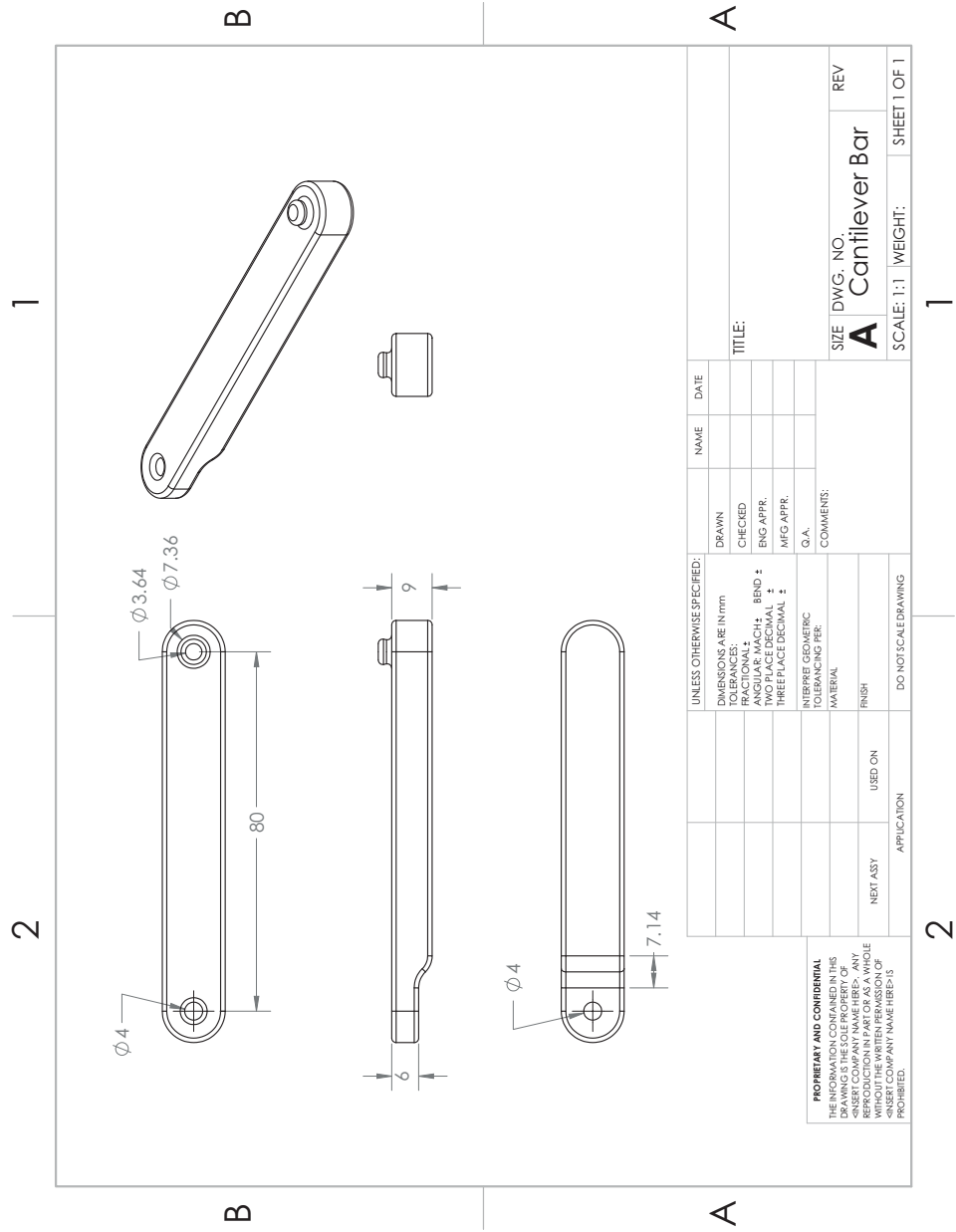


Fig. G.9. Cantilever bar structure.

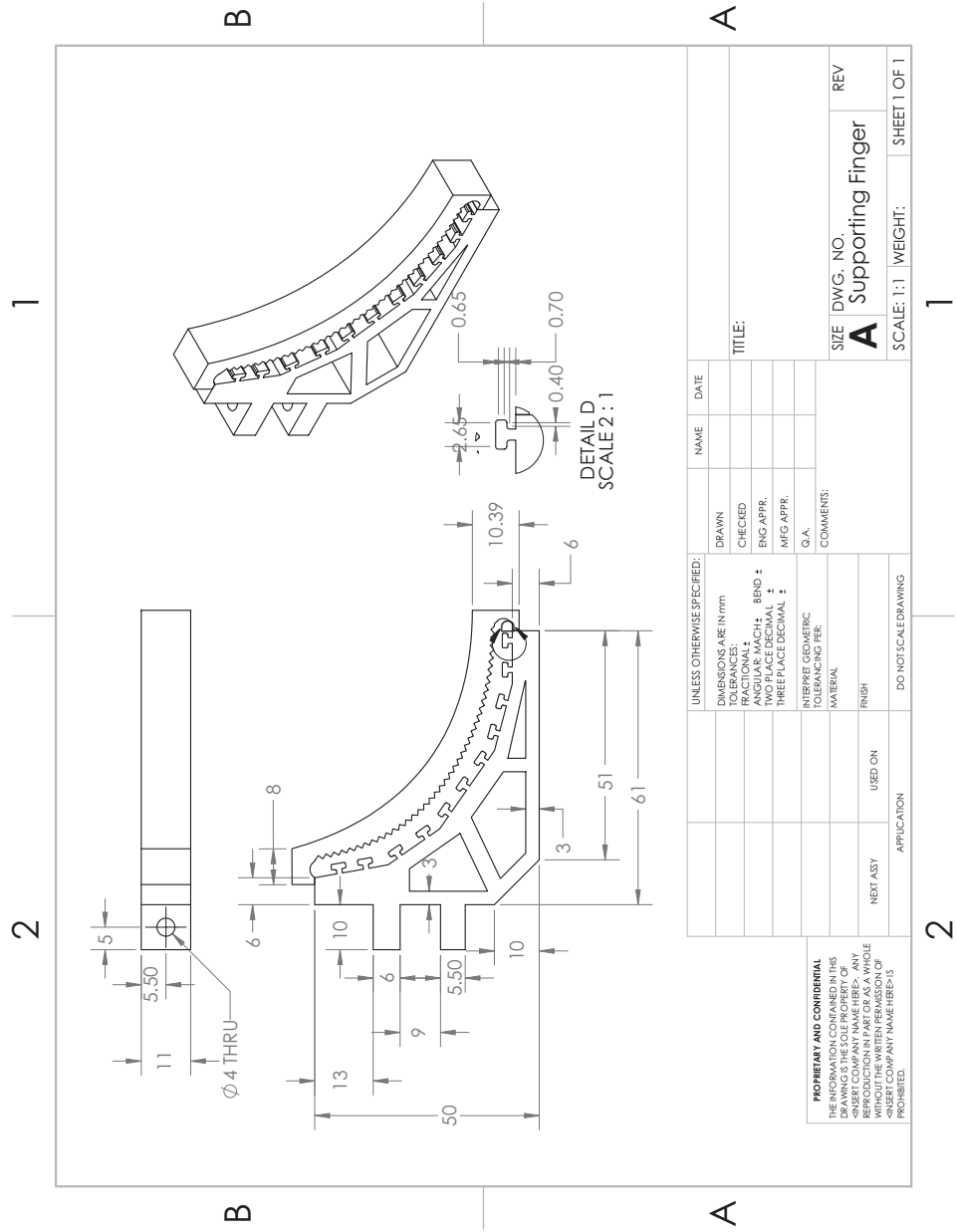


Fig. G.10. Supporting Finger.

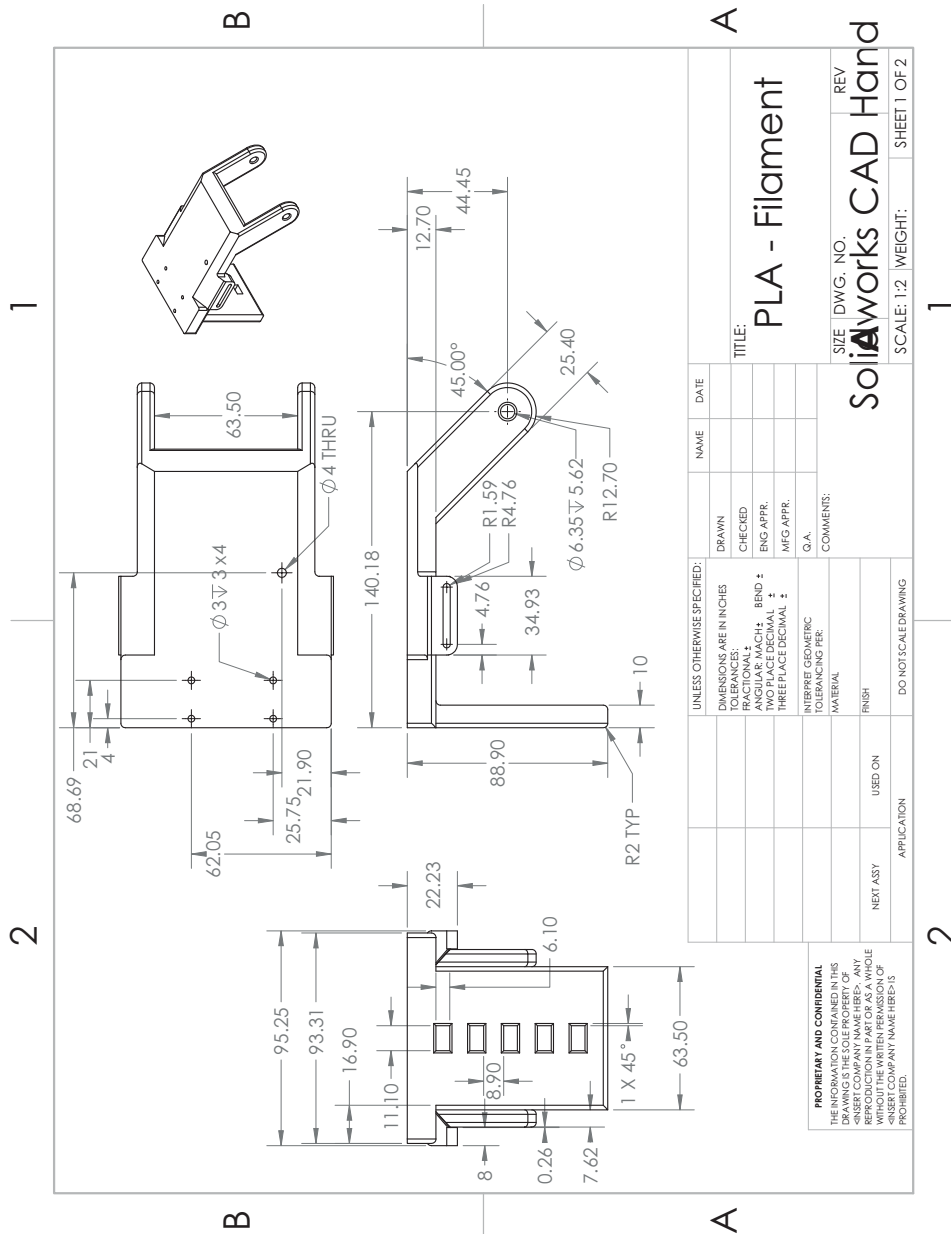


Fig. G.11. Gauntlet.

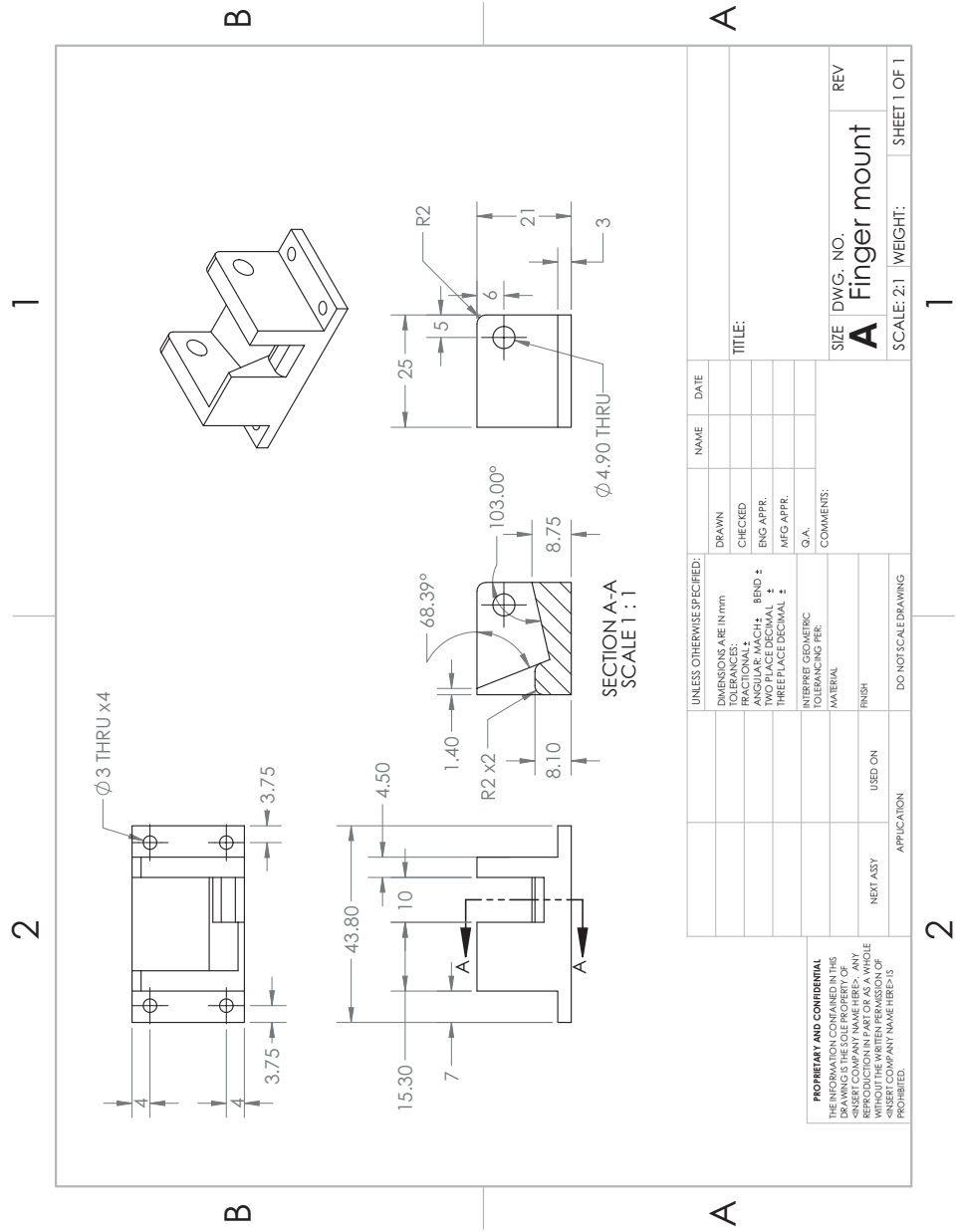


Fig. G.12. Finger mount.

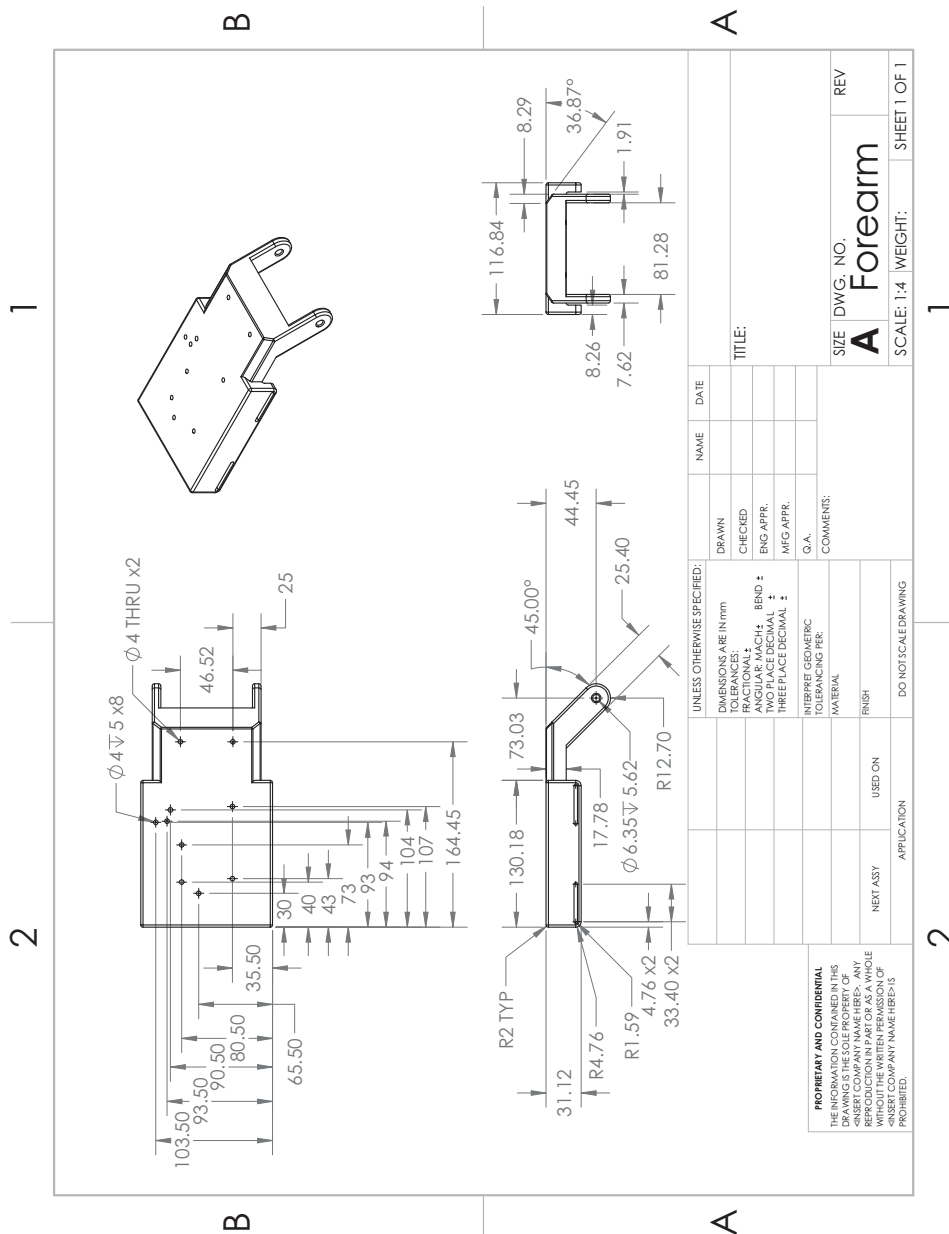


Fig. G.13. Forearm.

H. CODE

H.1 Preshaping - Input Force Control Using Point Contact Method

```

clear
clc

%%point contact method
%%Rack Position Controlled Method
%%Calculates the joint angles during the preshaping phase

%Link length
link_1 = 26.05/1000;
link_2 = 43.05/1000;
link_3 = 45.2/1000;

%Distance between the center of the joints and the cable route
a2=9.98/1000;
b2=-10.38/1000;

a3=9.48/1000;
b3=-10.38/1000;

alpha = degtorad(90);

%coefficient of friction
mu = 0.3;
%Radius of Pulley (Based on the length of the flexure joints)
Ra = 11.46/1000; %check the dimension of the actuator pully (not the partial gear)

%Flexure Joint
E = 2.756*10^6; %in Pa

%check/change values - flexure joints parameters %%%%%%%%%%%%%%%%%%%%%%%%%
b = 13/1000;
h = 5.5/1000;
%%%%%%%%%%%%%%%%%%%%%%%%
L_i = 8/1000;
L_d = 7/1000;
I = b*h^3/12;

k1 = 0.0535; %Nm/rad
k2 = E*I/L_i; %Nm/rad
k3 = E*I/L_d; %Nm/rad
k_fuse = 1696.979; %N/m

%Define Theta a
theta_a = degtorad(linspace(0,160,161));
num_ta = numel(theta_a);
theta_1 = degtorad(20);
theta_2 = degtorad(0);
theta_3 = degtorad(0);
theta_n2 = degtorad(0);
theta_n3 = degtorad(0);

i=1;
%initial estimate

%Newton Ralphson Method
while i <= 161
    del_t2 = 1;
    del_t3 = 1;
    while abs(del_t3) > 0.1 || abs(del_t2) > 0.1
        e1 = -Ra*theta_a(i)+ L_i - 2*(L_i/2)*cos(theta_2/2) +
2*(abs(b2))*sin(theta_2/2) +...
        L_d - 2*(L_d/2)*cos(theta_3/2) + 2*(abs(b3))*sin(theta_3/2);
        e2 = (a2*sin(theta_2/2+pi)-b2*cos(theta_2/2+pi))*k3*theta_3 - ...
(a3*sin(theta_3/2+pi)-b3*cos(theta_3/2+pi))*k2*theta_2;

```

```

df1_da2 = (L_i/2)*sin(theta_2/2)+abs(b2)*cos(theta_2/2);
df1_da3 = (L_d/2)*sin(theta_3/2)+abs(b3)*cos(theta_3/2);
df2_da2 = (a2/2*cos(theta_2/2+pi)+b2/2*sin(theta_2/2+pi))*k3*theta_3 - ...
(a3*sin(theta_3/2+pi)-b3*cos(theta_3/2+pi))*k2;
df2_da3 = -(a3/2*cos(theta_3/2+pi)+b3/2*sin(theta_3/2+pi))*k2*theta_2
+ ...
(a2*sin(theta_2/2+pi)-b2*cos(theta_2/2+pi))*k3;

A = [df1_da2, df1_da3;
df2_da2, df2_da3];
B = [-e1;-e2];
C = inv(A)*B;

del_t2 = C(1);
del_t3 = C(2);

theta_2 = theta_2 + del_t2;
theta_3 = theta_3 + del_t3;
end
d_theta_2(i) = radtodeg(theta_2);
d_theta_3(i) = radtodeg(theta_3);
d_theta_a(i) = radtodeg(theta_a(i));
o_theta_2(i) = -theta_2;
o_theta_3(i) = -theta_3;
theta_2p = -d_theta_2';
theta_3p = -d_theta_3';
i = i+1;
end
i=i-1;
figure(1)
plot(d_theta_a(1:i),d_theta_2(1:i))
hold on
plot(d_theta_a(1:i),d_theta_3(1:i))
hold on
xlabel('Acutation Angle (deg)');
ylabel('\theta_2 and \theta_3 (deg)');
legend('\theta_2', '\theta_3', 'Location', 'southeast');
legend boxoff
title('The Changes in Joint Angles');

%Tension
for u = 1:i
    %Force
    Fa_n(u) = (k2*o_theta_2(u))/(a2*sin(-o_theta_2(u)/2+pi)-b2*cos(-
o_theta_2(u)/2+pi));
    Fa4(u) = Fa_n(u)*exp(mu*(-o_theta_3(u)/2))*exp(mu*(degtorad(78.83)));
    Fa3(u) = Fa4(u)*exp(mu*(-o_theta_3(u)/2));
    Fa2(u) = Fa3(u)*exp(mu*(-o_theta_2(u)/2));
    Fa1(u) = Fa2(u)*exp(mu*(-o_theta_2(u)/2));
    Fa0(u) = Fa1(u); %for experiment
    %Fa0(u) = Fa1(u); %actual

    %w/ Mechanical Fuse - subtracted distance elongated by spring
    d_fuse(u) = Fa0(u)/k_fuse;
    cable(u) = (Ra*theta_a(u) - d_fuse(u));
    cable(1) = 0;
    del_nt2 = 1;
    del_nt3 = 1;

    while abs(del_nt3) > 0.1 || abs(del_nt2) > 0.1
        e1 = -cable(u) + L_i - 2*(L_i/2)*cos(theta_n2/2) +
2*(abs(b2))*sin(theta_n2/2) + ...
L_d - 2*(L_d/2)*cos(theta_n3/2) + 2*(abs(b3))*sin(theta_n3/2);

```

```

e2 = (a2*sin(theta_n2/2+pi)-b2*cos(theta_n2/2+pi))*k3*theta_n3 - ...
      (a3*sin(theta_n3/2+pi)-b3*cos(theta_n3/2+pi))*k2*theta_n2;

df1_da2 = (L_i/2)*sin(theta_n2/2)+abs(b2)*cos(theta_n2/2);
df1_da3 = (L_d/2)*sin(theta_n3/2)+abs(b3)*cos(theta_n3/2);
df2_da2 = (a2/2*cos(theta_n2/2+pi)+b2/2*sin(theta_n2/2+pi))*k3*theta_n3
- ...
      (a3*sin(theta_n3/2+pi)-b3*cos(theta_n3/2+pi))*k2;
df2_da3 = -(a3/2*cos(theta_n3/2+pi)+b3/2*sin(theta_n3/2+pi))*k2*theta_n2
+ ...
      (a2*sin(theta_n2/2+pi)-b2*cos(theta_n2/2+pi))*k3;

A = [df1_da2, df1_da3;
      df2_da2, df2_da3];
B = [-e1;-e2];
C = inv(A)*B;

del_nt2 = C(1);
del_nt3 = C(2);

theta_n2 = theta_n2 + del_nt2;
theta_n3 = theta_n3 + del_nt3;
end
d_theta_n2(u) = radtodeg(theta_n2);
d_theta_n3(u) = radtodeg(theta_n3);
cable_na(u) = cable(u);
end
Fa_trans = Fa_n';
Fa_0 = Fa0';
Fa2p = Fa2';

figure(2)
plot(d_theta_a(1:u),Fa_trans,d_theta_a(1:u),Fa_0);
xlabel('\theta_a (deg)');
ylabel('F_a (N)');
title('Required Tension Force wrt Actuation Angle');
legend('w/o friction','w/ friction','Location','southeast');
legend boxoff

figure(10)
plot(d_theta_a(1:u)',d_theta_n2',d_theta_a(1:u)',d_theta_n3');
xlabel('\theta_a(deg)');
ylabel('\theta_2 and \theta_3 (deg)');
legend('\theta_2','\theta_3','Location','southeast');
legend boxoff
title('The Changes in Joint Angles (w/ Spring)');

```

H.2 Preshaping - Input Force Control Using Capstan Equation Method

```

clear
clc

%capstan equation method
%considers friction on the cable and uses matrix to solve for the normal
%forces and cable force on the cable at the same time
%%

%Calculates the joint angles during the preshaping phase
%This is based on virtual work and the constraint equation

%Link length
link_1 = 26.05/1000;
link_2 = 43.05/1000;
link_3 = 45.2/1000;

a2=9.98/1000;
b2=-10.38/1000; %%%%%%%%%%%%%%%%%%%%%%%%%change%%%%%%%%%%%%%%%%%%%%%%%%%

a3=9.48/1000;
b3=-10.38/1000; %%%%%%%%%%%%%%%%%%%%%%%%%change%%%%%%%%%%%%%%%%%%%%%%%%%

alpha = degtorad(90);

%coefficient of friction
mu = 0.3;
%Radius of Pulley (Based on the length of the flexure joints)
Ra = 11.46/1000; %check the dimension of the actuator pully (not the partial gear)

%Flexure Joint
%shore = 80;
%E = exp(shore*0.0235-0.6403)*(10^6); %in Pa
E = 2.756*10^6;

%check/change values - flexure joints%%%%%%%%%%%%%%%%%%%%%%%%%
b = 13/1000;
h = 5.5/1000;
%%%%%%%%%%%%%%%%%%%%%%%%%
L_i = 8/1000;
L_d = 7/1000;
I = b*h^3/12;

k1 = 0.0535; %Nm/rad
k2 = E*I/L_i; %Nm/rad
k3 = E*I/L_d; %Nm/rad %fix-----
k_fuse = 1696.979; %N/m

%Define Theta a
Fa = linspace(0,7,161);
theta_a = degtorad(0);
theta_1 = degtorad(20);
theta_2 = degtorad(100);
theta_3 = degtorad(100);
theta_n2 = degtorad(0);
theta_n3 = degtorad(0);

i=1;
u=1;
%initial estimate

while i <= 161

```



```

del_t2 = 1;
del_t3 = 1;
del_ta = 1;
u=1;
while abs(del_t3) > 0.0001 || abs(del_t2) > 0.0001 || abs(del_ta) > 0.0001
e1 = -Ra*theta_a+ L_i - 2*(L_i/2)*cos(theta_2/2) +
2*(abs(b2))*sin(theta_2/2) +...
L_d - 2*(L_d/2)*cos(theta_3/2) + 2*(abs(b3))*sin(theta_3/2);
e2 = Fa(i)*(a2*sin(theta_2/2+pi)-b2*cos(theta_2/2+pi)) + k2*theta_2;
e3 = Fa(i)*(a3*sin(theta_3/2+pi)-b3*cos(theta_3/2+pi)) + k3*theta_3;

df1_da = -Ra;
df1_da2 = (L_i/2)*sin(theta_2/2)+abs(b2)*cos(theta_2/2);
df1_da3 = (L_d/2)*sin(theta_3/2)+abs(b3)*cos(theta_3/2);
df2_da = 0;
df2_da2 = Fa(i)*(-a2/2*sin(theta_2/2+pi)-b2/2*cos(theta_2/2+pi))+k2;
df2_da3 = 0;
df3_da = 0;
df3_da2 = 0;
df3_da3 = Fa(i)*(-a3/2*sin(theta_3/2+pi)-b3/2*cos(theta_3/2+pi))+k3;

A = [df1_da,df1_da2, df1_da3;
df2_da,df2_da2, df2_da3;
df3_da,df3_da2, df3_da3];
B = [-e1;-e2;-e3];
C = inv(A)*B;

del_ta = C(1);
del_t2 = C(2);
del_t3 = C(3);

theta_a = theta_a + del_ta;
theta_2 = theta_2 + del_t2;
theta_3 = theta_3 + del_t3;
u = u + 1;
end
d_theta_2(i) = radtodeg(theta_2);
d_theta_3(i) = radtodeg(theta_3);
d_theta_a(i) = radtodeg(theta_a);
o_theta_2(i) = theta_2;
o_theta_3(i) = theta_3;
theta_2p = -d_theta_2';
theta_3p = -d_theta_3';
s_theta_a(i) = theta_a;
i = i+1;
end

figure(1)
plot(Fa,d_theta_2)
hold on
plot(Fa,d_theta_3)
hold on
xlabel('Actuation Force (N)');
ylabel('Theta_2 and Theta_3 (deg)');
legend('\theta_2','\theta_3','Location','southeast');
title('The Changes in Joint Angles (w/o friction)');
legend('boxoff');

for u = 1:i-1
%Force
Fal(u) = Fa(u)*exp(mu*degtorad(78.83));
alpha_1(u) = (o_theta_3(u)/2+pi)/2;
beta_1(u) = (o_theta_3(u)/2+pi)/2-pi/2;
alpha_2(u) = (o_theta_3(u)/2+pi)/2-(o_theta_3(u)/2);

```

```

beta_2(u) = (o_theta_3(u)/2+pi)/2-(o_theta_3(u)/2)-pi/2;
alpha_3(u) = (o_theta_2(u)/2+pi)/2;
beta_3(u) = (o_theta_2(u)/2+pi)/2-pi/2;
alpha_4(u) = (o_theta_2(u)/2+pi)/2-(o_theta_2(u)/2);
beta_4(u) = (o_theta_2(u)/2+pi)/2-(o_theta_2(u)/2)-pi/2;

A = [cos(alpha_1(u))+mu*cos(beta_1(u)) cos(o_theta_3(u)/2+pi);
     sin(alpha_1(u))+mu*sin(beta_1(u)) sin(o_theta_3(u)/2+pi)];
B = [-Fa1(u);0];
C = inv(A)*B;
N_1(u) = C(1);
Fa2(u) = C(2);

AA = [cos(alpha_2(u))+mu*cos(beta_2(u)) cos(alpha_3(u))+mu*cos(beta_3(u))
      cos(o_theta_2(u)/2+pi);
      sin(alpha_2(u))+mu*sin(beta_2(u)) sin(alpha_3(u))+mu*sin(beta_3(u))
      sin(o_theta_2(u)/2+pi);
      0 -link_2*link_2*sin(alpha_3(u))-link_2*mu*sin(beta_3(u)) -
      link_2*sin(o_theta_2(u)/2+pi)];
BB = [-Fa2(u)*cos(-o_theta_3(u)/2);-Fa2(u)*sin(-o_theta_3(u)/2);0];
CC = inv(AA)*BB;
N_2(u) = CC(1);
N_3(u) = CC(2);
Fa3(u) = CC(3);

AAA = [cos(alpha_4(u))+mu*cos(beta_4(u)) -1;
       sin(alpha_4(u))+mu*sin(beta_4(u)) 0];
BBB = [-Fa3(u)*cos(-o_theta_2(u)/2); -Fa3(u)*sin(-o_theta_2(u)/2)];
CCC = inv(AAA)*BBB;
N_4(u) = CCC(1);
Fa4(u) = CCC(2);

Fa5(u) = Fa4(u)*exp(mu*deg2rad(90));
end

DP_Fa = Fa2'; % distal phalanx pull
IP_Fa = Fa3'; % intermediate phalanx pull
PP_Fa = Fa4'; % proximal phalanx pull
EXP_Fa = Fa5'; % For the experiment data
%Fa_0 = Fa0';
%Fa2p = Fa2';

figure(2)
plot(EXP_Fa,-theta_2p,EXP_Fa,-theta_3p);
xlabel('Actuation Tension (N)');
ylabel('Output angles (deg)');
title('The Change in Joint Angles (w/ friction)');
legend('\theta_2','\theta_3','Location','southeast');
legend('boxoff');

```

H.3 Preshaping - Rack Actuated Distance Control

```

clear
clc

%% Rack Position Controlled Method
%%Calculates the joint angles during the preshaping phase

%Link length
link_1 = 26.05/1000;
link_2 = 43.05/1000;
link_3 = 45.2/1000;

%Distance between the center of the joints and the cable
route
a2=9.98/1000;
b2=-10.38/1000;

a3=9.48/1000;
b3=-10.38/1000;

alpha = degtorad(90);

%coefficient of friction
mu = 0.3;
%Radius of Pulley (Based on the length of the flexure
joints)
Ra = 11.46/1000; %check the dimension of the actuator pully
(not the partial gear)

%Flexure Joint
E = 2.756*10^6; %in Pa

%check/change values - flexure joints
parameters %%%%%%%%%%%%%%%%%%%%%%%%%%
b = 13/1000;
h = 5.5/1000;
%%%%%%%%%%%%%%%%%%%%%%%%%%%%%%
L_i = 8/1000;
L_d = 7/1000;
I = b*h^3/12;

k1 = 0.0535; %Nm/rad
k2 = E*I/L_i; %Nm/rad
k3 = E*I/L_d; %Nm/rad

```

```

k_fuse = 1696.979; %N/m

%Define Theta a
theta_a = degtorad(linspace(0,140,141));
num_ta = numel(theta_a);
theta_1 = degtorad(20);
theta_2 = degtorad(0);
theta_3 = degtorad(0);
theta_n2 = degtorad(0);
theta_n3 = degtorad(0);

i=1;
%initial estimate

%Newton Ralphson Method
while i <= 141
    del_t2 = 1;
    del_t3 = 1;
    while abs(del_t3) > 0.1 || abs(del_t2) > 0.1
        e1 = -Ra*theta_a(i)+ L_i -
2*(L_i/2)*cos(theta_2/2) + 2*(abs(b2))*sin(theta_2/2) +...
        L_d - 2*(L_d/2)*cos(theta_3/2) +
2*(abs(b3))*sin(theta_3/2);
        e2 = (a2*sin(theta_2/2+pi)-
b2*cos(theta_2/2+pi))*k3*theta_3 - ...
        (a3*sin(theta_3/2+pi)-
b3*cos(theta_3/2+pi))*k2*theta_2;

        df1_da2 =
(L_i/2)*sin(theta_2/2)+abs(b2)*cos(theta_2/2);
        df1_da3 =
(L_d/2)*sin(theta_3/2)+abs(b3)*cos(theta_3/2);
        df2_da2 =
(a2/2*cos(theta_2/2+pi)+b2/2*sin(theta_2/2+pi))*k3*theta_3
- ...
        (a3*sin(theta_3/2+pi)-
b3*cos(theta_3/2+pi))*k2;
        df2_da3 = -
(a3/2*cos(theta_3/2+pi)+b3/2*sin(theta_3/2+pi))*k2*theta_2
+ ...
        (a2*sin(theta_2/2+pi)-
b2*cos(theta_2/2+pi))*k3;

        A = [df1_da2, df1_da3;

```

```

        df2_da2, df2_da3];
    B = [-e1;-e2];
    C = inv(A)*B;

    del_t2 = C(1);
    del_t3 = C(2);

    theta_2 = theta_2 + del_t2;
    theta_3 = theta_3 + del_t3;
end
d_theta_2(i) = radtodeg(theta_2);
d_theta_3(i) = radtodeg(theta_3);
d_theta_a(i) = radtodeg(theta_a(i));
o_theta_2(i) = -theta_2;
o_theta_3(i) = -theta_3;
theta_2p = -d_theta_2';
theta_3p = -d_theta_3';
i = i+1;
end
i=i-1;
figure(1)
plot(d_theta_a(1:i),d_theta_2(1:i))
hold on
plot(d_theta_a(1:i),d_theta_3(1:i))
hold on
xlabel('Acutation Angle (deg)');
ylabel('\theta_2 and \theta_3 (deg)');
legend('\theta_2', '\theta_3', 'Location', 'southeast');
legend boxoff
title('The Changes in Joint Angles (w/o spring)');

%Tension
for u = 1:i
    %Force
    Fa_n(u) = (k2*o_theta_2(u))/(a2*sin(-
o_theta_2(u)/2+pi)-b2*cos(-o_theta_2(u)/2+pi));
    Fa4(u) = Fa_n(u)*exp(mu*(-
o_theta_3(u)/2))*exp(mu*(degtorad(78.83)));
    Fa3(u) = Fa4(u)*exp(mu*(-o_theta_3(u)/2));
    Fa2(u) = Fa3(u)*exp(mu*(-o_theta_2(u)/2));
    Fa1(u) = Fa2(u)*exp(mu*(-o_theta_2(u)/2));
    Fa0(u) = Fa1(u); %for experiment
    %Fa0(u) = Fa1(u); %actual

```

```

    %w/ Mechanical Fuse - subtracted distance elongated by
spring
    d_fuse(u) = Fa0(u)/k_fuse;
    cable(u) = (Ra*theta_a(u) - d_fuse(u));
    cable(1) = 0;
    del_nt2 = 1;
    del_nt3 = 1;

    while abs(del_nt3) > 0.1 || abs(del_nt2) > 0.1
        e1 = -cable(u) + L_i - 2*(L_i/2)*cos(theta_n2/2)
+ 2*(abs(b2))*sin(theta_n2/2) + ...
            L_d - 2*(L_d/2)*cos(theta_n3/2) +
2*(abs(b3))*sin(theta_n3/2);
        e2 = (a2*sin(theta_n2/2+pi) -
b2*cos(theta_n2/2+pi))*k3*theta_n3 - ...
            (a3*sin(theta_n3/2+pi) -
b3*cos(theta_n3/2+pi))*k2*theta_n2;

        df1_da2 =
(L_i/2)*sin(theta_n2/2)+abs(b2)*cos(theta_n2/2);
        df1_da3 =
(L_d/2)*sin(theta_n3/2)+abs(b3)*cos(theta_n3/2);
        df2_da2 =
(a2/2*cos(theta_n2/2+pi)+b2/2*sin(theta_n2/2+pi))*k3*theta_n3 - ...
            (a3*sin(theta_n3/2+pi) -
b3*cos(theta_n3/2+pi))*k2;
        df2_da3 = -
(a3/2*cos(theta_n3/2+pi)+b3/2*sin(theta_n3/2+pi))*k2*theta_n2 + ...
            (a2*sin(theta_n2/2+pi) -
b2*cos(theta_n2/2+pi))*k3;

        A = [df1_da2, df1_da3;
            df2_da2, df2_da3];
        B = [-e1;-e2];
        C = inv(A)*B;

        del_nt2 = C(1);
        del_nt3 = C(2);

        theta_n2 = theta_n2 + del_nt2;
        theta_n3 = theta_n3 + del_nt3;
    end

```

```

    d_theta_n2(u) = radtodeg(theta_n2);
    d_theta_n3(u) = radtodeg(theta_n3);
    cable_na(u) = cable(u);
end
Fa_trans = Fa_n';
Fa_0 = Fa0';
Fa2p = Fa2';

figure(2)
plot(d_theta_a(1:u),Fa_trans,d_theta_a(1:u),Fa_0);
xlabel('Actuation Angle (deg)');
ylabel('Required Tension (N)');
title('Required Tension Force wrt Actuation Angle')
legend('w/o friction','w/
friction','Location','southeast');
legend boxoff

figure(10)
plot(d_theta_a(1:u)',d_theta_n2',d_theta_a(1:u)',d_theta_n3
');
xlabel('Acutation Angle (deg)');
ylabel('\theta_2 and \theta_3 (deg)');
legend('\theta_2','\theta_3','Location','southeast');
legend boxoff
title('The Changes in Joint Angles (w/ Spring)');

```

H.4 Preshaping Data Analyzing Code

```

clear
clc
%https://www.youtube.com/watch?v=1-jURfDzPls
%1st slope is the slope of two circles on the right
%%
I = imread('20180217_164053.jpg');

%%
%Compares RGB values of the image
r = I(:,:,1);
g = I(:,:,2);
b = I(:,:,3);
Ig = rgb2gray(I);

%Figure
% figure(2)
% subplot(2,2,1),imshow(r);
% title('Red');
% subplot(2,2,2),imshow(g);
% title('Blue');
% subplot(2,2,3),imshow(b);
% title('Green');
% subplot(2,2,4),imshow(I);
% title('Original');

%Adjust image intensity values
b = imadjust(b);
r = imadjust(r);
g = imadjust(g);
%%

%%%%%%%%%%%%%%%%%%%%%%%%%%%%%%%%%%%%%%%%%%%%%%%%%%%%%%%%%%%%%%%%%%%%%%%%adjust%%%%%%%%%%%%%%%%%%%%%%%%%%%%%%%%%%%%%%%%%%%%%%%%%%%%%%%%%%%%%%%%%%%%%%%%
%%%%%%%%%%%%%%%%%%%%%%%%%%%%%%%%%%%%%%%%%%%%%%%%%%%%%%%%%%%%%%%%%%%%%%%%
levelr = 0.754; %tolerance value
%%%%%%%%%%%%%%%%%%%%%%%%%%%%%%%%%%%%%%%%%%%%%%%%%%%%%%%%%%%%%%%%%%%%%%%%
%%%%%%%%%%%%%%%%%%%%%%%%%%%%%%%%%%%%%%%%%%%%%%%%%%%%%%%%%%%%%%%%%%%%%%%%
bw_R = im2bw(r,levelr); %Changing it to binary color -
black and white
%imshow(bw_R);

% wb_R = ~bw_R; % change BW image to WB image
% imshow(wb_R)
%%

```



```

%%%%%%%%%%%%%%%%%%%%%%%%%%%%%%%%%%%%%%%%%%%%%%%%%%%%%%%%%%%%%%%%%%%%%%%%adjust%%%%%%%%%%%%%%%%%%%%%%%%%%%%%%%%%%%%%%%%%%%%%%%%%%%%%%%%%%%%%%%%%%%%%%%%
%%%%%%%%%%%%%%%%%%%%%%%%%%%%%%%%%%%%%%%%%%%%%%%%%%%%%%%%%%%%%%%%%%%%%%%%
[center,radius] =
imfindcircles(r,[43,57],'ObjectPolarity','bright','Sensitivity',0.955); %[70-77] = approximate radius
%%%%%%%%%%%%%%%%%%%%%%%%%%%%%%%%%%%%%%%%%%%%%%%%%%%%%%%%%%%%%%%%%%%%%%%%
%%%%%%%%%%%%%%%%%%%%%%%%%%%%%%%%%%%%%%%%%%%%%%%%%%%%%%%%%%%%%%%%%%%%%%%%
num = length(center(:,1));
y=1;
for t = 1:num
    %Captured Area
    %%%%%%%%%%%%%%%%%%%%%%%%%%%%%%%%%%%%%%%%%%%%%%%%%%%%%%%%%%%%%%%%%%%%%%%%%adjust%%%%%%%%%%%%%%%%%%%%%%%%%%%%%%%%%%%%%%%%%%%%%%%%%%%%%%%%%%%%%%%%%%%%%%%%
    %%%%%%%%%%%%%%%%%%%%%%%%%%%%%%%%%%%%%%%%%%%%%%%%%%%%%%%%%%%%%%%%%%%%%%%%%
    if center(t,2) < 988 & center(t,2) > 230 & center(t,1)
> 1137 & center(t,1) < 3183%sets the limit to detect circle
    %%%%%%%%%%%%%%%%%%%%%%%%%%%%%%%%%%%%%%%%%%%%%%%%%%%%%%%%%%%%%%%%%%%%%%%%%
    %%%%%%%%%%%%%%%%%%%%%%%%%%%%%%%%%%%%%%%%%%%%%%%%%%%%%%%%%%%%%%%%%%%%%%%%%
        center_new(y,1) = center(t,1);
        center_new(y,2) = center(t,2);
        radius_n(y) = radius(t);
        y=y+1;
    end
end

%%
%Organizing the Data
num = length(center_new(:,1));
center_x = zeros(num,1);
center_y = zeros(num,1);
radius_new = zeros(num,1);
result = 0;
n = 1;

%Organize the data points by x and y location in
combination
% %organize by x location
% while n <= num %Keep on comparing the value until you
compared every centers
%     for m = 1:num
%         if center_new(n,1) <= center_new(m)
%             %+1 if the x coordinate of the center that
you are comparing is smaller than the center
%                 %that you are comparing with

```

```

%         result = result+1;
%     end
%     end
%     %6 = smallest x, 1 = largest
%     center_x(result) = center_new(n,1);
%     center_y(result) = center_new(n,2);
%     radius_new(result) = radius_n(n);
%     result = 0;
%     n = n + 1;
% end
% center_x2(1,1) = center_x(1);
% center_y2(1,1) = center_y(1);
% radius_new2(1,1) = radius_new(1);
% center_x2(2,1) = center_x(2);
% center_y2(2,1) = center_y(2);
% radius_new2(2,1) = radius_new(2);
%
%
% n=2;
% result = 1;
% %organize by y location
% while n <= num %Keep on comparing the value until you
compared every centers
%     for m = 2:num
%         if center_y(n) >= center_y(m)
%             %+1 if the center you are comparing is
smaller than the center
%             %that you are comparing with
%             result = result+1;
%         end
%     end
%     end
%     % %
%     %6 = largest x, 1 = smallest
%     center_x2(result,1) = center_x(n);
%     center_y2(result,1) = center_y(n);
%     radius_new2(result,1) = radius_new(n);
%     result = 1;
%     n = n + 1;
% end
%
%%organize by x
while n <= num %Keep on comparing the value until you
compared every centers
    for m = 1:num

```

```

        if center_new(n,1) <= center_new(m,1)
            %+1 if the x coordinate of the center that you
are comparing is smaller than the center
            %that you are comparing with
            result = result+1;
        end
    end
    %6 = smallest x, 1 = largest
    center_x2(result) = center_new(n,1);
    center_y2(result) = center_new(n,2);
    radius_new2(result) = radius_n(n);
    result = 0;
    n = n + 1;
end

%Organize with y
% while n <= num %Keep on comparing the value until you
compared every centers
%   for m = 1:num
%       if center_new(n,2) >= center_new(m,2)
%           %+1 if the x coordinate of the center that
you are comparing is smaller than the center
%           %that you are comparing with
%           result = result+1;
%       end
%   end
%   %6 = smallest x, 1 = largest
%   center_x2(result) = center_new(n,1);
%   center_y2(result) = center_new(n,2);
%   radius_new2(result) = radius_n(n);
%   result = 0;
%   n = n + 1;
% end

n=1;

%%
%inserting circle and line
while n <= (num)

    if n < num
        img = insertShape(I,'Line',[center_x2(n) center_y2(n)
center_x2(n+1)
center_y2(n+1)],'LineWidth',20,'Color','blue');
    end
end

```

```

end
img = insertShape(img, 'Circle', [center_x2(n)
center_y2(n) radius_new2(n)], 'LineWidth', 20, 'Color', 'red');

I = img;
n=n+1;
end
img = insertShape(img, 'Circle', [center_x2(num)
center_y2(num)
radius_new2(num)], 'LineWidth', 20, 'Color', 'red');
%Figure
figure(4)
imshow(img);
%% Finding Slopes and Angles
n=1;
i=1;
j=1;
while n <= (num/2)
    m(n) = (center_y2(j+1)-center_y2(j))/(center_x2(j+1)-
center_x2(j));
    if n == 2
        theta(i) = atan2(abs((m(n-1)-m(n))), abs((1+m(n-
1)*m(n))));
        i = i+1;
    end
    n=n+1;
    j=j+2;
end
theta(i) = atan2(abs((m(n-2)-m(n-1))), abs((1+m(n-2)*m(n-
1))));
theta_deg = radtodeg(theta);

```

H.5 Contact Force Analysis Code - Varying Angle

```

clear
clc

%% Varying Angle
%considers friction on the cable and uses matrix to solve for the normal
%forces and cable force on the cable at the same time
%%

%Calculates the joint angles during the preshaping phase
%This is based on virtual work and the constraint equation

%Link length
link_1 = 26.05/1000;
link_2 = 43.5/1000;
link_3 = 45.2/1000;

a2=9.98/1000;
b2=-10.38/1000; %%%%%%%%%%%%%%%%%%%%%%%%%change%%%%%%%%%%%%%%%%%%%%%%%%%

a3=9.48/1000;
b3=-10.38/1000; %%%%%%%%%%%%%%%%%%%%%%%%%change%%%%%%%%%%%%%%%%%%%%%%%%%

alpha = degtorad(90);

%coefficient of friction
mu = 0.3;
%Radius of Pulley (Based on the length of the flexure joints)

%Flexure Joint
%Young's Modulus
E = 2.76*10^6;%in Pa

b = 13/1000;
h = 5.5/1000;
%%%%%%%%%%%%%%%%%%%%%%%%%
L_i = 8/1000;
L_d = 7/1000;
I = b*h^3/12;

k1 = 0.0535; %Nm/rad
k2 = E*I/L_i; %Nm/rad
k3 = E*I/L_d; %Nm/rad

rc2x_2 = 21.88/1000;
rc3x_2 = 23.28/1000;
F_result=zeros(86);
F_res_com=zeros(86);
F_stability=zeros(86);
F_tot=zeros(86);
i = 1;
j = 1;
for theta_2_2 = degtorad(0:-1:-85)
    for theta_3_2 = degtorad(0:-1:-85)
        f_factor = 0;

        Fa_comp = (k2*theta_2_2)/(a2*sin(-theta_2_2/2+pi)-b2*cos(-
theta_2_2/2+pi))+f_factor;

```

```

%Fa = 10;
%Fa3= 5;
Fa =10.08;
Fa2=Fa/(exp(mu*(-theta_2_2/2)));
Fa3=Fa2/(exp(mu*(-theta_2_2/2))*exp(mu*(-theta_3_2/2)));
Fa4=Fa3/(exp(mu*(-theta_3_2/2)*exp(mu*(degtorad(78.83))));
if Fa4>Fa_comp
    F_res_comp(i,j) = Fa_comp;
    F_result(i,j) = 1; %1 = not slack 0 = slack
    %Fa_comp = tension of the cable (initial)
    %Fa4 = tension of the cable distal phalange
    %Fa_comp = minimum tension cable (without friction). If Fa4 is
    %the minimum tension cable as well (without friction). If Fa4
    %is less than Fa_comp then the cable is slacking
end
% Fa3 = Fa*exp(mu*(-theta_3_2/2))*exp(mu*(degtorad(78.83)));
% Fa2 = Fa3*exp(mu*(-theta_2_2/2))*exp(mu*(-theta_3_2/2));
s_theta_2(i,j) = radtodeg(theta_2_2);
s_theta_3(i,j) = radtodeg(theta_3_2);
A = [rc3x_2 0;
     link_2*cos(-theta_3_2)+rc3x_2 rc2x_2];
B = [k3*theta_3_2 - a3*Fa3*sin(-theta_3_2/2+pi)+b3*Fa3*cos(-
theta_3_2/2+pi);
     k2*theta_2_2 - a2*Fa2*sin(-theta_2_2/2+pi) + b2*Fa2*cos(-
theta_2_2/2+pi)];
C = inv(A)*B;
Fc3y(i,j) = C(1);
Fc2y(i,j) = C(2);

Fc3y_res(i,j) = Fc3y(i,j);
Fc2y_res(i,j) = Fc2y(i,j);
DP_F_ca (i,j) = (k3*theta_3_2 - a3*Fa3*sin(-
theta_3_2/2+pi)+b3*Fa3*cos(-theta_3_2/2+pi))/rc3x_2;
if Fc3y(i,j) > 0 && Fc2y (i,j) > 0
    F_stability(i,j) = 1;
end
if F_result(i,j) && F_stability(i,j) == true
    F_tot(i,j) = 1;
end
if F_tot(i,j) == 0
    Fc3y_res(i,j) = 0;
    Fc2y_res(i,j) = 0;
end
j= j+1;
end
i = i+1;
j = 1;

end

% Plots
figure(4) %Fc3y plot
surf(-s_theta_2,-s_theta_3,Fc3y_res);

```

```

hold on
scatter3(50,48,3,'filled','r')
hold on
scatter3(57,18,3,'filled','y')
hold on
xlabel('\theta_2 (deg)')
ylabel('\theta_3 (deg)')
zlabel('Contacting Force at Distal Phalanx (N)')
title('Distal Phalanx Contacting Force')
colormap(jet(6))
c = colorbar;
c.Label.String = 'Contact Force at Distal Phalanx (N)';
view(0, 90);

figure(5)
surf(-s_theta_2,-s_theta_3,Fc2y_res);
hold on
scatter3(50,48,3,'filled','r')
hold on
scatter3(57,18,3,'filled','y')
hold on
xlabel('\theta_2 (deg)')
ylabel('\theta_3 (deg)')
zlabel('Contacting Force at Intermediate Phalanx (N)')
title('Intermediate Phalanx Contacting Force')
colormap(jet(6))
c = colorbar;
c.Label.String = 'Contact Force at Intermediate Phalanx (N)';
view(0, 90);

figure(9) %Fc3y plot
surf(-s_theta_2,-s_theta_3,F_result);
hold on
xlabel('\theta_2 (deg)')
ylabel('\theta_3 (deg)')
zlabel('slack (N)')
title('slack or not')
c = colorbar;
c.Label.String = 'slack/ not slack';
view(0, 90);

figure(10) %Fc3y plot
surf(-s_theta_2,-s_theta_3,F_stability);
hold on
xlabel('\theta_2 (deg)')
ylabel('\theta_3 (deg)')
zlabel('stability')
title('stable or not')
c = colorbar;
c.Label.String = 'stable/not stable';
view(0, 90);

figure(11)
surf(-s_theta_2,-s_theta_3,F_tot);
hold on
xlabel('\theta_2 (deg)')
ylabel('\theta_3 (deg)')

```

```
zlabel('stability and slacking')
title('Stability')
c = colorbar;
c.Label.String = 'stable and not slacking /not stable or slacking';
view(0, 90);
```


H.6 Contact Force Analysis Code - Varying Contact Distance

```

clear
clc

%%%varying distance
%considers friction on the cable and uses matrix to solve for the normal
%forces and cable force on the cable at the same time
%%

%Calculates the joint angles during the preshaping phase

%Link length
link_1 = 26.05/1000;
link_2 = 43.5/1000;
link_3 = 45.2/1000;

a2=9.98/1000;
b2=-10.38/1000; %%%%%%%%%%%%%%%%%%%%%%%%%change%%%%%%%%%%%%%%%%%%%%%%%%

a3=9.48/1000;
b3=-10.38/1000; %%%%%%%%%%%%%%%%%%%%%%%%%change%%%%%%%%%%%%%%%%%%%%%%%%

alpha = degtorad(90);

%coefficient of friction
mu = 0.3;
%Radius of Pulley (Based on the length of the flexure joints)

%Flexure Joint
%Young's Modulus
E = 2.76*10^6;%in Pa

b = 13/1000;
h = 5.5/1000;
%%%%%%%%%%%%%%%%%%%%%%%%
L_i = 8/1000;
L_d = 7/1000;
I_ = b*h^3/12;

k1 = 0.0535; %Nm/rad
k2 = E*I/L_i; %Nm/rad
k3 = E*I/L_d; %Nm/rad

%% Test 1 - Changing the Contacting Point

%change
%original
theta_2 = degtorad(-50);
theta_3 = degtorad(-48);
Fa =10.08;
Fa2=Fa/(exp(mu*(-theta_2/2)));
Fa3=Fa2/(exp(mu*(-theta_2/2))*exp(mu*(-theta_3/2)));
Fa4=Fa3/(exp(mu*(-theta_3/2)*exp(mu*(degtorad(78.83))));

F_stability=zeros([25 80]);

rc3x2_c = 17;

```

```

rc3x3_c = 7;
rc3y = -17.45;
t2 = degtorad(42.34); %finger pad slope angle
t3 = degtorad(47.66); %finger pad slope angle
i = 1;
j = 1;
for rc2x = 15.86:0.5:27.9
    rc2x = rc2x/1000;

    for rc3x = 15.37:0.5: (31.19 + rc3x2_c + rc3x3_c)
        rc3x = rc3x/1000;
        s_rc2x(i,j) = rc2x*1000-15.86;
        s_rc3x(i,j) = rc3x*1000-15.37;

        if rc3x > 31.19/1000 && rc3x <= (31.19 + rc3x2_c)/1000
            rc3x2 = rc3x-31.19/1000;
            A = [(rc3x+rc3x2*cos(t2))*cos(t2)+(rc3y+rc3x2*sin(t2))*sin(t2) 0;
                (link_2*cos(-theta_3)+rc3x+rc3x2*cos(t2))*cos(t2)+(link_2*sin(-
                theta_3)+rc3y+rc3x2*sin(t2))*sin(t2) rc2x];
            B = [k3*theta_3 - a3*Fa3*sin(-theta_3/2+pi)+b3*Fa3*cos(-
                theta_3/2+pi);
                k2*theta_2 - a2*Fa2*sin(-theta_2/2+pi) + b2*Fa2*cos(-
                theta_2/2+pi)];
            C = inv(A)*B;

            DP_F(i,j) = (k3*theta_3 - a3*Fa3*sin(-theta_3/2+pi)+b3*Fa3*cos(-
                theta_3/2+pi))/...
                ((rc3x+rc3x2*cos(t2))*cos(t2)+(rc3y+rc3x2*sin(t2))*sin(-t2));
            fprintf('2\n');
        elseif rc3x > (31.19 + rc3x2_c)/1000
            rc3x2 = (rc3x2_c+rc3x3_c)/1000;
            rc3x3 = rc3x - rc3x2_c/1000 -rc3x3_c/1000;
            A =
            [(rc3x+rc3x2*cos(t2)+rc3x3*cos(t2+t3))*cos(t2+t3)+(rc3y+rc3x2*sin(t2)+rc3x3*
            in(t2+t3))*sin(t2+t3) 0;
            (link_2*cos(-
            theta_3)+rc3x+rc3x2*cos(t2)+rc3x3*cos(t2+t3))*cos(t2+t3)+(link_2*sin(-
            theta_3)+rc3y+rc3x2*sin(t2)+rc3x3*sin(t2+t3))*sin(t2+t3) rc2x];
            B = [k3*theta_3 - a3*Fa3*sin(-theta_3/2+pi) + b3*Fa3*cos(-
                theta_3/2+pi);
                k2*theta_2 - a2*Fa2*sin(-theta_2/2+pi) + b2*Fa2*cos(-
                theta_2/2+pi)];
            C = inv(A)*B;
            DP_F(i,j) = (k3*theta_3 - a3*Fa3*sin(-theta_3/2+pi) +
                b3*Fa3*cos(-theta_3/2+pi))/...

            ((rc3x+rc3x2*cos(t2)+rc3x3*cos(t2+t3))*cos(t2)+(rc3y+rc3x2*sin(t2)+rc3x3*sin(
            t2+t3))*sin(t2));
            fprintf('3\n');
        else
            A = [rc3x 0;
                link_2*cos(-theta_3)+rc3x rc2x];
            B = [k3*theta_3 - a3*Fa3*sin(-theta_3/2+pi)+b3*Fa3*cos(-
                theta_3/2+pi);
                k2*theta_2 - a2*Fa2*sin(-theta_2/2+pi) + b2*Fa2*cos(-
                theta_2/2+pi)];

```

```

C = inv(A)*B;

DP_F(i,j) = (k3*theta_3 - a3*Fa3*sin(-theta_3/2+pi)+b3*Fa3*cos(-
theta_3/2+pi))/rc3x;
fprintf('l');
end
Fc3y(i,j) = C(1);
Fc2y(i,j) = C(2);

Fc3y_res(i,j) = Fc3y(i,j);
Fc2y_res(i,j) = Fc2y(i,j);
if Fc3y(i,j) > 0 && Fc2y(i,j) > 0
F_stability(i,j) = 1;
end
if F_stability(i,j) == 0
Fc3y_res(i,j) = 0;
Fc2y_res(i,j) = 0;
end

j= j+1;

end
i = i+1;
j = 1;

end

% Plots
figure(1) %Fc3y plot
surf(s_rc2x,s_rc3x,Fc3y_res);
xlabel('Relative Intermediate Phalanx Contacting Distance (mm)')
ylabel('Relative Distal Phalanx Contacting Distance (mm)')
title('Distal Phalanx Contacting Force')
%shading interp
colormap(jet(6))
c = colorbar;
c.Label.String = 'Contact Force at Distal Phalanx (N)';
view(0, 90);

figure(2)
surf(s_rc2x,s_rc3x,DP_F);
xlabel('Relative Intermediate Phalanx Contacting Distance (mm)')
ylabel('Relative Distal Phalanx Contacting Distance (mm)')
zlabel('Contacting Force at Intermediate Phalanx (N)')
title('Contacting Distal Phalanx Only')
%shading interp
colormap default
c = colorbar;
c.Label.String = 'Contact Force at Distal Phalanx (N)';
view(0, 90);

figure(3)
surf(s_rc2x,s_rc3x,Fc2y_res);
xlabel('Relative Intermediate Phalanx Contacting Distance (mm)')
ylabel('Relative Distal Phalanx Contacting Distance (mm)')

```

```
zlabel('Contacting Force at Intermediate Phalanx (N)')
title('Intermediate Phalanx Contacting Force')
%shading interp
colormap(jet(6))
c = colorbar;
c.Label.String = 'Contact Force at Intermediate Phalanx (N)';
view(0, 90);

figure(12) %Fc3y plot
surf(s_rc2x,s_rc3x,F_stability);
hold on
xlabel('Relative Intermediate Phalanx Contacting Distance (mm)')
ylabel('Relative Distal Phalanx Contacting Distance (mm)')
zlabel('stability')
title('stable or not')
c = colorbar;
c.Label.String = 'stable/not stable';
view(0, 90);
```

I. BILL OF MATERIALS

Material Name	Quantity	Package Quantity	Price	Price per package	Quantity used for the prototype	Prototype part price
PLA Filament - 1kg	1	1000 g	\$ 23.00	0.02 \$/g	320 g	\$ 7.36
PMC 780	1	1360 g	\$ 34.08	0.03 \$/g	3.51 g	\$ 0.09
Sylgard 184	1	500 g	\$ 65.41	0.13 \$/g	4.1 g	\$ 0.54
Steel Phillips Rounded Head Screws #6 x 1/2"	1	100	\$ 2.72	0.03 \$/part	11	\$ 0.30
0.5mm x8mm	1	100	\$ 4.17	0.04 \$/part	3	\$ 0.13
Metric 316 stainless steel dowel pins 4mm x 24mm	1	10	\$ 6.29	0.63 \$/part	2	\$ 1.26
Metric 316 stainless steel dowel pins 5mm x 24mm	1	5	\$ 4.76	0.95 \$/part	2	\$ 1.90
Metric alloy steel cup point set screws M4 x 0.7mm x 10mm	1	100	\$ 5.04	0.05 \$/part	2	\$ 0.10
Extension spring with loop ends 0.75"x0.188"	1	12	\$ 7.00	0.58 \$/part	2	\$ 1.17
Metric 316 Stainless Steel Dowel Pins 4mm x 28mm	1	10	\$ 6.98	0.70 \$/part	1	\$ 0.70
90 deg right hand wound torsional spring 0.375"x0.218"	1	6	\$ 7.33	1.22 \$/part	1	\$ 1.22
18-8 stainless steel nylon insert locknuts M3	1	100	\$ 5.17	0.05 \$/part	4	\$ 0.21
M3 x 0.5mm Thread, 25mm Long screw	1	100	\$ 6.67	0.07 \$/part	2	\$ 0.13
M3 x 0.5mm Thread, 20mm Long screw	1	100	\$ 6.26	0.06 \$/part	1	\$ 0.06
Loop Ends, Zinc-Plated, Tempered, 2.49" Extended Length	1	3	\$ 3.08	1.03 \$/part	1	\$ 1.03
Velcro Strap	1		\$3.97		1	\$3.97
Power Pro Spectra Fiber Braided Fishing Line	1	13716 cm	\$ 13.96	0.00 \$/cm	40 cm	\$ 0.04
		Total	\$ 205.89		Total	\$ 20.20